Probing molecular layers with low-energy electrons

Tebyani, A.

Citation

Tebyani, A. (2024, March 14). *Probing molecular layers with low-energy electrons*. Retrieved from https://hdl.handle.net/1887/3721791

Probing Molecular Layers with Low-Energy Electrons

Proefschrift

ter verkrijging van
de graad van doctor aan de Universiteit Leiden,
op gezag van rector magnificus prof.dr.ir. H. Bijl,
volgens besluit van het college voor promoties
te verdedigen op donderdag 14 maart 2024
klokke 16.15 uur

door

Arash Tebyani

geboren te Tehran, Iran
in 1990

Promotores:

Prof.dr.ir. S.J. van der Molen
Prof.dr. M.A.G.J. Orrit

Promotiecommissie:

Prof.dr. R. Coehoorn (Technische Universiteit Eindhoven)
Dr.ir. J.P. Hoogenboom (Technische Universiteit Delft)
Prof.dr. J. Aarts
Dr. T. Lamberts
Prof.dr.ir. T.H. Oosterkamp
Prof.dr. J.M. van Ruitenbeek

ISBN: 978-94-6496-069-3

An electronic version of this dissertation is available at: https://openaccess.leidenuniv.nl

The work presented in this dissertation was funded by the Dutch Research Council (NWO) as part of the Frontiers of Nanoscience program.

Cover illustration by Steffie Padmos, www.steffiepadmos.com

The cover depicts the experimental setup. In a Low-Energy Electron Microscope, a beam of electrons is emitted from an electron gun at the top, and is directed to the sample, i.e. molecular layers. After interaction with the sample, the reflected electrons are collected and guided to the detector at the bottom, where they form an image.

Printed by: Gildeprint – Enschede

Table of Contents

1 Introduction **1**
References 7

2 Low Energy Electron Microscopy **15**
2.1 Introduction 16
2.2 Imaging in LEEM 18
2.3 Bright-field and dark-field imaging 22
2.4 Photoemission 22
2.5 Sample preparation 23
2.6 LEEM-IV spectroscopy 24
2.7 Angle-Resolved Reflected-Electron Spectroscopy (ARRES) 25
2.8 Electron Energy Loss Spectroscopy (EELS) 26
References 29

3 Comparison of Pentacene Layer Growth on Graphite and hBN Flakes **35**
3.1 Introduction 36
3.2 Experimental Technique 37
3.3 Results 37
3.4 Discussion 43
3.5 Conclusions 46
References 48
Supporting Information 53

4 Low-Energy Electron Irradiation Damage in Few-Monolayer Pentacene Films **57**
4.1 Introduction 58
4.2 Experimental Technique 59
4.3 Results 61
4.4 Discussion 65
4.5 Conclusions 68
References 70
Supporting Information 76

5 Critical Role of Electronic States above the Vacuum Level in Photo-Electron and Secondary-Electron Emission in Few-Monolayer Pentacene Films **85**
5.1 Introduction 86
5.2 Experimental Technique 87
5.3 Results and Discussion 88
5.4 Conclusions 94
References 95
Supporting Information 100

6 Band Structure of Few-Monolayer Pentacene Films Above the Vacuum Level **105**
6.1 Introduction 106
6.2 Experimental Technique and Results 106
6.3 Conclusions 117
References 118

7 Low Energy Electron Microscopy at Cryogenic Temperatures **121**
7.1 Introduction 122
7.2 Experimental Technique 123
7.3 Results and Discussion 128
7.4 Conclusions 133
References 134

Summary **141**

Samenvatting **145**

Curriculum Vitae **151**

List of Publications **153**

Acknowledgments **155**

1

Introduction

Molecular materials have been the subject of study in physics and materials science for decades due to their potential applications, particularly in electronics. Countless studies have investigated molecules in crystal form, in thin films and down to single molecules, as well as in hybrids with inorganic elements, for a vast range of properties including electronic, optical, and magnetic characteristics. In particular, charge transport and photovoltaic experiments constitute large portions of physics research in molecular, and more broadly organic, materials. Most of such research has been focused on organic molecules and polymers which possess a conjugated π-electron cloud, such as polycyclic aromatic hydrocarbons (PAHs), due to the higher degree of electron delocalization in this class of organic materials.

A key factor for the interest in organic materials, regarding applications, is the relatively low cost as well as ease of processing and device fabrication, in comparison with inorganic semiconductors. In addition, organic electronic devices can be flexible and lightweight. Another reason for the continued interest in molecular materials, both in fundamental science as well as in applications, is the fact that molecules partially retain their individual properties while at the same time forming van der Waals bonds with other molecules leading to formation of crystals, or crystalline thin films. This is a distinguishing factor between molecular and inorganic materials. This feature has made explanations of some phenomena more challenging. For example, regarding charge transport, deformations of the molecules as a result of movement of electric charge need to be taken into account, requiring use of polaron models rather than single-particle ones [1]. But this feature also offers unique advantages for many applications. For instance, it allows much greater flexibility in photovoltaic devices regarding the range of possible optical bandgaps, as a result of the wide variety of molecules synthesized. Furthermore, specific classes of molecules have unique applications. For example, when fluorescent molecules are embedded as guest impurities within host matrices, they primarily retain their optical properties. However, the host matrix induces slight changes in the fluorescence spectra of these molecules. As a result, fluorescent molecules can be employed as very sensitive probes of local acoustic phonons [2], pressure [3], temperature [4,5], electric field [4,6–10] and charge movement [11,12].

Organic materials have already found applications in commercial products such as organic light-emitting diode (OLED) displays, [13] as well as in important technological processes such as resists for optical [14,15] and electron-beam [16] lithography. In academic research, some notable examples of the diverse properties observed in organic materials include band-like charge transport in molecular and doped polymer films [17–21], Hall effect in molecular crystals [21,22] and molecule-doped polymer films [18], polymer-based memristors [23–26], metallic conduction at organic charge-transfer interfaces [27], various optoelectronic devices based on conjugated polymers [28–32] or molecules [20,33–38] as well as organic-inorganic hybrids [39–41], long-range exciton transport in polymer nanofibers [42], ambipolar polymer-based field-effect transistors with balanced electron and hole mobilities [43,44], negative piezoelectric effect in a ferroelectric polymer [45], long spin relaxation time in organic single crystals [46], polaron spin current transport in conjugated polymers [47] and many more. Meanwhile, conductance measurements across various molecules [48–57], either single molecules in mechanically-controllable break junctions or a few molecules in a self-assembled layer contacted by a conductive atomic tip, have led to observations of negative differential conductance [50,51], electric field control of magnetic anisotropy [52], vibrationally-induced two-level systems [53], spin effects in molecular magnets [51], electron-vibration interactions [54], shot noise [55], quantum interference [56] and humidity-controlled rectification of current [57], among others.

The molecule we have chosen to study is pentacene, a well-known representative of small conjugated PAHs. Pentacene has been the subject of intense study over the years for its electronic as well as optical properties. Some examples of optical properties of pentacene include observations of fluorescence from pentacene molecules embedded as impurities in p-terphenyl crystals [58], and jumps in resonance frequency in the fluorescence excitation spectrum of pentacene molecules in p-terphenyl crystals [59]. Regarding electronic properties, conductance studies have reported charge carrier mobility values above

1 cm^{2}V^{-1}s^{-1} in both single crystal and thin film pentacene devices, [17,60–63] which are notably higher than in typical organic conductors.

In crystal form, pentacene exhibits different polymorphs. [64] The known structures include the Campbell phase [65,66], a different crystal phase observed by Holmes et. al. [67], Mattheus et. al. [68] and Siegrist et. al. [69], as well as a thin film phase. [70,71] In the latter, the molecules adopt a tilted standing-up orientation with respect to the substrate surface, and have a herringbone crystal structure, as illustrated in Fig. 1.1. In this phase, which will be the focus of our study in the next chapters, the pentacene crystal is triclinic with lattice parameters 5.93 Å (o-a in Fig. 1.1), 7.56 Å (o-b in Fig. 1.1), 15.65 Å (o-c in Fig. 1.1), α =98.6˚, β=93.3˚, γ= 89.8˚ (angle between o-a and o-b). [70] Or, citing another study, the almost identical values of 5.958 Å, 7.596 Å, 15.61 Å, 81.25˚, 86.56˚ and 89.8˚. [71] The molecular long axis tilt from the surface normal for the two independent pentacene molecules in the unit cell are 5.7˚ and 6.8˚, [70] or 5.6˚ and 6.0˚ (on amorphous SiO$_2$ substrate) in another study. [71]

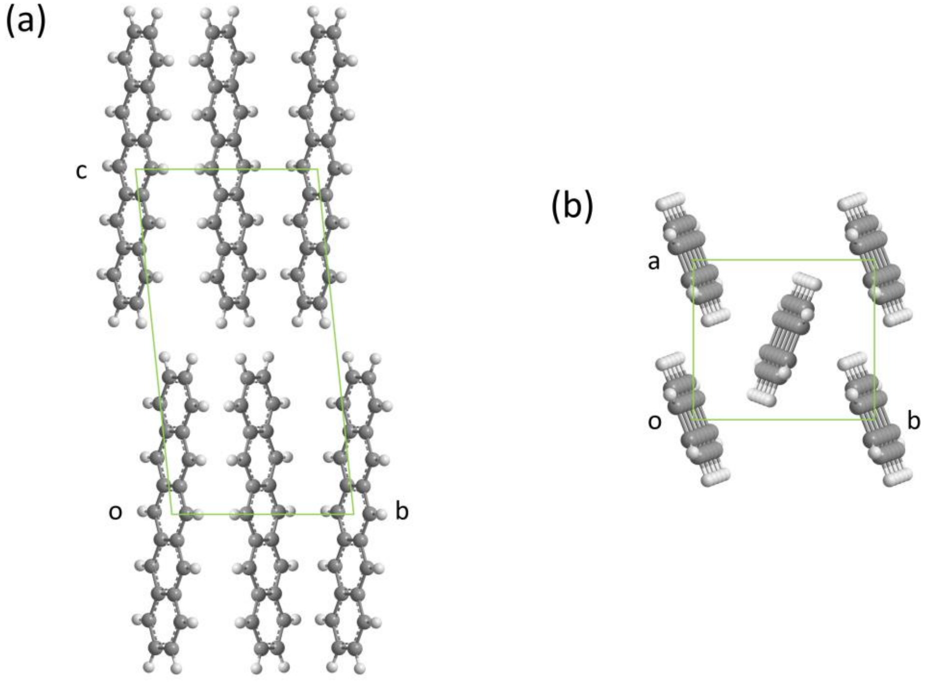

Fig. 1.1 Pentacene thin film (a) side view of two monolayers (b) top view. o-a, o-b and o-c represent the unit cell vectors.

In this thesis, we investigate pentacene crystals near the two-dimensional limit, i.e. in high-quality thin films of one to a few monolayers in thickness. Furthermore, we focus on real-time studies of these layers. We begin with a study of pentacene layer growth on different substrates in real-time using an advanced set-up. We aim to understand the effect of the surface crystal structure and electronic properties of the substrate on the structure of the resulting pentacene layer. Subsequently, we investigate various properties of the pentacene layers *in situ*, and monitor the dynamics of evolution of such properties as a result of controlled changes in the crystal. In particular, we focus on the evolution of the unoccupied electronic band structure of pentacene films as a function of thickness or external stimuli such as electron beam irradiation. The latter can cause controlled structural changes within the layers. We explore such beam-induced changes to the pentacene layers and compare them to other organic materials, and also discuss the implications for electron-beam lithography. Furthermore, we combine our knowledge of the changes in the electronic band structure with real-time measurements of other properties, to provide insights into secondary electron processes such as photo-electron and secondary electron emission.

For this aim, we use an experimental technique called Low Energy Electron Microscopy (LEEM). LEEM satisfies several important criteria for our research. First, in LEEM, the energy of the electrons used for imaging and spectroscopy is usually just a few electron Volts (eV). This leads to a low mean free path, [72,73] making LEEM suitable for studies of surfaces and ultrathin films. Second, because the entire field of view is illuminated at once with electrons (or photons), as opposed to scanning probe techniques, real-time monitoring of changes in the sample is possible, starting with the *in situ* preparation of the samples. Third, nanometer-resolution imaging [74] of the sample offers the ability to exclude local inhomogeneities from affecting the measured properties, by selecting sub-micrometer homogeneous areas to perform measurements on. This is in contrast to some common experimental techniques, such as charge transport measurements, that probe the properties of the sample as a whole. Fourth, typical electron energies in LEEM (0-20 eV) are particularly relevant for studying chemical processes and physical properties such as electronic band structure and crystal excitations. Fifth, due to the low energy of the electrons, beam irradiation damage to the molecular layers can be minimal for the lowest range of energies, depending on the material (chapter 4). Irradiation damage is a very important topic in research on organic samples. While some common microscopy techniques such as Transmission Electron Microscopy (TEM) or Scanning Electron Microscopy (SEM) offer high-resolution and real-time imaging, electron energies used in these techniques are typically tens or hundreds of keV, resulting in destruction of the organic sample during measurement. In contrast, minimal irradiation damage makes LEEM particularly favourable among microscopy techniques for studying organic materials. Finally, LEEM offers the ability to prepare samples *in situ* and perform all the measurements within one piece of equipment, all at ultrahigh vacuum (UHV) pressures, avoiding exposure of the sample to ambient conditions that can alter sample properties during transfer between different equipment.

In this thesis, we utilize the interaction of low-energy electrons with the molecular layers for two purposes. On the one hand, to learn about the properties of the layers, such as their crystal structure via diffraction. On the other hand, we employ low-energy electrons as an external stimulus to create controlled changes in the chemical and physical properties of the sample (chapters 4 and 5). Applying the variety of measurement techniques available in LEEM, we obtain insights from experiments on pentacene layers that can be generalized to wider classes of materials. In more detail, we discuss the following topics in the next chapters.

In chapter 2, we explain the primary experimental technique, i.e. LEEM. We introduce the instrument, how it works and the various measurement techniques available in LEEM. Such techniques include imaging in real-space and Low-Energy Electron Diffraction (LEED), use of apertures for bright-field, dark-field and µLEED imaging, PhotoElectron Emission Microscopy (PEEM), Electron Energy Loss Spectroscopy (EELS), LEEM-IV (intensity vs. voltage) spectroscopy and Angle-Resolved Reflected-Electron Spectroscopy (ARRES).

In chapter 3, we begin our exploration of molecular layers with an in-depth study of their growth. Growth of small aromatic molecules on surfaces has been the subject of several studies in the past. Here, we compare the growth of pentacene layers on graphite and hexagonal boron-nitride, two very different members of an emerging class of substrates, i.e. van der Waals materials.

In chapter 4, we study the low-energy electron chemistry initiated in the molecular layers as a result of exposure to a beam of very low-energy electrons. We measure electron beam irradiation damage cross-sections for incident electrons in the 0-40 eV range. We also investigate the effect of irradiation damage on the electronic and structural properties of the layers. Furthermore, we compare and contrast our results with similar studies on different classes of organic materials such as polymers, and discuss the implications for important technological processes such as electron-beam lithography.

In chapter 5, we study the evolution of the unoccupied electronic states of pentacene films via LEEM-IV spectroscopy, from one monolayer up to four monolayers. The results obtained for the unoccupied states are then correlated with measurements on (the energy-dependence of) secondary electron processes, specifically with PEEM and EELS measurements. Our results demonstrate the critical, and often overlooked, role of unoccupied states above the vacuum level on secondary electron processes, such as photo-electron and secondary electron emission. Our conclusions are generalizable not only to other organics, but to all classes of materials.

In chapter 6, we delve deeper into the unoccupied band structure of pentacene films above the vacuum level. Using ARRES, we measure the relation between energy and in-plane momenta for unoccupied states in pentacene layers, and remarkably find considerable dispersion. We compare the results for two and three monolayer films and also follow beam irradiation damage with ARRES band structure plots.

In chapter 7, we present an important advancement in LEEM, i.e. the extension of available sample temperatures from room temperature down to 15 K. We explain the design of a cryogenic sample chamber incorporated into the LEEM instrument at Leiden University, and show the first results obtained in the cryogenic chamber on a three-monolayer pentacene film. Specifically, we study electron beam irradiation damage and LEEM-IV spectra at various temperatures between 300 K and 52 K.

References

[1] A. Troisi, *Charge Transport in High Mobility Molecular Semiconductors: Classical Models and New Theories*, Chem. Soc. Rev. **40**, 2347 (2011).

[2] Y. Tian, P. Navarro, and M. Orrit, *Single Molecule as a Local Acoustic Detector for Mechanical Oscillators*, Phys. Rev. Lett. **113**, 135505 (2014).

[3] A. Muller, W. Richter, and L. Kador, *Pressure Effects on Single Molecules of Terrylene in P-Terphenyl*, Chem. Phys. Lett. **241**, 547 (1995).

[4] A. A. L. Nicolet, P. Bordat, C. Hofmann, M. A. Kol'chenko, B. Kozankiewicz, R. Brown, and M. Orrit, *Single Dibenzoterrylene Molecules in an Anthracene Crystal: Main Insertion Sites*, ChemPhysChem **8**, 1929 (2007).

[5] N. Verdal and A. M. Kelley, *Temperature Dependence of Phonon Sidebands in Line-Narrowed Fluorescence Spectra of Chromophores in Glasses*, J. Chem. Phys. **118**, 7985 (2003).

[6] A. Moradi, Z. Ristanović, M. Orrit, I. Deperasińska, and B. Kozankiewicz, *Matrix-Induced Linear Stark Effect of Single Dibenzoterrylene Molecules in 2,3-Dibromonaphthalene Crystal*, ChemPhysChem **20**, 55 (2019).

[7] M. Orrit, J. Bernard, A. Zumbusch, and R. I. Personov, *Stark Effect on Single Molecules in a Polymer Matrix*, Chem. Phys. Lett. **196**, 595 (1992).

[8] P. Tamarat, B. Lounis, J. Bernard, M. Orrit, S. Kummer, R. Kettner, S. Mais, and T. Basche, *Pump-Probe Experiments with a Single Molecule: Ac-Stark Effect and Nonlinear Optical Response*, Phys. Rev. Lett. **75**, 1514 (1995).

[9] C. Brunel, P. Tamarat, B. Lounis, J. C. Woehl, and M. Orrit, *Stark Effect on Single Molecules of Dibenzanthanthrene in a Naphthalene Crystal and in a N-Hexadecane Shpol'skii Matrix*, J. Phys. Chem. A **103**, 2429 (1999).

[10] P. Bordat, M. Orrit, R. Brown, and A. Wurger, *The Anomalous Stark Effect of Single Terrylene Molecules in P-Terphenyl Crystals*, Chem. Phys. **258**, 63 (2000).

[11] A. A. L. Nicolet, M. A. Kol'Chenko, C. Hofmann, B. Kozankiewicz, and M. Orrit, *Nanoscale Probing of Charge Transport in an Organic Field-Effect Transistor at Cryogenic Temperatures*, Phys. Chem. Chem. Phys. **15**, 4415 (2013).

[12] S. Faez, S. J. van der Molen, and M. Orrit, *Optical Tracing of Multiple Charges in Single-Electron Devices*, Phys. Rev. B **90**, 205405 (2014).

[13] M. Moser, A. Wadsworth, N. Gasparini, and I. McCulloch, *Challenges to the Success of Commercial Organic Photovoltaic Products*, Adv. Energy Mater. **11**, 2100056 (2021).

[14] T. Itani and T. Kozawa, *Resist Materials and Processes for Extreme Ultraviolet Lithography*, Jpn. J. Appl. Phys. **52**, 010002 (2013).

[15] L. Li, X. Liu, S. Pal, S. Wang, C. K. Ober, and E. P. Giannelis, *Extreme Ultraviolet Resist Materials for Sub-7 nm Patterning*, Chem. Soc. Rev. **46**, 4855 (2017).

[16] Y. Chen, *Nanofabrication by Electron Beam Lithography and Its Applications: A Review*, Microelectron. Eng. **135**, 57 (2015).

[17] Y. Zhang et al., *Probing Carrier Transport and Structure-Property Relationship of Highly Ordered Organic Semiconductors at the Two-Dimensional Limit*, Phys. Rev. Lett. **116**, 016602 (2016).

[18] K. Kang et al., *2D Coherent Charge Transport in Highly Ordered Conducting Polymers Doped by Solid State Diffusion*, Nat. Mater. **15**, 896 (2016).

[19] T. Sakanoue and H. Sirringhaus, *Band-like Temperature Dependence of Mobility in a Solution-Processed Organic Semiconductor*, Nat. Mater. **9**, 736 (2010).

[20] Y. Shi et al., *Bottom-up Growth of n-Type Monolayer Molecular Crystals on Polymeric Substrate for Optoelectronic Device Applications*, Nat. Commun. **9**, 2933 (2018).

[21] N. A. Minder, S. Ono, Z. Chen, A. Facchetti, and A. F. Morpurgo, *Band-like Electron Transport in Organic Transistors and Implication of the Molecular Structure for Performance Optimization*, Adv. Mater. **24**, 503 (2012).

[22] V. Podzorov, E. Menard, J. A. Rogers, and M. E. Gershenson, *Hall Effect in the Accumulation Layers on the Surface of Organic Semiconductors*, Phys. Rev. Lett. **95**, 226601 (2005).

[23] B. Tian et al., *A Robust Artificial Synapse Based on Organic Ferroelectric Polymer*, Adv. Electron. Mater. **5**, 1800600 (2019).

[24] G. Liu, C. Wang, W. Zhang, L. Pan, C. Zhang, X. Yang, F. Fan, Y. Chen, and R. W. Li, *Organic Biomimicking Memristor for Information Storage and Processing Applications*, Adv. Electron. Mater. **2**, 1500298 (2016).

[25] T. Berzina, A. Smerieri, M. Bernab, A. Pucci, G. Ruggeri, V. Erokhin, and M. P. Fontana, *Optimization of an Organic Memristor as an Adaptive Memory Element*, J. Appl. Phys. **105**, 124515 (2009).

[26] Y. Van de Burgt, E. Lubberman, E. J. Fuller, S. T. Keene, G. C. Faria, S. Agarwal, M. J. Marinella, A. Alec Talin, and A. Salleo, *A Non-Volatile Organic Electrochemical Device as a Low-Voltage Artificial Synapse for Neuromorphic Computing*, Nat. Mater. **16**, 414 (2017).

[27] H. Alves, A. S. Molinari, H. Xie, and A. F. Morpurgo, *Metallic Conduction at Organic Charge-Transfer Interfaces*, Nat. Mater. **7**, 574 (2008).

[28] H. Sirringhaus, N. Tessler, and R. Friend, *Integrated Optoelectronic Devices Based on Conjugated Polymers*, Science **280**, 1741 (1998).

[29] J. Zaumseil, C. L. Donley, J. S. Kim, R. H. Friend, and H. Sirringhaus, *Efficient Top-Gate, Ambipolar, Light-Emitting Field-Effect Transistors Based on a Green-Light-Emitting Polyfluorene*, Adv. Mater. **18**, 2708 (2006).

[30] M. C. Gwinner, D. Kabra, M. Roberts, T. J. K. Brenner, B. H. Wallikewitz, C. R. McNeill, R. H. Friend, and H. Sirringhaus, *Highly Efficient Single-Layer Polymer Ambipolar Light-Emitting Field-Effect Transistors*, Adv. Mater. **24**, 2728 (2012).

[31] T. H. Thomas et al., *Short Contacts between Chains Enhancing Luminescence Quantum Yields and Carrier Mobilities in Conjugated Copolymers*, Nat. Commun. **10**, 2614 (2019).

[32] S. Holliday et al., *High-Efficiency and Air-Stable P3HT-Based Polymer Solar Cells with a New Non-Fullerene Acceptor*, Nat. Commun. **7**, 11585 (2016).

[33] L. S. Cui et al., *Fast Spin-Flip Enables Efficient and Stable Organic Electroluminescence from Charge-Transfer States*, Nat. Photonics **14**, 636 (2020).

[34] X. Ai, E. W. Evans, S. Dong, A. J. Gillett, H. Guo, Y. Chen, T. J. H. Hele, R. H. Friend, and F. Li, *Efficient Radical-Based Light-Emitting Diodes with Doublet Emission*, Nature **563**, 536 (2018).

[35] H. Guo et al., *High Stability and Luminescence Efficiency in Donor–Acceptor Neutral Radicals Not Following the Aufbau Principle*, Nat. Mater. **18**, 977 (2019).

[36] P. J. Budden et al., *Singlet Exciton Fission in a Modified Acene with Improved Stability and High Photoluminescence Yield*, Nat. Commun. **12**, 1527 (2021).

[37] C. He et al., *Asymmetric Electron Acceptor Enables Highly Luminescent Organic Solar Cells with Certified Efficiency over 18%*, Nat. Commun. **13**, 2598 (2022).

[38] N. B. Kotadiya, P. W. M. Blom, and G. J. A. H. Wetzelaer, *Efficient and Stable Single-Layer Organic Light-Emitting Diodes Based on Thermally Activated Delayed Fluorescence*, Nat. Photonics **13**, 765 (2019).

[39] Y. Hassan et al., *Ligand-Engineered Bandgap Stability in Mixed-Halide Perovskite LEDs*, Nature **591**, 72 (2021).

[40] B. Zhao et al., *High-Efficiency Perovskite–Polymer Bulk Heterostructure Light-Emitting Diodes*, Nat. Photonics **12**, 783 (2018).

[41] T. Zhu, L. Shen, S. Xun, J. S. Sarmiento, Y. Yang, L. Zheng, H. Li, H. Wang, J. L. Bredas, and X. Gong, *High-Performance Ternary Perovskite–Organic Solar Cells*, Adv. Mater. **34**, 2109348 (2022).

[42] X.-H. Jin, M. B. Price, J. R. Finnegan, C. E. Boott, J. M. Richter, A. Rao, S. M. Menke, R. H. Friend, G. R. Whittell, and I. Manners, *Long-Range Exciton Transport in Conjugated Polymer Nanofibers Prepared by Seeded Growth*, Science **360**, 897 (2018).

[43] Z. Chen et al., *High-Performance Ambipolar Diketopyrrolopyrrole-Thieno[3,2-b]Thiophene Copolymer Field-Effect Transistors with Balanced Hole and Electron Mobilities*, Adv. Mater. **24**, 647 (2012).

[44] Z. Chen, H. Lemke, S. Albert-Seifried, M. Caironi, M. M. Nielsen, M. Heeney, W. Zhang, I. McCulloch, and H. Sirringhaus, *High Mobility Ambipolar Charge Transport in Polyselenophene Conjugated Polymers*, Adv. Mater. **22**, 2371 (2010).

[45] I. Katsouras et al., *The Negative Piezoelectric Effect of the Ferroelectric Polymer Poly(Vinylidene Fluoride)*, Nat. Mater. **15**, 78 (2016).

[46] J. Tsurumi, H. Matsui, T. Kubo, R. Häusermann, C. Mitsui, T. Okamoto, S. Watanabe, and J. Takeya, *Coexistence of Ultra-Long Spin Relaxation Time and Coherent Charge Transport in Organic Single-Crystal Semiconductors*, Nat. Phys. **13**, 994 (2017).

[47] S. Watanabe, K. Ando, K. Kang, S. Mooser, Y. Vaynzof, H. Kurebayashi, E. Saitoh, and H. Sirringhaus, *Polaron Spin Current Transport in Organic Semiconductors*, Nat. Phys. **10**, 308 (2014).

[48] M. Kiguchi, R. Stadler, I. S. Kristensen, D. Djukic, and J. M. Van Ruitenbeek, *Evidence for a Single Hydrogen Molecule Connected by an Atomic Chain*, Phys. Rev. Lett. **98**, 146802 (2007).

[49] R. Smit, Y. Noat, C. Untiedt, et al., *Measurement of the Conductance of a Hydrogen Molecule*, Nature **419**, 906 (2002).

[50] M. L. Perrin et al., *Large Negative Differential Conductance in Single-Molecule Break Junctions*, Nat. Nanotechnol. **9**, 830 (2014).

[51] H. B. Heersche, Z. De Groot, J. A. Folk, H. S. J. van der Zant, C. Romeike, M. R. Wegewijs, L. Zobbi, D. Barreca, E. Tondello, and A. Cornia, *Electron Transport through Single Mn_{12} Molecular Magnets*, Phys. Rev. Lett. **96**, 206801 (2006).

[52] A. S. Zyazin et al., *Electric Field Controlled Magnetic Anisotropy in a Single Molecule*, Nano Lett. **10**, 3307 (2010).

[53] W. H. A. Thijssen, D. Djukic, A. F. Otte, R. H. Bremmer, and J. M. Van Ruitenbeek, *Vibrationally Induced Two-Level Systems in Single-Molecule Junctions*, Phys. Rev. Lett. **97**, 226806 (2006).

[54] O. Tal, M. Krieger, B. Leerink, and J. M. Van Ruitenbeek, *Electron-Vibration Interaction in Single-Molecule Junctions: From Contact to Tunneling Regimes*, Phys. Rev. Lett. **100**, 196804 (2008).

[55] D. Djukic and J. M. Van Ruitenbeek, *Shot Noise Measurements on a Single Molecule*, Nano Lett. **6**, 789 (2006).

[56] C. M. Guédon, H. Valkenier, T. Markussen, K. S. Thygesen, J. C. Hummelen, and S. J. van der Molen, *Observation of Quantum Interference in Molecular Charge Transport*, Nat. Nanotechnol. **7**, 305 (2012).

[57] H. Atesci, V. Kaliginedi, J. A. Celis Gil, H. Ozawa, J. M. Thijssen, P. Broekmann, M. A. Haga, and S. J. van der Molen, *Humidity-Controlled Rectification Switching in Ruthenium-Complex Molecular Junctions*, Nat. Nanotechnol. **13**, 117 (2018).

[58] M. Orrit and J. Bernard, *Single Pentacene Molecules Detected by Fluorescence Excitation in a P-Terphenyl Crystal*, Phys. Rev. Lett. **65**, 2716 (1990).

[59] W. P. Ambrose and W. E. Moerner, *Fluorescence Spectroscopy and Spectral Diffusion of Single Impurity Molecules in a Crystal*, Nature **349**, 225 (1991).

[60] J. Y. Lee, S. Roth, and Y. W. Park, *Anisotropic Field Effect Mobility in Single Crystal Pentacene*, Appl. Phys. Lett. **88**, 252106 (2006).

[61] Y. Kato, S. Iba, R. Teramoto, T. Sekitani, T. Someya, H. Kawaguchi, and T. Sakurai, *High Mobility of Pentacene Field-Effect Transistors with Polyimide Gate Dielectric Layers*, Appl. Phys. Lett. **84**, 3789 (2004).

[62] O. D. Jurchescu, J. Baas, and T. T. M. Palstra, *Effect of Impurities on the Mobility of Single Crystal Pentacene*, Appl. Phys. Lett. **84**, 3061 (2004).

[63] H. Klauk, M. Halik, U. Zschieschang, G. Schmid, W. Radlik, and W. Weber, *High-Mobility Polymer Gate Dielectric Pentacene Thin Film Transistors*, J. Appl. Phys. **92**, 5259 (2002).

[64] C. C. Mattheus, A. B. Dros, J. Baas, G. T. Oostergetel, A. Meetsma, J. L. De Boer, and T. T. M. Palstra, *Identification of Polymorphs of Pentacene*, Synthetic Met. **138**, 475 (2003).

[65] R. B. Campbell, J. Monteath Robertson, and J. Trotter, *The Crystal and Molecular Structure of Pentacene*, Acta Cryst. **14**, 705 (1961).

[66] R. B. Campbell, J. Monteath Robertson, and J. Trotter, *The Crystal Structure of Hexacene, and a Revision of the Crystallographic Data for Tetracene*, Acta Cryst. **15**, 289 (1962).

[67] D. Holmes, S. Kumaraswamy, A. J. Matzger, and K. P. C. Vollhardt, *On the Nature of Nonplanarity in the [N]Phenylenes*, Chem. Eur. J. **5**, 3399 (1999).

[68] C. C. Mattheus, A. B. Dros, J. Baas, A. Meetsma, J. L. De Boer, and T. T. M. Palstra, *Polymorphism in Pentacene*, Acta Cryst. **57**, 939 (2001).

[69] T. Siegrist, C. Kloc, J. H. Schön, B. Batlogg, R. C. Haddon, S. Berg, and G. A. Thomas, *Enhanced Physical Properties in a Pentacene Polymorph*, Angew. Chem. Int. Ed. **40**, 1732 (2001).

[70] H. Yoshida, K. Inaba, and N. Sato, *X-Ray Diffraction Reciprocal Space Mapping Study of the Thin Film Phase of Pentacene*, Appl. Phys. Lett. **90**, 181930 (2007).

[71] S. Schiefer, M. Huth, A. Dobrinevski, and B. Nickel, *Determination of the Crystal Structure of Substrate-Induced Pentacene Polymorphs in Fiber Structured Thin Films*, J. Am. Chem. Soc. **129**, 10316 (2007).

[72] M. P. Seah and W. A. Dench, *Quantitative Electron Spectroscopy of Surfaces: A Standard Data Base for Electron Inelastic Mean Free Paths in Solids*, Surf. Interface Anal. **1**, 2 (1979).

[73] D. Geelen, J. Jobst, E. E. Krasovskii, S. J. van der Molen, and R. M. Tromp, *Nonuniversal Transverse Electron Mean Free Path through Few-Layer Graphene*, Phys. Rev. Lett. **123**, 086802 (2019).

[74] R. M. Tromp, J. B. Hannon, A. W. Ellis, W. Wan, A. Berghaus, and O. Schaff, *A New Aberration-Corrected, Energy-Filtered LEEM/PEEM Instrument. I. Principles and Design*, Ultramicroscopy **110**, 852 (2010).

2

Low Energy Electron Microscopy

Abstract

In this chapter, we introduce Low Energy Electron Microscopy (LEEM). We will describe the operation of LEEM and explain the various measurement techniques available in LEEM that are used in the following chapters.

2.1 Introduction

Low Energy Electron Microscopy (LEEM) was first realized in 1985 by Wolfgang Telieps and Ernst Bauer. [1] Because of the low energy of incident electrons when they interact with the sample, typically only a few electron volts, LEEM is particularly suitable for probing the surface of the sample. This is a consequence of the small mean free path of electrons at such low energies, about one to a few nanometers. [2,3] Combined with the advantage of simultaneous illumination of the entire field of view, as opposed to scanning probe techniques such as Scanning Tunneling Microscopy (STM), LEEM has been successfully employed to study a variety of dynamic phenomena at surfaces in real time. Prominent examples include phase transitions, and growth of molecular crystals, oxide films, metals, two-dimensional materials, etc. [4–19] The ability to follow changes in the sample in real time is particularly powerful noting that it holds true for any of the various techniques for imaging and spectroscopy available in LEEM. Several of these measurement techniques are explained in this chapter.

The LEEM instrument used for the measurements in this dissertation is the ESCHER LEEM instrument at Leiden University. [20] Here, ESCHER stands for **E**lectronic, **S**tructural and **CHE**mical nanoimaging in **R**eal-time. The ESCHER LEEM instrument is based on an aberration-corrected version [21,22] of the IBM/SPECS LEEM instrument designed by Rudolf Tromp and first introduced in 1998. [23] Its sample chamber has an UltraHigh Vacuum (UHV) pressure of ~1×10^{-9} mbar or lower, with experiments possible at gas pressures up to 1×10^{-5} mbar. Measurements and sample preparation can be performed at sample temperatures from room temperature up to 1800 K. A Knudsen cell evaporator connected to the sample chamber allows for *in situ* sublimation of various materials such as metals or molecules. A schematic of the LEEM instrument is illustrated in Fig. 2.1. The ESCHER instrument is also equipped with a cryogenic sample chamber, omitted from this schematic. The cryogenic extension of the microscope is discussed in detail in chapter 7.

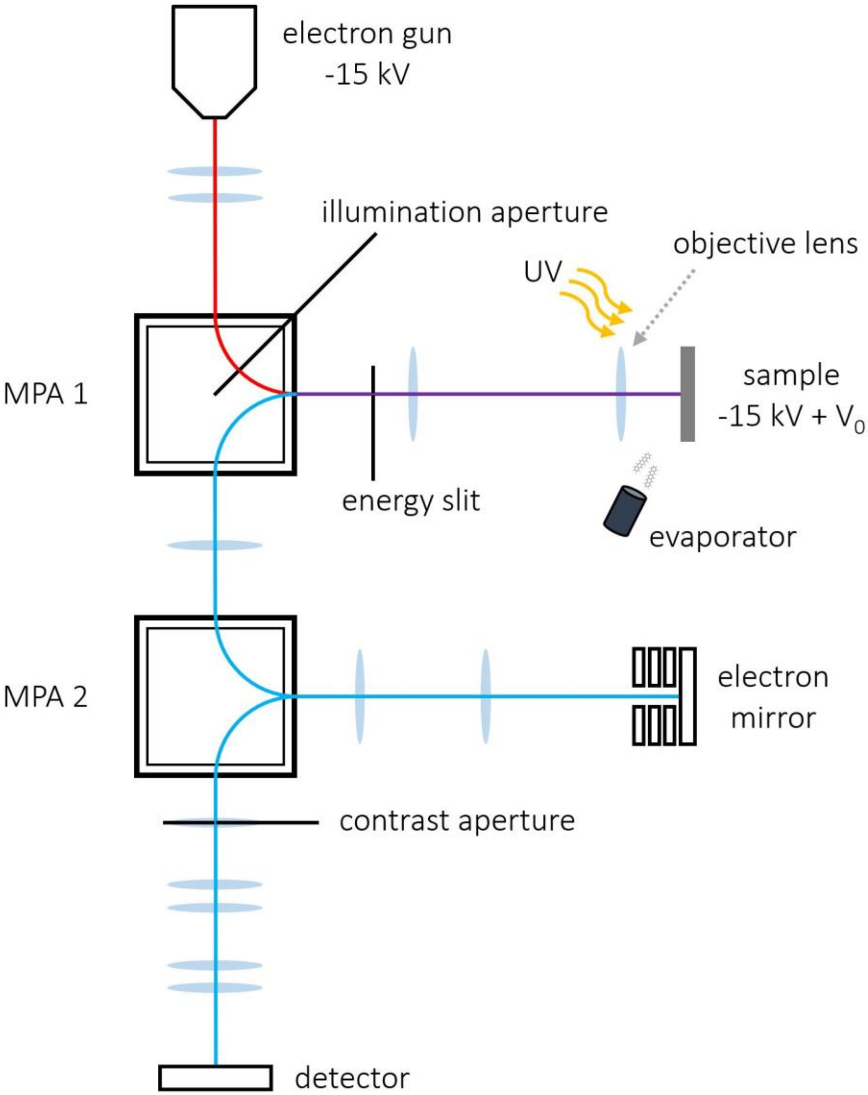

Fig. 2.1 Schematic of LEEM instrument. A beam of electrons is emitted from the electron gun at the top and traverses the column with a kinetic energy of 15 keV along the red line. MPA1 bends the electron beam toward the sample. An electric field between the objective lens and the sample decelerates the electrons to a kinetic energy of eV_0. The electrons interact with the sample with this energy, which is tunable by setting the sample potential. Reflected electrons are accelerated by the same electric field and directed toward MPA1, and follow the blue trajectory toward the detector. The purple line shows where the paths of the incident and reflected electrons overlap. MPA2 works in the same manner as MPA1 but directs the electrons to an electrostatic electron mirror, which corrects the lowest-order aberrations of the microscope. Imaging with photoelectrons is also possible via a Hg UV lamp attached to the sample chamber. Furthermore, a Knudsen cell evaporator connected to the sample chamber allows for *in situ* molecule sublimation. Various lenses and apertures of the microscope are also shown in the figure.

2.2 Imaging in LEEM

LEEM includes a variety of magnetic and electrostatic components, which are employed to focus, disperse, deflect or otherwise adjust the electron beam. Imaging with electrons proceeds in the following way. Electrons are emitted from an electron gun, located at the top in Fig. 2.1. The electron source is a cold-field emitter, in which electrons are extracted from a sharp cathode due to a strong electric field between the cathode and a planar anode inside the gun, via a mechanism called Fowler-Nordheim emission. [24] This manner of electron beam generation leads to a narrower spread in the energy of the electrons, about 250 meV, compared to alternatives such as thermionic emission. After emission from the tip, the electrons are accelerated to a kinetic energy of 15 keV, and traverse the column with this energy. Several magnetic lenses and deflectors in the illumination column, i.e. before magnetic prism array 1 (MPA1), are used to focus and adjust the electron beam, such as vary the beam diameter or beam tilt. MPA1 bends the electron beam by 90° toward the objective lens and the sample. The LEEM is a cathode lens instrument, with the sample acting as the cathode. The electrons are decelerated by an electric field of ~10 kV/mm between a grounded objective lens, and the sample, which is biased at -15 kV$+V_0$ (close to the electron gun potential) and located 1-2 millimeters away from the front of the objective lens. After deceleration, a collimated beam of electrons with a kinetic energy of $eV_0+\Delta\Phi$ reaches and interacts with the sample. Here, $\Delta\Phi$ represents the difference between the work functions of the sample and the electron gun. The interaction energy can be precisely tuned by changing the sample bias potential, with typical values of 0-50 eV. After reflection from the sample, the electrons are re-accelerated by the same electric field between the objective lens and the sample to an energy of ~15 keV. The objective lens forms a magnified real-space image of the sample using a magnetic lens field, and directs the electrons toward MPA1. This time, the Lorentz force exerted by the prism bends the electron beam by 90° downwards (see the schematic). Hence, the prism separates the incident and the reflected beams. Magnetic prism array 2 (MPA 2) operates in the same manner as MPA 1, except it directs the electron beam toward an electron mirror. MPA 2 and the electron mirror comprise the aberration-correcting part of the instrument. Aberrations are corrected upon reflection from the mirror. The reflected beam is then bent by MPA 2 toward the detector, travelling through several magnetic lenses (i.e. the projector column) along its path. In the detector, the electrons are first multiplied by a micro-channel plate, and subsequently hit a phosphorescent screen, creating an image that is captured by a CCD camera.

Regarding aberration correction, the electron mirror is comprised of four silicon-bronze discs, one biased at ground potential and the three others at adjustable (negative) high potentials. The ratio of the potentials between the disks determines the optical properties of the mirror. Aberration correction removes the lowest-order chromatic and spherical aberrations, which are caused predominantly by the cathode objective lens. As a result, the resolution is enhanced from 4.1 nm in the uncorrected version of the instrument, to 1.4 nm after aberration correction. [21] The electron mirror cannot correct higher order or higher rank aberrations, i.e. only C_c and C_3 are corrected. We also note that the LEEM instrument is installed on a vibration isolation foundation, accompanied by an active vibration damping system, in order to reduce mechanical instabilities that can deteriorate the resolution. Furthermore, all the electronic power supplies are highly stable with noise levels of only about 1 ppm, a critical requirement for high-resolution imaging.

In a LEEM instrument, it is also possible to project a reciprocal-space, rather than a real-space, image on the detector screen by changing the excitations of the magnetic lenses in the projector column (i.e. between MPA 2 and the detector). This makes it possible to observe the Low Energy Electron Diffraction (LEED) pattern on the detector screen. The reciprocal-space image contains information about the angular distribution of electrons. We note that since only the out-of-plane momentum of the electrons is affected by the cathode lens electric field, the in-plane momenta of the electrons from the sample are preserved in the LEED image. Given that the wavelengths of the electrons used in LEEM are on the order of a few Ångstroms (5 Å for 6 eV electrons), surface atomic lattices of crystalline samples act as a diffraction grating for the incoming electrons, creating bright spots in the diffraction image at in-plane momenta where the Bragg conditions for constructive interference of scattered electron waves are satisfied. Hence, the diffraction pattern conveys information about the crystalline structure of the sample surface. Combined with real-space information about the surface morphology, the microstructure of the sample can now be characterized.

Diffraction images contain more information than just the position of the diffraction peaks. Study of changes in the profile of the diffraction spots over time or as a result of external stimuli is called Spot Profile Analysis LEED (SPA-LEED). In chapter 4, we use this technique to study electron beam irradiation damage in pentacene films.

In LEEM, real-space and reciprocal-space planes alternatingly follow each other, with the various electron optical elements projecting these planes onto the next element, with possible adjustments in magnification or rotation. Using an analogy with light optics, Fig. 2.2 illustrates the formation of a diffraction image in the back focal plane of an objective lens (plane 1), as well as an inverted real-space image further away (plane 2). In LEEM, due to the effect of the electric field between the objective lens and the sample on the electrons, the trajectories of the rays from the sample are actually parabolic. But the electric field by itself also forms a virtual image of the sample, at a somewhat greater distance to the grounded front of the objective lens. Taking this virtual image of the sample as the object, Fig. 2.2 applies without modification (i.e. straight-line trajectories).

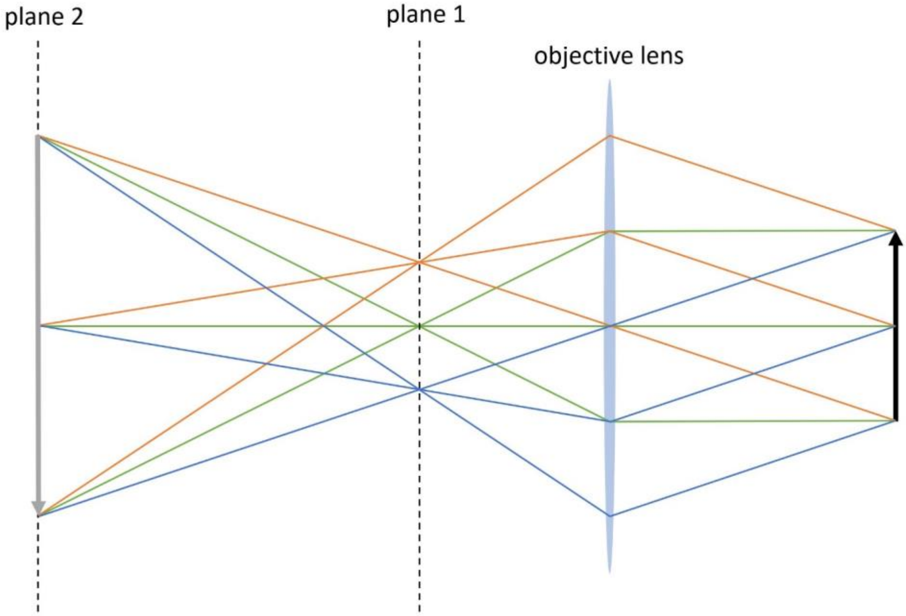

Fig. 2.2 Illustration of image formation in an optical system. The black arrow at the right represents the object. The orange, green and blue lines are optical rays from the object. Planes 1 and 2 indicate diffraction-space and real-space planes after the objective lens, respectively. The grey arrow at the left shows an inverted image of the object. In LEEM, the trajectory of the electrons from the sample is actually parabolic, due to the electric field between the sample and the objective lens.

The ESCHER instrument allows for insertion of apertures along various real-space or diffraction planes. This capability greatly enhances the ability to perform various imaging and spectroscopy techniques, as we describe in the remainder of this chapter. For example, frequently, the area on the sample illuminated by the electron beam is not homogeneous within a beam diameter of several micrometers. To collect information only from smaller homogeneous regions, we can place an aperture along the beam's path in order to limit the illuminated area on the sample surface. Fig. 2.1 shows such an illumination aperture inserted along the diagonal of MPA 1, allowing for selection of sub-micrometer areas on the sample. Placing such an aperture with the goal of investigating the diffraction corresponding to the chosen real-space area is called micro-LEED (μLEED) imaging. Also, with the aperture blocking some of the beam, we can record small fluctuations of the beam current (~pA) which are not detectable by the electron gun electronics, in order to correct for the noise in the measured data caused by such small fluctuations.

Fig. 2.3 shows an example of LEEM and µLEED imaging, in order to study the microstructure of a pentacene film. Regions with different intensities in Fig. 2.3(a) indicate different layer counts in the pentacene layer, with higher layer counts appearing brighter. In other words, the film thickness is not homogeneous across the illuminated area. Intensity variations between different regions are explained later in this chapter, in the discussion of "LEEM-IV spectroscopy". By placement of an aperture smaller than 1 µm in diameter on regions corresponding to each of the different layer counts, we examined their diffraction patterns. The illuminated areas are indicated with orange, green and blue circles in Fig. 2.3(a), with their associated µLEED patterns in Fig. 2.3(b-d), enclosed with a circle of the same color. The center spot in each image corresponds to specularly reflected electrons, while the other spots are characteristic of the herringbone lattice structure of the pentacene layers. The µLEED images are similar in all three regions, with the diffraction spots appearing increasingly sharper on thicker areas, an indication of better crystallinity. We also note an absence of rotation between the µLEED patterns, signaling that the layers grow on top of each other as a single crystal.

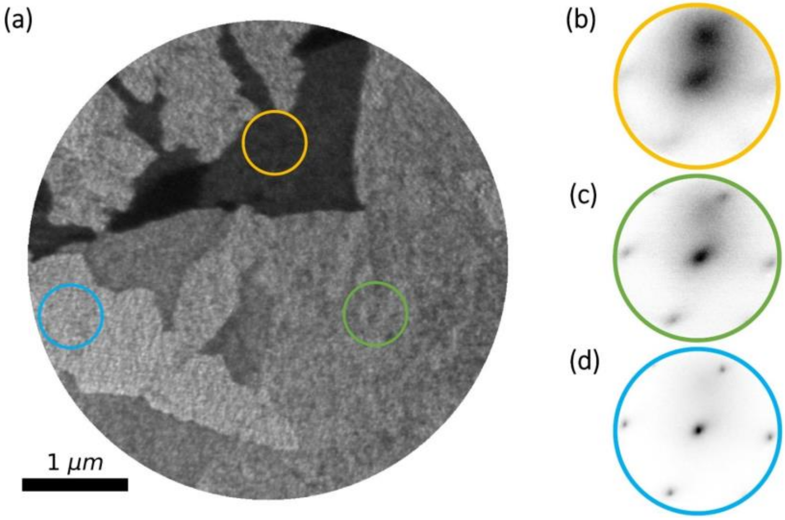

Fig. 2.3 µLEED imaging. (a) Bright-field image of a pentacene film, obtained by a beam of 1.9 eV electrons. Intensity variations within the image indicate non-homogeneity of layer count. The orange, green and blue circles in (a) indicate the locations of the illumination aperture for µLEED imaging. (b-d) diffraction patterns corresponding to the chosen areas in (a), imaged by 11 eV electrons. The colors of the circles around the diffraction patterns correspond to the areas selected by the illumination aperture in (a). The diffraction patterns corresponding to brighter areas (higher layer counts) appear sharper, an indication of better crystallinity. Also, lack of rotation between the diffraction patterns indicates that the layers grow on top of each other as a single crystal.

2.3 Bright-field and dark-field imaging

In the example above, we placed an aperture in a real-space image plane (MPA 1 diagonal) to select certain areas of the sample surface in order to investigate their corresponding diffraction. Similarly, we can place an aperture in a diffraction plane in order to let through only the electrons from a certain diffraction peak, and block the rest. Such an aperture is shown in Fig. 2.1, named “contrast aperture”. In the resulting real-space image after such filtering, only areas on the sample surface that contribute to the chosen diffraction peak lighten up. If the aperture lets through only the 0^{th}-order diffraction spot, i.e. normal incidence and reflection of electrons, the resulting real-space image is called a “bright-field” image. The intensities in a bright-field image contain information about the unoccupied electronic density of states (DOS) of the material, as will be explained in the discussion of “LEEM-IV spectroscopy”. If any other diffraction spot is selected, the resulting image is called a “dark-field” image. Dark-field imaging differentiates between regions of the image that have different crystal structure or orientations. In chapter 3, we employ bright-field and dark-field imaging to investigate a crystalline pentacene layer on graphite (Fig. 3.3 in chapter 3).

2.4 Photoemission

So far, we have discussed imaging using electrons from the electron gun. The LEEM instrument is also equipped with two ultraviolet (UV) light sources, namely a Hg discharge lamp (hν = 4.9 eV) and a Helium I/II light source (hν = 21.2 eV and 40.8 eV). These sources allow for the possibility of imaging with photoelectrons emitted from the sample, or PhotoElectron Emission Microscopy (PEEM). The photoelectrons are accelerated to a kinetic energy of ~15 keV by the same electric field between the objective lens and the sample, and afterwards follow the same path as the reflected electrons from the electron gun. Given that the photons from the Hg lamp illuminate the entire sample surface at once, PEEM can be used to monitor surface phenomena at a larger field of view of several tens of μm. We use PEEM with a Hg lamp to study the dynamics of growth of pentacene layers on various substrates, as will be discussed in chapters 3 and 5.

PEEM and other photoemission imaging and spectroscopy techniques, such as Angle-Resolved PhotoEmission Spectroscopy (ARPES), are widely used in condensed matter physics and surface science to probe the occupied electronic bands in solids. Simply put, if the energy of the incoming photons is higher than the ionization energy of the sample (i.e. the minimum amount of energy required to extract a photoelectron from the sample), photoelectrons can generally be ejected from occupied states in the material. In chapter 5, we additionally study the role of unoccupied electronic states above the vacuum level, measurable by LEEM-IV spectroscopy (see below), in photoemission.

2.5 Sample preparation

Now, we briefly discuss sample preparation inside the LEEM instrument. As mentioned earlier, a Knudsen cell evaporator can be attached to the sample chamber, allowing for molecule sublimation by resistive heating of the crucible inside the evaporator. The sublimated molecules follow a line of sight from the crucible to the sample surface in the UHV pressure of the sample chamber. Upon reaching the sample surface, they may be adsorbed on the surface via van der Waals forces (physisorption) or formation of chemical bonds with the surface (chemisorption), depending on the substrate. The substrate temperature also plays an important role in adsorption and layer formation. At higher temperatures the incoming molecules (or atoms) can diffuse more easily on the surface, an important factor in the formation of crystalline layers. On the other hand, temperatures that are too high may prevent the incoming molecules from staying on the surface. In this dissertation, we explore the growth of crystalline pentacene layers on a variety of substrates, such as silicon, silicon oxide, as well as van der Waals substrates graphite and hexagonal boron-nitride (hBN). The results are presented in chapters 3 and 5.

Prior to thin film growth, the substrate is prepared *in situ*. An electron bombardment heater behind the sample can heat the sample up to ~1500˚C. This heater was frequently used to prepare atomically-flat silicon surfaces by removing the SiO_2 layer at high temperatures (~1100˚C). For some experiments, the substrates were prepared outside the vacuum system and then transferred into the LEEM instrument. Examples of such substrates include hBN and graphite flakes exfoliated onto SiO_2 surfaces using Scotch tape. [25,26] For these substrates, the heater was used to clean the flake surfaces from adsorbates by keeping the samples at elevated temperatures, such as 500˚C, for several hours. All the substrates were cooled to (near) room temperature prior to pentacene sublimation, otherwise the molecules would not stay on the surface due to their high vapor pressure at higher temperatures. [27]

The capability to prepare the samples and perform various measurements all *in situ* in the UHV sample chamber of the LEEM instrument is a major advantage. It reduces the possibility of surface contamination between sample preparation and measurement as a result of exposure to ambient pressure. Note that given the surface sensitivity of LEEM any contamination of the sample surface interferes with the measurements.

Next, we discuss a few spectroscopy techniques available in LEEM.

2.6 LEEM-IV spectroscopy

The intensity in any region of a LEEM image depends on the energy of the incident beam used for imaging. In other words, LEEM images of the same area of the sample obtained with different beam energies look different. Recording the intensity variations of any location on the sample surface while varying the incident beam energy (i.e. changing the sample bias voltage) within a given range, yields what is called a "LEEM-IV (intensity vs. voltage) spectrum". To obtain a LEEM-IV spectrum, typically an aperture is placed on the 0^{th}-order diffraction spot in order to prevent electrons from other diffraction peaks, as well as incoherently-scattered and secondary electrons, from affecting image intensity. Such LEEM-IV spectra are a fingerprint of the electronic and crystalline structure of the area. At low electron energies, LEEM-IV spectra are mostly determined by the unoccupied electronic DOS above the vacuum level. [28–34] Simply put, if the DOS is high at a given energy, the incoming electrons can enter the sample, resulting in lower reflectivity in the LEEM-IV spectrum. Vice versa, at energies corresponding to a band gap, the electrons cannot enter the sample and the reflectivity is high. The exact value of the reflectivity, however, depends not only on the availability of unoccupied electronic states, but also on the quantum mechanical probability of both the incident and reflected vacuum electron plane waves coupling with the unoccupied sample states. The higher this probability, the lower the reflectivity. [35]

Differences in the LEEM-IV reflectivity spectra of different regions on the sample at any given electron energy create the contrast in LEEM images. For example, the intensity variations within the LEEM image in Fig. 2.3(a) are due to differences in the LEEM-IV spectra of different pentacene layer counts.

A different approach for obtaining LEEM-IV spectra is placement of an illumination aperture on a homogeneous area on the sample and recording the intensity variations of the diffraction pattern as a function of incident beam energy. Plotting the intensity variations of the 0^{th}-order diffraction peak yields the same LEEM-IV spectrum as the one obtained by following the intensity variations of the same area in bright-field images, as explained above. This approach, however, also allows for observing the energy-dependence of the intensities of other diffraction peaks.

As an example, Fig. 2.4(a) shows a bright-field image of a Au film on mica (sample purchased from Phasis). The terrace step edges on the areas in between the bigger gaps can be seen as narrow black lines created by Fresnel interference of the electron waves reflected from adjacent sides of the step edge. This is called “phase contrast”. Fig. 2.4(b) shows a LEEM-IV spectrum obtained on the Au film in Fig. 2.4(a). Here, the negative energies indicate that the incident electrons do not have sufficient kinetic energy to reach the sample, i.e. the sample potential is too negative. This results in total reflection, i.e. the sample acts as a perfect mirror. 0 eV corresponds to electrons that reach the sample with no kinetic energy. This energy is called the mirror-mode transition (MMT) energy. Due to the energy spread of the beam, ~250 meV, some electrons have slightly lower or higher energies at MMT energy. At positive energies, electrons interact with the sample.

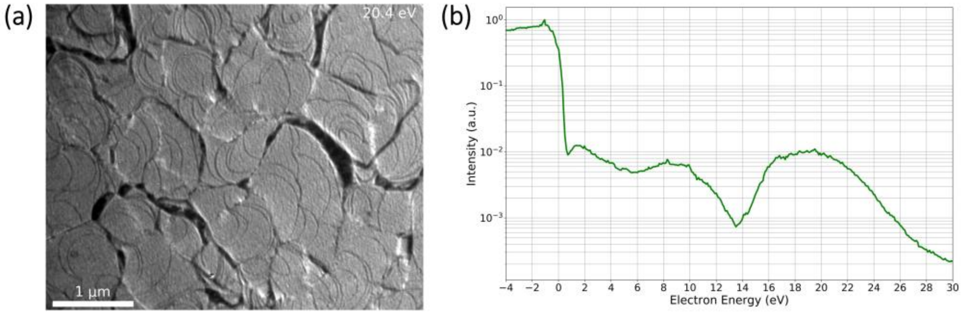

Fig. 2.4 (a) bright-field image of a Au film on mica, obtained by a beam of 20.4 eV electrons. The narrow black lines on the areas in between the bigger gaps indicate terrace step edges. They are created by Fresnel interference of the electron waves reflected from adjacent sides of the step edge. (b) LEEM-IV spectrum of Au on mica. Here, 0 eV corresponds to vacuum level. Negative energies indicate that the incident electrons do not have sufficient kinetic energy to reach the sample, resulting in total reflection. At positive energies, the incident electrons interact with the sample.

2.7 Angle-Resolved Reflected-Electron Spectroscopy (ARRES)

LEEM-IV spectra obtained as described above, follow the intensity variations of electrons with normal incidence and reflection from the sample. In other words, the incident electrons do not have any in-plane momentum when interacting with the sample. Angle-resolved reflected-electron spectroscopy (ARRES) is an extension of LEEM-IV spectroscopy as introduced above, in which the incident electrons are provided with in-plane momenta. This allows for probing the unoccupied electronic DOS across the entire Brillouin zone. ARRES is described in detail in chapter 6.

2.8 Electron Energy Loss Spectroscopy (EELS)

We discussed earlier that electrons with energies above the MMT energy reach the sample and interact with it. These electrons are either transmitted through the sample, absorbed by the sample, or reflected from it. Reflection or scattering of electrons can be either elastic or inelastic. Elastically-scattered electrons have the same kinetic energy as the incident electrons. They create a LEED pattern in the case of reflection from crystalline surfaces. On the other hand, some incident electrons lose some of their energy upon interaction with the sample, as a result of creation of excitations in the sample. Hence, they are inelastically scattered. Interaction of an incoming electron beam with the sample can also lead to creation of secondary electrons. The secondary electrons typically have low energies of only a few eV for the incident electron energies used in LEEM. These secondary electrons are accelerated by the electric field between the objective lens and the sample in the same way as photoelectrons and reflected electrons from the electron gun.

We can learn about the physical properties of the sample by analyzing the energy distribution of the electrons leaving the sample by a measurement technique called Electron Energy Loss Spectroscopy (EELS). [36–38] This is implemented in the following way. A slit is placed in the back focal plane of the objective lens ("energy slit" in Fig. 2.1). In this diffraction plane, the angular distributions of electrons with different energies occur as superimposed concentric disks of varying radii, with higher energies corresponding to bigger radii. Each disk represents the in-plane momentum distributions of the electrons with a certain energy. Fig. 2.5(a) illustrates this with three disks representative of three different electron energies. Note that only the outlines of the disks are shown. The energy slit selects a narrow slice of the diffraction space (at fixed k_x) in which the intensities from these concentric disks are superimposed. In Fig. 2.5(a), the energy slit is placed across the center of the disks ($k_x = 0$). Since the magnetic prism array is dispersive, after the beam passes through the prism, the aforementioned disks are shifted relative to each other along the dispersive direction of the magnetic prism array (x direction); see Fig. 2.5(b). As a result, the slices of the concentric disks selected by the energy slit are no longer superimposed on top of each other, but rather are shifted with respect to one another; see Fig. 2.5(b). The exact amount of the shift depends on the energy of the electrons. In the ESCHER LEEM instrument, an energy resolution of about 160 meV can be achieved for 15 keV electrons. [39] Due to the relation between the energy and the momenta of the electrons ($E \sim k^2$), the shifted slices are enveloped in a parabola, as illustrated in Fig. 2.5(c). With the energy slit placed across the center of the concentric disks, the vertex of this parabola corresponds to electrons leaving the sample with kinetic energy of 0 eV. Hence, in this manner, the energy distribution of electrons from the sample is revealed.

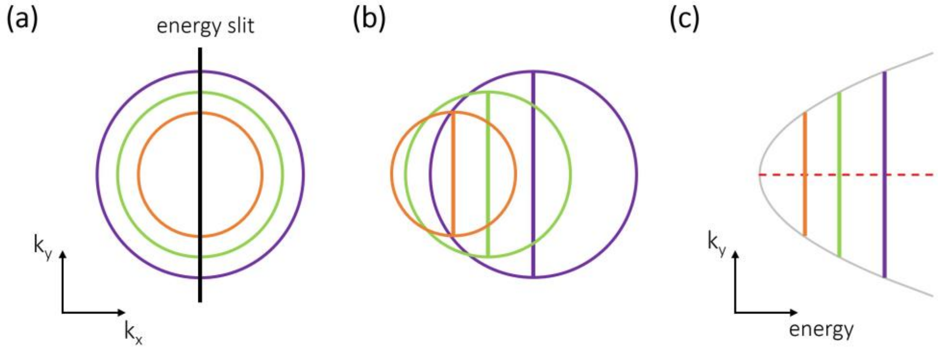

Fig. 2.5 Electron Energy Loss Spectroscopy. (a) Three superimposed concentric disks (only the outlines are shown) in the diffraction space, each containing the angular distribution of electrons from the sample with a certain energy. Higher energies correspond to larger disk radii. An energy slit selecting a slice of the diffraction space is shown. Here, the energy slit passes through the center of the disks and corresponds to k_x=0. (b) the disks are shifted relative to each other after passing through MPA1, due to the dispersive character of the prism. In other words, electrons with different energies are deflected by slightly different angles upon passing through the prism. (c) The slices of the diffraction pattern selected by the energy slit corresponding to various disks are no longer superimposed. The slices from all the possible disks form a parabola, due to the relation between the energy and the momenta of the electrons ($E \sim k^2$). The dashed red line corresponds to k_y=0. Hence, the spectrum obtained from this linecut yields the energy distribution of electrons from the sample with no in-plane momenta (k_x=k_y=0)

Fig. 2.6 shows an example of an electron energy spectrum obtained from a three-monolayer pentacene film. For this measurement, the energy slit was placed across the center of the diffraction pattern (k_x=0). The spectrum in Fig. 2.6 is a linecut passing through the vertex of the parabola along the dashed red line in Fig. 2.5(c), and hence, corresponds to electrons with no in-plane momenta ($k_x = k_y = 0$). Here, the strong peak at 10.1 eV corresponds to elastically scattered electrons, while the distribution between 0 eV and 4 eV corresponds to secondary electrons (near the vertex of the parabola). Electron energy spectra in pentacene films are further explored in chapter 5.

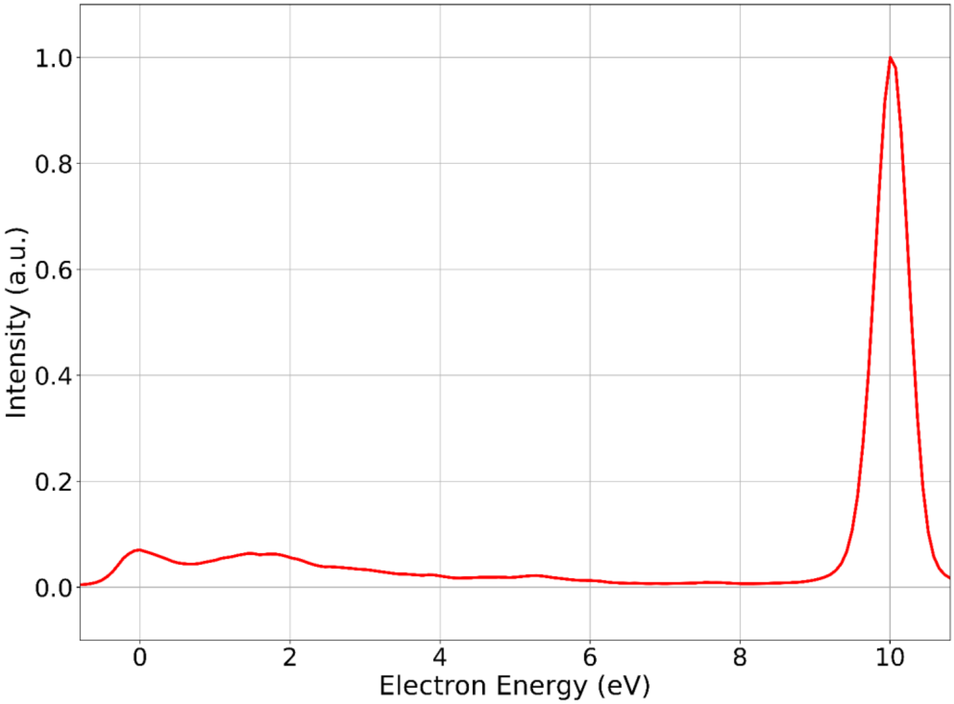

Fig. 2.6 Electron energy spectrum from a three-monolayer pentacene film. The peak at the right corresponds to elastically scattered electrons having an energy of 10.1 eV. The distribution at the left (0-4 eV) corresponds to secondary electrons.

References

[1] W. Telieps and E. Bauer, *An Analytical Reflection and Emission UHV Surface Electron Microscope*, Ultramicroscopy **17**, 57 (1985).

[2] M. P. Seah and W. A. Dench, *Quantitative Electron Spectroscopy of Surfaces: A Standard Data Base for Electron Inelastic Mean Free Paths in Solids*, Surf. Interface Anal. **1**, 2 (1979).

[3] D. Geelen, J. Jobst, E. E. Krasovskii, S. J. van der Molen, and R. M. Tromp, *Nonuniversal Transverse Electron Mean Free Path through Few-Layer Graphene*, Phys. Rev. Lett. **123**, 086802 (2019).

[4] Frank-J. Meyer zu Heringdorf, M. C. Reuter, and & R. M. Tromp, *Growth Dynamics of Pentacene Thin Films*, Nature **412**, 517 (2001).

[5] A. Al-Mahboob, J. T. Sadowski, Y. Fujikawa, K. Nakajima, and T. Sakurai, *Kinetics-Driven Anisotropic Growth of Pentacene Thin Films*, Phys. Rev. B **77**, 035426 (2008).

[6] F. J. Meyer Zu Heringdorf, M. C. Reuter, and R. M. Tromp, *The Nucleation of Pentacene Thin Films*, Appl. Phys. A **78**, 787 (2004).

[7] A. J. H. van der Torren et al., *Growing a $LaAlO_3/SrTiO_3$ Heterostructure on $Ca_2Nb_3O_{10}$ Nanosheets*, Sci. Rep. **9**, 17617 (2019).

[8] J. Kautz, M. W. Copel, M. S. Gordon, R. M. Tromp, and S. J. van der Molen, *Titration of Submonolayer Au Growth on Si(111)*, Phys. Rev. B **89**, 035416 (2014).

[9] A. J. H. van der Torren, S. J. van der Molen, and J. Aarts, *Imaging Pulsed Laser Deposition Growth of Homo-Epitaxial $SrTiO_3$ by Low-Energy Electron Microscopy*, Nanotechnology **27**, 495702 (2016).

[10] A. J. H. van der Torren, Z. Liao, C. Xu, N. Gauquelin, C. Yin, J. Aarts, and S. J. van der Molen, *Formation of a Conducting $LaAlO_3/SrTiO_3$ Interface Studied by Low-Energy Electron Reflection during Growth*, Phys. Rev. Mater. **1**, 075001 (2017).

[11] N. M. Buckanie and F. J. Meyer zu Heringdorf, *Photoemission Electron Microscopy Study of Anthracene Growth on Si(111)*, Surf. Sci. **601**, 1701 (2007).

[12] T. Yasue, T. Koshikawa, and E. Bauer, *Low Energy Electron Microscopy/Diffraction Study on Growth of Ge on Si(113) Surface*, J. Vac. Sci. Technol. B **20**, 2496 (2002).

[13] A. Pavlovska, E. Bauer, and M. Giessen, *Low Energy Electron Microscopy Study of In on Si(111)*, J. Vac. Sci. Technol. B **20**, 2478 (2002).

[14] H. W. Liu, H. T. Yuan, N. Fukui, L. Zhang, J. F. Jia, Y. Iwasa, M. W. Chen, T. Hashizume, T. Sakurai, and Q. K. Xue, *Growth of Topological Insulator Bi_2Te_3 Ultrathin Films on Si(111) Investigated by Low-Energy Electron Microscopy*, Cryst. Growth Des. **10**, 4491 (2010).

[15] H. Hibino, S. Wang, C. M. Orofeo, and H. Kageshima, *Growth and Low-Energy Electron Microscopy Characterizations of Graphene and Hexagonal Boron Nitride*, Prog. Cryst. Growth Ch. **62**, 155 (2016).

[16] C. Klein, R. Ramchal, M. Farle, and A. K. Schmid, *Direct Imaging of Spin-Reorientation Transitions in Ultrathin Ni Films by Spin-Polarized Low-Energy Electron Microscopy*, Surf. Interface Anal. **38**, 1550 (2006).

[17] A. Makoveev, P. Procházka, A. Shahsavar, L. Kormoš, T. Krajňák, V. Stará, and J. Čechal, *Kinetic Control of Self-Assembly Using a Low-Energy Electron Beam*, Appl. Surf. Sci. **600**, 154106 (2022).

[18] R. Zdyb, A. Locatelli, S. Heun, S. Cherifi, R. Belkhou, and E. Bauer, *Nanomagnetism Studies with Spin-Polarized Low-Energy Electron Microscopy and x-Ray Magnetic Circular Dichroism Photoemission Electron Microscopy*, Surf. Interface Anal. **37**, 239 (2005).

[19] K. L. Man, M. S. Altman, and H. Poppa, *Spin Polarized Low Energy Electron Microscopy Investigations of Magnetic Transitions in Fe/Cu(100)*, Surf. Sci. **480**, 163 (2001).

[20] S. M. Schramm, J. Kautz, A. Berghaus, O. Schaff, R. M. Tromp, and S. J. van der Molen, *Low-Energy Electron Microscopy and Spectroscopy with ESCHER: Status and Prospects*, IBM J. Res. & Dev. **55**, 1:1 (2011).

[21] R. M. Tromp, J. B. Hannon, A. W. Ellis, W. Wan, A. Berghaus, and O. Schaff, *A New Aberration-Corrected, Energy-Filtered LEEM/PEEM Instrument. I. Principles and Design*, Ultramicroscopy **110**, 852 (2010).

[22] R. M. Tromp, J. B. Hannon, W. Wan, A. Berghaus, and O. Schaff, *A New Aberration-Corrected, Energy-Filtered LEEM/PEEM Instrument II. Operation and Results*, Ultramicroscopy **127**, 25 (2013).

[23] R. M. Tromp, M. Mankos, M. C. Reuter, A. W. Ellis, and M. Copel, *A New Low Energy Electron Microscope*, Surf. Rev. Lett. **5**, 1189 (1998).

[24] R. H. Fowler and L. Nordheim, *Electron Emission in Intense Electric Fields*, Proc. R. Soc. Lond. A **119**, 173 (1928).

[25] K. S. Novoselov, D. Jiang, F. Schedin, T. J. Booth, V. V Khotkevich, S. V Morozov, and A. K. Geim, *Two-Dimensional Atomic Crystals*, P. Natl. Acad. Sci. **102**, 10451 (2005).

[26] K. S. Novoselov, A. K. Geim, S. V Morozov, D. Jiang, Y. Zhang, S. V Dubonos, I. V Grigorieva, and A. A. Firsov, *Electric Field Effect in Atomically Thin Carbon Films*, Science **306**, 666 (2004).

[27] V. Oja and E. M. Suuberg, *Vapor Pressures and Enthalpies of Sublimation of Polycyclic Aromatic Hydrocarbons and Their Derivatives*, J. Chem. Eng. Data **43**, 486 (1998).

[28] E. Bauer, *Surface Microscopy with Low Energy Electrons* (2014), Springer New York, ISBN: 978-1-4939-0934-6

[29] J. B. Pendry, *The Application of Pseudopotentials to Low-Energy Electron Diffraction II: Calculation of the Reflected Intensities*, J. Phys. C: Solid State Phys. **2**, 2273 (1969).

[30] J. B. Pendry, *Theory of Photoemission*, Surf. Sci. **57**, 679 (1976).

[31] J. Jobst, J. Kautz, D. Geelen, R. M. Tromp, and S. J. van der Molen, *Nanoscale Measurements of Unoccupied Band Dispersion in Few-Layer Graphene*, Nat. Commun. **6**, 8926 (2015).

[32] J. Jobst, A. J. H. van der Torren, E. E. Krasovskii, J. Balgley, C. R. Dean, R. M. Tromp, and S. J. van der Molen, *Quantifying Electronic Band Interactions in van der Waals Materials Using Angle-Resolved Reflected-Electron Spectroscopy*, Nat. Commun. **7**, 13621 (2016).

[33] V. N. Strocov, E. E. Krasovskii, W. Schattke, N. Barrett, H. Berger, D. Schrupp, and R. Claessen, *Three-Dimensional Band Structure of Layered $TiTe_2$: Photoemission Final-State Effects*, Phys. Rev. B **74**, 195125 (2006).

[34] V. N. Strocov, H. I. Starnberg, and P. O. Nilsson, *Mapping the Excited-State Bands above the Vacuum Level with VLEED: Principles, Results for Cu, and the Connection to Photoemission*, J. Phys.: Condens. Matter. **8**, 7539 (1996).

[35] J. I. Flege and E. E. Krasovskii, *Intensity-Voltage Low-Energy Electron Microscopy for Functional Materials Characterization*, Phys. Status Solidi RRL **8**, 463 (2014).

[36] Y. Fujikawa, T. Sakurai, and R. M. Tromp, *Micrometer-Scale Band Mapping of Single Silver Islands in Real and Reciprocal Space*, Phys. Rev. B **79**, 121401(R) (2009).

[37] R. M. Tromp, Y. Fujikawa, J. B. Hannon, A. W. Ellis, A. Berghaus, and O. Schaff, *A Simple Energy Filter for Low Energy Electron Microscopy/Photoelectron Emission Microscopy Instruments*, J. Phys.: Condens. Matter. **21**, 314007 (2009).

[38] Y. Fujikawa, T. Sakurai, and R. M. Tromp, *Surface Plasmon Microscopy Using an Energy-Filtered Low Energy Electron Microscope*, Phys. Rev. Lett. **100**, 126803 (2008).

[39] S. Schramm, PhD Thesis (Leiden University): *Imaging with Aberration-Corrected Low Energy Electron Microscopy* (2013), ISBN: 978-90-8593-152-2. http://hdl.handle.net/1887/20843

3

Comparison of Pentacene Layer Growth on Graphite and hBN Flakes *

Abstract

We use PhotoElectron Emission Microscopy (PEEM) and Low-Energy Electron Microscopy (LEEM) to study the growth dynamics of pentacene layers on graphite and hexagonal boron nitride (hBN) flakes in real-time. These two substrates have similar atomic surface lattices but different electronic band structures. On both substrates, we find pentacene molecules to initially cover the flake surface with a flat-lying wetting layer. From diffraction and dark-field images, we find the wetting layer to be comprised of crystalline domains in six different orientations. Subsequently, pentacene layer growth proceeds in notably different manners on the two substrates, forming tilted recumbent crystalline domains on graphite versus standing-up thin film phase crystals on hBN. We discuss these results in light of the multi-faceted way in which different factors such as the electronic density of states of the surface, templating due to surface lattice structure, and cleanliness of the surface affect the growth of the molecular adlayer. We also measure LEEM reflectivity spectra related to the unoccupied density of states above the vacuum level, of the wetting layer on both substrates. We argue that the stronger electronic interaction between pentacene and graphite, compared to hBN, is responsible for the difference between the LEEM reflectivity spectra as well as the formation of different pentacene phases growing on the two substrates after the wetting layer has formed.

---

* This chapter has been submitted for publication as "Comparison of Pentacene Layer Growth on Graphite and hBN Flakes", A. Tebyani, R.M. Tromp, S.J. van der Molen

3.1 Introduction

Van der Waals (vdW) materials have emerged in recent years as a promising class of substrate materials for growth of molecular layers. One approach is to combine molecular adlayers with vdW materials to create heterostructures with tailored new properties. For instance, p-n heterojunctions stemming from the combination of pentacene and MoS_2 are found to be gate-tunable and exhibit interesting photovoltaic effects, such as ultrafast (several picoseconds) charge transfer and a long-lived charge-separated state. [1,2] Other examples include gate-tunable vertical graphene-pentacene barristor devices [3] or doping effects caused in graphene by adsorbate NO_2 molecules. [4] Another approach is to use vdW materials as substrates for growth of molecular layers on top, allowing for investigation of properties such as charge transport in molecular crystals near the monolayer limit. Some examples include devices made with few-layer crystalline pentacene on hBN [5], few-layer dioctylbenzothienobenzothiophene molecular crystals on graphene and boron nitride [6] and films of rubrene on hBN [7]. The underlying vdW material can also alter the growth of the molecular layer on top, potentially creating new phases.

In this chapter, we use pentacene as a model aromatic organic molecule. Over the years, pentacene has been the subject of intense study due to its excellent properties such as high charge carrier mobility of above 1 $cm^2V^{-1}s^{-1}$ in both single crystal and thin film devices. [5,8–11] Since the first real-time observations of pentacene growth on silicon and organically-terminated silicon [12], the growth and structure of pentacene layers on various other substrates such as SiO_2, Al_2O_3, Au(111), Ag(110), Ag(111), Cu(110) and Bi(001), among others, have been the subject of many studies. [13–22] More recently, pentacene growth on vdW materials is also being investigated, with promising results. [1,2,5] Here, we study the growth of pentacene layers on two basic vdW systems, i.e. graphite and bulk hexagonal boron nitride (hBN). Graphite is a conductor, chemically rather inert with a hexagonal surface lattice closely matching the aromatic ring structure of pentacene. hBN also has a hexagonal lattice, with similar unit cell parameters to graphite. However, in contrast to graphite, hBN is an insulator, making it a useful substrate for transport studies of molecular adlayers. [5] There have been a few reports of pentacene layer growth on hBN flakes so far. [5,23–25] However, these show discrepancies regarding the structure of the pentacene layers.

We use Low-Energy Electron Microscopy (LEEM) to study the growth of pentacene layers on exfoliated graphite and hBN flakes. We observe the growth dynamics of the pentacene layers in real-time using PhotoElectron Emission Microscopy (PEEM). Furthermore, we probe the local microstructure of the layers, in real-space and diffraction-space, using Low Energy Electron Microscopy (LEEM). We also measure LEEM reflectivity spectra, which are directly related to the unoccupied density of states (DOS) above the vacuum level, of the pentacene layers on top of the two substrates. We analyze the similarities and the differences in the resulting pentacene layers, and discuss the results in terms of the factors affecting layer growth such as the templating effect from the substrate, electronic band structure of the substrate and surface cleanliness.

3.2 Experimental Technique

In the LEEM instrument, electrons are emitted from an electron gun with a kinetic energy of 15 keV. [26,27] Before reaching the sample, an electric field of ~10 kV/mm between an objective lens and the sample (spaced at 1.5 mm) decelerates the electrons to an energy of just a few eV. This interaction energy can be precisely tuned by changing the sample potential with respect to the grounded objective lens. After interaction with the sample, the reflected electrons are re-accelerated by the same electric field and guided toward the detector screen, also passing through an aberration-correcting path along the way. On the detector, a real-space or a diffraction image can be displayed. Furthermore, illumination with a Hg discharge lamp allows for PEEM with UV photons. The photoelectrons are collected in the same way as the reflected electrons from the electron gun. A Knudsen cell evaporator is attached to the sample chamber with line of sight to the substrate surface, allowing for *in situ* pentacene sublimation and growth.

Graphite and hBN flakes were exfoliated onto silicon substrates (with native oxide) with the Scotch tape method. Typical thicknesses of the flakes are several tens of nanometers. Prior to the growth experiments, the samples were heated to ~500˚C overnight in the UHV chamber of LEEM (~1×10^{-9} mbar) in order to clean the flake surfaces. Growth and characterization of the samples were carried out in ultrahigh vacuum (UHV) and at room temperature, unless stated otherwise.

3.3 Results

Pentacene on Graphite:

Figs. 3.1(a) and (b) show PEEM images of a graphite flake prior to and after a period of pentacene sublimation, respectively. On the SiO_2 substrate surrounding the graphite flake, many bright nucleation spots have appeared in Fig. 3.1(b). These areas indicate growth of pentacene in standing-up thin film phase with a herringbone crystal structure (see Fig. 1.1 in chapter 1), which proceeds in the same manner as already reported in the literature for growth of pentacene on flash-cleaned silicon or SiO_2. [12,17] The graphite flake remains dark in PEEM compared to the substrate, however the photoemission intensity on the flake as a whole shows a gradual increase as pentacene is deposited (see Fig. 3.1(g)). The elliptical spot in Fig. 3.1(b) is due to an electron beam imprint after LEEM imaging. Figs. 3.1(c-f) show the developments on the area of the graphite flake indicated by the dashed rectangle in Fig. 3.1(b) during the pentacene sublimation process. The contrast has been readjusted to better reveal the changes. We observe regions of lower intensity gradually growing from the edges of the flake. We will refer to these darker areas as phase A and the rest of the flake as phase B.

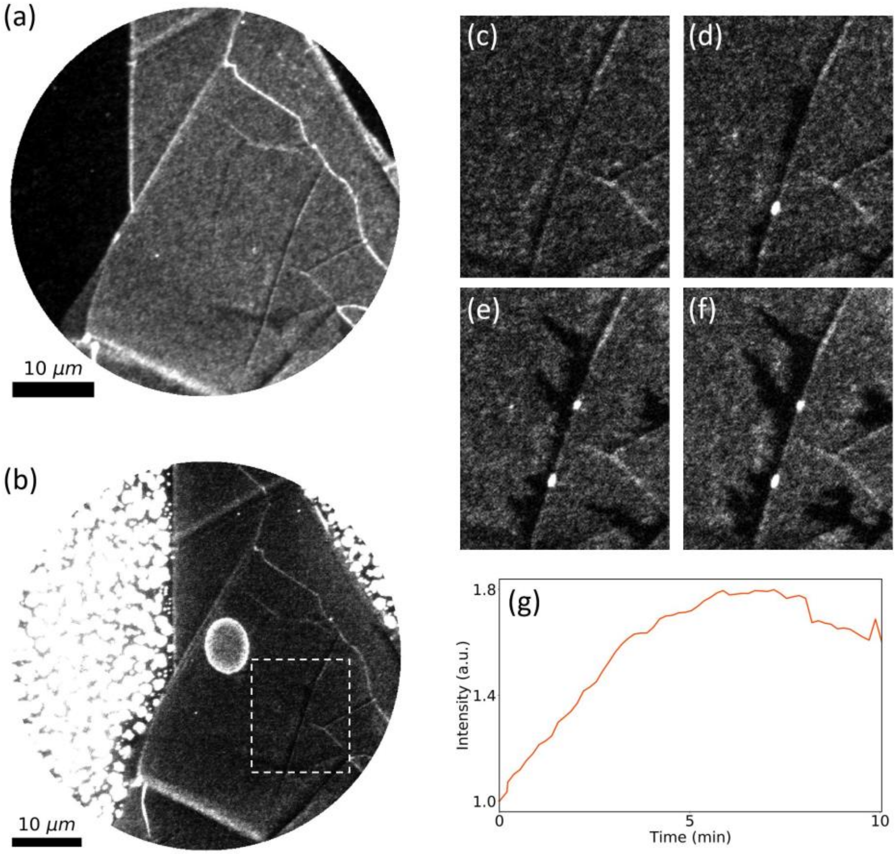

Fig. 3.1 PEEM images of pentacene growth on a graphite flake (grey) on SiO_2 (black) (a) before the start of pentacene sublimation. (b) some time after the start of sublimation. The contrast has been re-adjusted. The elliptical spot is due to beam imprint. (c-f) contrast-readjusted sequence following the changes during sublimation in PEEM images on the area marked with a rectangle in (b). The dark regions in these images are referred to in the text as phase A, and the rest of the flake as phase B. (g) increase in photoemission intensity during the initial stage of sublimation

To investigate the structure of the two different regions on the graphite flake, i.e. phases A and B, we employ the electron beam. Fig. 3.2(a) shows a bright-field LEEM image of an area on the graphite flake, containing both phases. To obtain such an image, an aperture is placed in a diffraction plane to only transmit the 0th-order diffraction spot. Phase A appears as the bright region at the bottom of Fig. 3.2(a) and has the diffraction pattern shown in Fig. 3.2(b). Phase B forms stripe patterns on the rest of the surface of the flake and corresponds to the diffraction pattern in Fig. 3.2(c). To further investigate phase B, we placed apertures on each of the twelve diffraction spots so as to obtain dark-field images. The dark-field images for six of the diffraction spots (numbers 1, 2, 5, 6, 9, 10 in Fig. 3.3(a)) are displayed in Fig. 3.3(d-i). Here, the bright areas only show those pentacene regions that have the crystal orientation chosen. The dark-field images in Fig. 3.3(d-i) and their superimposition in Fig. 3.3(c) reveal that pentacene forms stripe-shaped crystals that appear dark in the corresponding bright-field image of the same area, see Fig. 3.3(b) (and similarly Fig. 3.2(a)). Due to symmetry, dark-field images corresponding to the other diffraction spots (3, 4, 7, 8, 11, 12 as annotated in Fig. 3.3(a)), light up exactly the same areas as those shown in Fig. 3.3(d-i). Hence, pentacene in phase B forms long narrow crystals in six different azimuthal orientations on the surface of the flake. These orientations can be grouped into three pairs, with a rotation of 120° between different pairs and a smaller splitting angle between the diffraction points of each pair. Such pairs in Fig. 3.3(a) are the spots 1-2, 5-6, and 9-10. Interestingly, the domains associated with each pair are also located spatially close to one another, see Figs. 3.3(d-g), (e-h), (f-i).

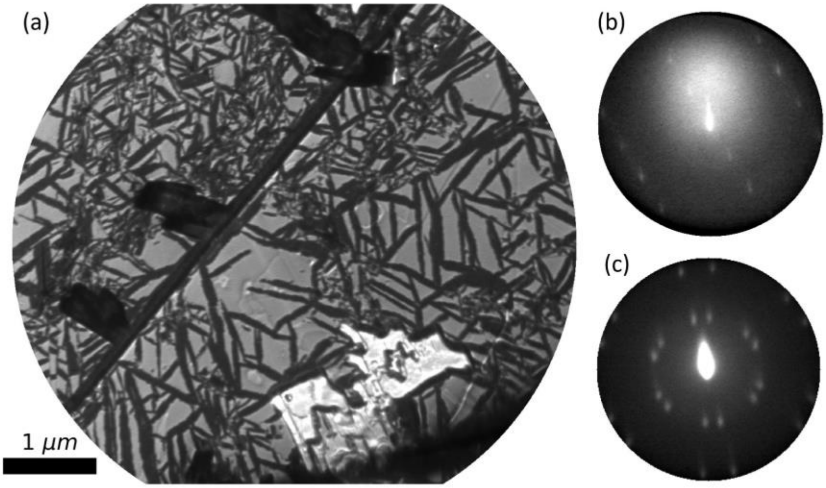

Fig. 3.2 LEEM images of pentacene on graphite. (a) bright-field image of an area containing two different pentacene phases: A (bright at the bottom) and B (the stripe patterns) (b) diffraction pattern corresponding to phase A. (c) diffraction pattern corresponding to phase B.

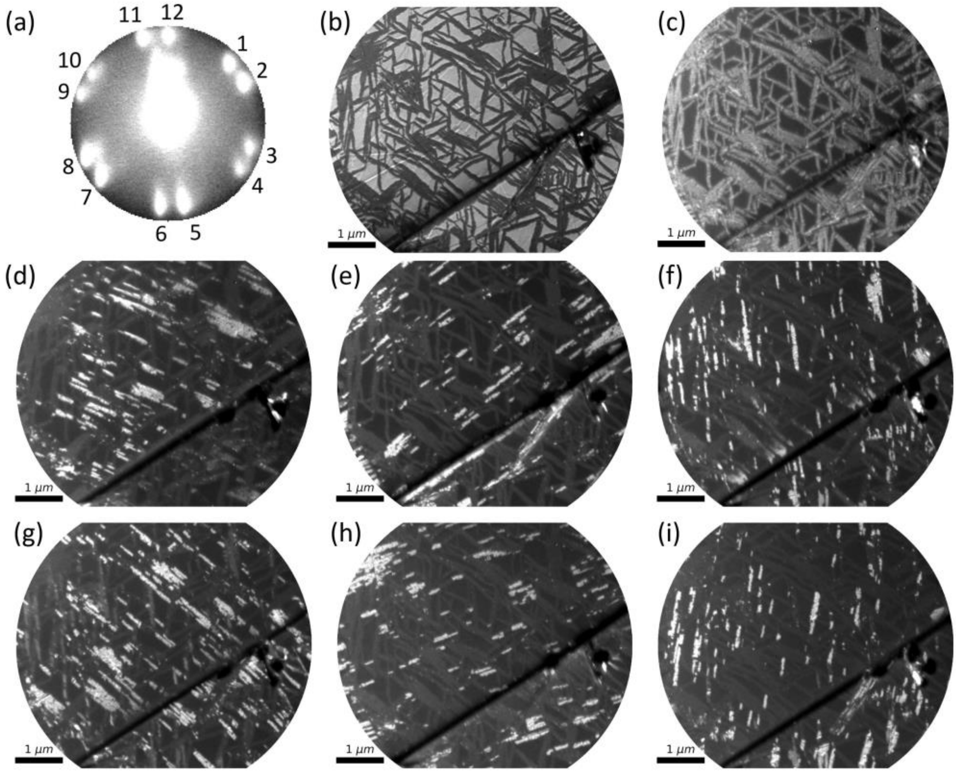

Fig. 3.3 Bright-field and dark-field images of pentacene phase B on graphite. (a) annotation of diffraction spots for dark-field images (b) bright-field image (c) all six dark-field images in (d-i) superimposed. Pentacene areas are bright and create the same pattern as the dark areas in the bright-field image (d-i) dark field images corresponding to diffraction spots 1, 2, 5, 6, 9, 10 with the following correspondence: 1:d, 2:g, 5:e, 6:h, 9:f, 10:i. Areas corresponding to each pair of adjacent diffraction peaks (i.e., 1-2, 5-6, 9-10) are located spatially close to one another. The beam energy used for imaging (e), (d) and (h) is 0.5 eV, while it is 0.6 eV for (b), (f), (g) and (i).

Pentacene on hBN:

Next, we present the dynamics of growth of pentacene layers on top of hBN flakes imaged in real-time with PEEM. In several cases we could also obtain diffraction patterns of the pentacene crystals using the electron beam. Still, the insulating nature of hBN poses challenges towards full characterization with an electron beam.

The initial stage of growth of pentacene on hBN flakes proceeds in a similar fashion to the growth of pentacene layers on graphite. Initially, bright nucleation spots (in PEEM images) appear on the SiO_2 substrate indicating standing-up thin film phase growth. The hBN flake itself remains relatively dark, although it shows some gradual increase in photoemission intensity (see Fig. 3.4(d)). Shining the electron beam on the flakes at this stage reveals a diffraction pattern, indicating adsorption and organization of pentacene on the hBN flake surface. We will refer to this pentacene phase as phase C, with the corresponding diffraction pattern shown in Fig. 3.5(a). Note that Fig. 3.5(a) is very similar to Fig. 3.2(c), i.e. phase B on graphite. Fig. 3.5(a) is obtained by a higher-energy incoming electron beam (20.6 eV), and hence, reveals more of the diffraction pattern compared to Fig. 3.2(c) (obtained by a beam of 2.5 eV electrons). With continued sublimation, what we typically observe in PEEM is the emergence of bright spots on the flakes (with similar intensity to the nucleation spots on SiO_2). These nucleation spots gradually grow until they cover the entire flake. PEEM images in Fig. 3.4(a-c) depict this growth stage. Here, the hBN flake, located to the left of the dashed line, covers about half of the image. The rest of the image corresponds to the SiO_2 substrate. We will refer to the bright areas growing on the hBN flake as pentacene phase D. Diffraction patterns of phase D areas (Fig. 3.5(b)) reveal that they all have the herringbone crystal typical for the standing-up thin film phase of pentacene, similar to growth of pentacene on silicon. [12,17] We have observed pentacene single crystals (in standing-up phase) on hBN flakes with sizes as large as tens of micrometers. Indeed, the diffraction pattern in Fig. 3.5(b) is that of a single crystal within the beam diameter of ~7µm. We have also observed cases where the growth of phase D proceeds in a more branched manner, resulting in a rather polycrystalline film, as evidenced by diffraction. We relate the latter to local substrate contamination.

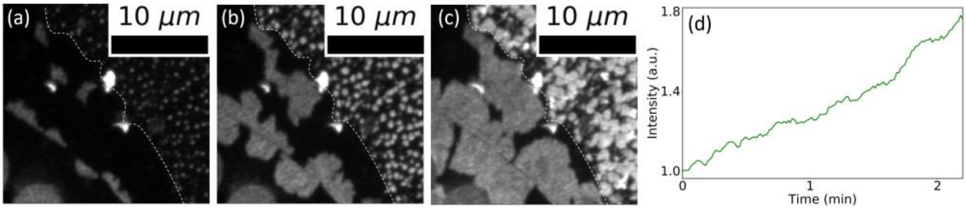

Fig. 3.4 (a-c) PEEM images of growth of pentacene thin film phase on a hBN flake. The flake is located to the left of the dashed line, while to the right of the line is SiO_2. The images show growth of pentacene phase D, which has a higher photoemission intensity than hBN. We also observe nucleation and growth of pentacene on SiO_2 (d) increase in photoemission intensity during formation of phase C before growth of phase D

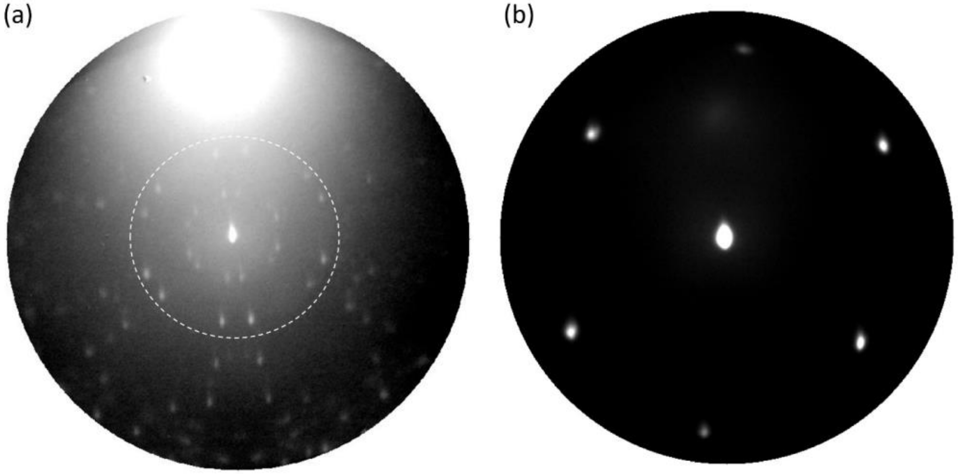

Fig. 3.5 Diffraction patterns of pentacene on hBN flakes. (a) phase C, image intensity is in a log-scale to make higher-order diffraction peaks more visible. The bright circle at the top is due to secondary electrons. The dashed circle encapsulates the lowest-order spots also visible in Fig. 3.2(c) for phase B on graphite. (b) phase D

LEEM-IV spectra of pentacene layers on graphite and hBN:

We used LEEM to also obtain information about the electronic states above the vacuum level for pentacene on graphite and hBN substrates. As mentioned earlier, the energy of the electrons interacting with the sample can be precisely tuned by adjusting the sample potential. The intensity in a real-space LEEM image as well as the intensity of the diffraction spots are functions of incident beam energy. Plotting the intensity of specularly-reflected electrons as a function of beam energy yields a LEEM-IV (intensity vs. voltage) spectrum (referred to above as LEEM reflectivity spectrum). At low electron energies, LEEM-IV spectra are determined mostly by the unoccupied band structure of the sample above the vacuum energy. [28–33] For electron energies at which states are present in the solid and the DOS is high, the incoming electrons have a higher probability of passing into the material, resulting in a lower reflectivity. At energies where the DOS is zero, i.e. at a bandgap, the probability of reflection is higher.

Fig. 3.6 shows LEEM-IV spectra corresponding to pentacene phase B on graphite in black, and the (very similar) phase C on hBN in red. Note that in our experiments, 0 eV corresponds to the vacuum level. At negative energies the incident electrons do not have enough energy to reach the sample, resulting in total reflection. Both spectra show dips at ~1.5 eV and 6 eV.

This figure will be discussed further below along with the pentacene crystal structure in different phases.

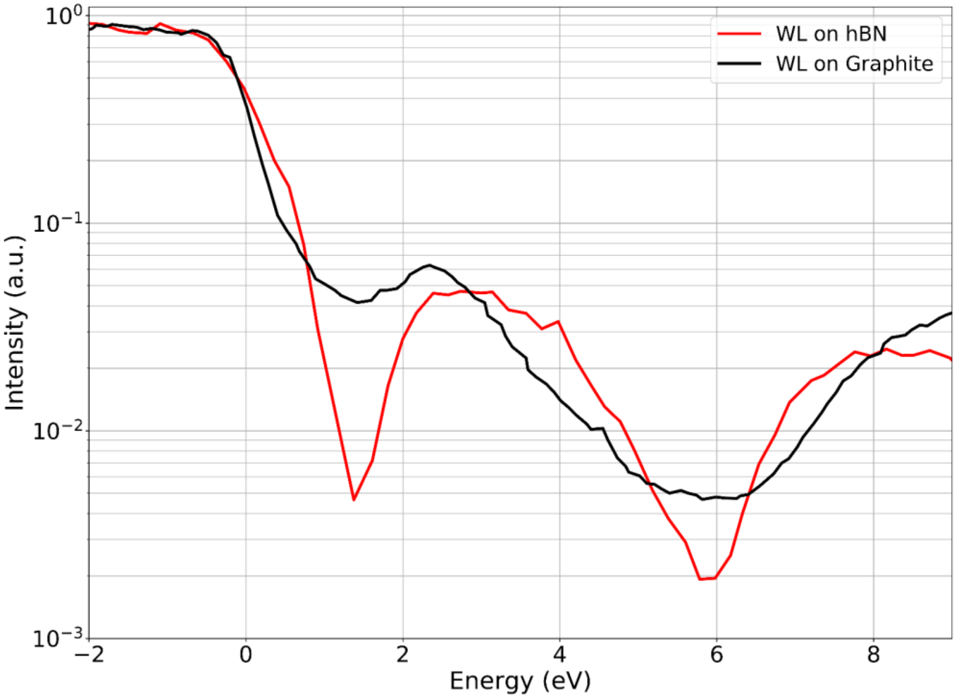

Fig. 3.6 LEEM-IV spectra of pentacene phase B on graphite (black) and phase C on hBN (red)

3.4 Discussion

Now we discuss the structure of pentacene crystals in each of the four phases A-D. First, we focus on phase B (on graphite) and phase C (on hBN). Both of these phases form on flakes in the initial stage of growth, i.e. before formation of phase A (on graphite) and phase D (on hBN), and exhibit striking similarity in their diffraction patterns, see Fig. 3.2(c) and Fig. 3.5(a). Bright-field and dark-field LEEM images of phase B (on graphite) reveal that pentacene forms long narrow crystals in six different orientations on the graphite flake, shown in Fig. 3.3. Similar crystalline domains are expected on hBN flakes due to the similarity of the diffraction images on the graphite and hBN flakes. However, direct imaging with the electron beam on hBN flakes was hampered by charging effects.

To understand the molecular orientation of pentacene in these phases, we need to examine the substrates. Both graphite and hBN have hexagonal crystal lattices, with lattice parameters very similar to each other and to the molecular carbon frame in pentacene. The C-C distance in pentacene varies between 1.35 Å and 1.45 Å [34,35], while it is 1.42 Å in the basal plane of graphite [34]. The B-N bond length in hBN is 1.446 Å. [36] Phase B of pentacene on graphite has previously been observed, [34,37] with the splitting within each of the six diffraction pairs (as discussed above) reported to be 18±3° [34]. Within each crystalline domain the molecules are found to form an oblique lattice with unit cell parameters 17.2±0.5 Å, 7.0±0.5 Å and an angle of 78±3°. [34] STM, UPS and Penning-ionization electron spectroscopy measurements have found that pentacene molecules in this phase are adsorbed with the molecular plane parallel to the surface. [34,38–40] For pentacene on hBN, the existence of a wetting layer (0.5 nm in thickness) with the same structural features as pentacene adsorbed on graphene, has been reported by Zhang et. al., with DFT calculations showing the phenyl rings of pentacene are oriented parallel to the hBN surface. [5] Park et. al. also reported that the pentacene molecules initially lie flat (with zero tilting angle) parallel to the hBN substrate surface. [23]

Hence, we conclude that phases B (on graphite) and phase C (on hBN) have the same crystal structure, in which the molecules lie flat parallel to the flake surface (planar adsorption geometry), forming a substrate-induced crystal lattice (“templating effect”). We will refer to these phases as the wetting layer (WL). The molecules in the WL form six oblique crystals with two-fold symmetries. In our experiments (Fig. 3.2(c) and Fig. 3.5(a)), the splitting angle within each pair of adjacent diffraction spots is 16.7°±0.6° on graphite (phases B) and 17.7°±1.3° on hBN (phase C), close to the 18±3° reported for graphite. [34] Compatible with the lattice mismatch between hBN and graphene, which is ~1.8% [41], the difference in the unit cell parameters of the WL on graphite and hBN in our measurements is also less than 2%.

After formation of the WL, pentacene growth on graphite and hBN proceeds in notably different manners. On graphite, it has been reported that upon further deposition, pentacene forms islands with lateral extensions of several micrometers in which the molecules have a tilted recumbent orientation (28°-32° around their long axis) and crystallize in the Siegrist bulk-phase. [34] Regions with the same diffraction as observed for phase A and dimensions of several micrometers, surrounded by the WL, have also been reported elsewhere, attributed to a bulk phase with tilted recumbent molecules. [37] Hence, we identify phase A as a recumbent bulk crystal phase that grows in islands.

Regarding the growth of pentacene on hBN, literature shows some discrepancies. Similar to our observation of phase D, Zhang et. al. have reported the growth of a standing-up thin-film phase after the WL. [5] In contrast, Amsterdam et. al. did not observe pentacene growth in the thin film phase and found pentacene to have a recumbent “face-on” orientation (similar to phase A) on top of the initial flat-lying molecules. [24] Park et. al. claimed a flat-lying orientation for the first layer, which gradually transitions with increased pentacene layer thickness to a recumbent phase similar to phase A and eventually standing-up orientation (for thicknesses of tens of nanometers). [23] We did not observe such a gradual transition in our experiments, evidenced by the sudden change of diffraction, and the absence of any intermediate diffraction pattern. Finally, Günder et. al. found pentacene deposited on “single crystal” hBN to have recumbent single-crystals similar to the case of pentacene on graphite (phase A), while on hBN “exfoliated flakes” they found pentacene to form elongated tall fibers with recumbent pentacene in addition to thin film phase covering the areas in between the fibers. [25]

To understand the underlying reasons for the different phases observed in our study, we will briefly discuss the factors affecting the structure of an adsorbed molecular layer. The structure of the adsorbed layer is governed by the energetic competition between the strength of the interactions between the molecule and the substrate on the one hand, and between the molecules on the other hand. One factor affecting this competition is the lattice structure of the substrate surface and the possibility of epitaxial layer growth and templating effect. Both graphite and hBN have a hexagonal lattice structure, similar to the molecular frame of pentacene itself, allowing for the possibility of templating effect. This leads to the formation of the WL on both substrates. A second important factor is the density of states (DOS) of the substrate near the Fermi energy. If the van der Waals interactions between the molecules are stronger than their interaction with the substrate, a standing-up orientation for the molecules is expected. This is more likely for the case of a low electron density at the substrate surface, whereas for higher substrate DOS, the molecules may tend to adopt a lying-down orientation. [19] This dependence was clearly demonstrated in a study of pentacene molecules on a Si(111)-(5×2)Au substrate surface, where addition of 0.5 monolayers of Au turned the substrate into a metallic Si(111)-($\sqrt{3}\times\sqrt{3}$)Au surface and changed the pentacene orientation from standing-up to flat-lying. [19] Growth studies of pentacene molecules on various metal substrates such as Ag(110), Au(111) and Cu(110) have also reported a recumbent orientation for the molecules, [14,20–22] while on semiconducting or insulating surfaces such as Si, SiO_2, organically-terminated Si, Al_2O_3, as well as the semi-metallic Bi(001), pentacene molecules tend to stand up. [12,17–19]

The roughness of the substrate surface, in the form of adsorbates or a damaged crystalline structure, is shown to be another factor affecting growth via local disruption of molecule-substrate interactions. Examples in the literature include observation of a standing-up pentacene phase in place of a recumbent orientation due to sputtering of HOPG with

Ar$^+$-ions [34], PMMA residue on graphene films. [42] defective MoS_2 substrates [43], and amorphous carbon substrate [44]. On hBN, Günder et. al. have reported only standing-up molecules on defective substrate surfaces with no evidence of any regions with a recumbent orientation [25]. In contrast, we repeatedly observe the formation of the crystalline flat-lying WL on hBN prior to the growth of the standing-up phase, suggesting that the hBN surface condition is such that the molecule-substrate interactions are not disrupted, leading to the observation of templating effect.

We propose that it is the difference in the strength of electronic interactions between pentacene and the substrate that is responsible for the observation of a tilted recumbent phase (phase A) on graphite, versus a standing-up phase (phase D) on hBN. To substantiate that, we refer to Figure 3.6. The two spectra of the WL, which has the same crystal structure on both substrates, exhibit dips at the same energies. However, the minima are strongly broadened on graphite. This indicates significant electronic interaction (hybridization) of the WL pentacene electron states with graphite bands. The sharp minima seen for the hBN substrate suggest very little hybridization between pentacene and hBN, i.e. we are observing a more “pure” spectrum of the WL pentacene in this case. This implies a relatively small interaction energy for the flat-lying molecules on hBN, as compared to the graphite case. Consequently, a standing-up orientation, with energy gain due to intermolecular hybridization, is expected to be more favorable for hBN than for graphite substrates. This reasoning is consistent with our observations: standing-up thin film phase growth of pentacene on hBN flakes vs. recumbent phase growth on graphite. Still we note that on both graphite and hBN, the templating effect is strong enough for the first molecules arriving on the surface to form a flat-lying WL.

3.5 Conclusions

We have studied the growth of pentacene layers on graphite and hBN flakes in real-time, using low-energy electrons as well as UV photons. The two substrates both possess a hexagonal lattice structure with similar unit cell parameters, approximately matching the molecular frame of pentacene. However, they are very different in their electronic properties. We found pentacene to initially form a flat-lying crystalline wetting layer on both substrates. The diffraction patterns corresponding to this wetting layer are strikingly similar for the two substrates. They imply the existence of six oblique crystals with two-fold symmetries, rotated with respect to each other. This crystal lattice is a result of the substrate templating effect.

Upon further sublimation on graphite, we find pentacene to form crystalline islands nucleating and growing from flake edges, in which the molecules adopt a tilted recumbent orientation. On hBN, we observe pentacene to adopt the standing-up thin film phase configuration, contrasting several previous publications. In some literature reports, the appearance of the standing-up phase is observed on intentionally-roughened (or dirty) substrates and hence said to be a result of disrupted molecule-substrate interactions. This explanation cannot be straightforwardly applied here, because prior to the formation of the standing-up phase on hBN, we repeatedly observe the formation of a crystalline wetting-layer with a substrate-induced crystal structure, hinting at undiminished molecule-substrate interactions.

A different and more fundamental explanation for the standing-up thin film phase on hBN as opposed to the tilted recumbent phase seen on graphite is related to the strength of electronic interactions between pentacene molecules and the substrates. LEEM-IV spectra of the wetting layer on both substrates, related to the unoccupied DOS above the vacuum level, indicate a stronger interaction (hybridization) between pentacene and graphite, as compared to pentacene and hBN. We argue that a strong interaction with the substrate makes the recumbent orientation more energetically favourable, explaining the case of graphite. Vice versa, when molecule-molecule interactions are stronger than molecule-substrate interactions, a standing-up orientation is expected, explaining the case of hBN. The differences between the pentacene crystalline structures on the two substrates confirm the possibility of engineered electronic properties by an appropriate choice of the substrate. Our results also illustrate the multi-faceted way the different factors such as density of states of the surface, templating due to surface lattice structure and cleanliness of the surface determine the growth of molecular layers on top.

References

[1] D. Jariwala, S. L. Howell, K. S. Chen, J. Kang, V. K. Sangwan, S. A. Filippone, R. Turrisi, T. J. Marks, L. J. Lauhon, and M. C. Hersam, *Hybrid, Gate-Tunable, van der Waals p-n Heterojunctions from Pentacene and* MoS_2, Nano Lett. **16**, 497 (2016).

[2] S. B. Homan, V. K. Sangwan, I. Balla, H. Bergeron, E. A. Weiss, and M. C. Hersam, *Ultrafast Exciton Dissociation and Long-Lived Charge Separation in a Photovoltaic Pentacene-*MoS_2 *van der Waals Heterojunction*, Nano Lett. **17**, 164 (2017).

[3] C. Ojeda-Aristizabal, W. Bao, and M. S. Fuhrer, *Thin-Film Barristor: A Gate-Tunable Vertical Graphene-Pentacene Device*, Phys. Rev. B **88**, 035435 (2013).

[4] T. O. Wehling, K. S. Novoselov, S. V. Morozov, E. E. Vdovin, M. I. Katsnelson, A. K. Geim, and A. I. Lichtenstein, *Molecular Doping of Graphene*, Nano Lett. **8**, 173 (2008).

[5] Y. Zhang et al., *Probing Carrier Transport and Structure-Property Relationship of Highly Ordered Organic Semiconductors at the Two-Dimensional Limit*, Phys. Rev. Lett. **116**, 016602 (2016).

[6] D. He et al., *Two-Dimensional Quasi-Freestanding Molecular Crystals for High-Performance Organic Field-Effect Transistors*, Nat Commun **5**, 5162 (2014).

[7] C. H. Lee et al., *Epitaxial Growth of Molecular Crystals on van der Waals Substrates for High-Performance Organic Electronics*, Adv. Mater. **26**, 2812 (2014).

[8] Y. Kato, S. Iba, R. Teramoto, T. Sekitani, T. Someya, H. Kawaguchi, and T. Sakurai, *High Mobility of Pentacene Field-Effect Transistors with Polyimide Gate Dielectric Layers*, Appl. Phys. Lett. **84**, 3789 (2004).

[9] H. Klauk, M. Halik, U. Zschieschang, G. Schmid, W. Radlik, and W. Weber, *High-Mobility Polymer Gate Dielectric Pentacene Thin Film Transistors*, J. Appl. Phys. **92**, 5259 (2002).

[10] O. D. Jurchescu, J. Baas, and T. T. M. Palstra, *Effect of Impurities on the Mobility of Single Crystal Pentacene*, Appl. Phys. Lett. **84**, 3061 (2004).

[11] J. Y. Lee, S. Roth, and Y. W. Park, *Anisotropic Field Effect Mobility in Single Crystal Pentacene*, Appl. Phys. Lett. **88**, 252106 (2006).

[12] FJ. Meyer zu Heringdorf, M. C. Reuter, and & R. M. Tromp, *Growth Dynamics of Pentacene Thin Films*, Nature **412**, 517 (2001).

[13] C. B. France, P. G. Schroeder, and B. A. Parkinson, *Direct Observation of a Widely Spaced Periodic Row Structure at the Pentacene/Au(111) Interface Using Scanning Tunneling Microscopy*, Nano Lett **2**, 693 (2002).

[14] Y. L. Wang, W. Ji, D. X. Shi, S. X. Du, C. Seidel, Y. G. Ma, H. J. Gao, L. F. Chi, and H. Fuchs, *Structural Evolution of Pentacene on a Ag(110) Surface*, Phys. Rev. B **69**, 075408 (2004).

[15] L. Casalis, M. F. Danisman, B. Nickel, G. Bracco, T. Toccoli, S. Iannotta, and G. Scoles, *Hyperthermal Molecular Beam Deposition of Highly Ordered Organic Thin Films*, Phys. Rev. Lett. **90**, 206101 (2003).

[16] S. Lukas, S. Söhnchen, G. Witte, and C. Wöll, *Epitaxial Growth of Pentacene Films on Metal Surfaces*, ChemPhysChem **5**, 266 (2004).

[17] A. Al-Mahboob, J. T. Sadowski, Y. Fujikawa, K. Nakajima, and T. Sakurai, *Kinetics-Driven Anisotropic Growth of Pentacene Thin Films*, Phys. Rev. B **77**, 035426 (2008).

[18] F. J. Meyer Zu Heringdorf, M. C. Reuter, and R. M. Tromp, *The Nucleation of Pentacene Thin Films*, Appl. Phys. A **78**, 787 (2004).

[19] G. E. Thayer, J. T. Sadowski, F. Meyer Zu Heringdorf, T. Sakurai, and R. M. Tromp, *Role of Surface Electronic Structure in Thin Film Molecular Ordering*, Phys. Rev. Lett. **95**, 256106 (2005).

[20] J. H. Kang and X. Y. Zhu, *Pi-Stacked Pentacene Thin Films Grown on Au(111)*, Appl. Phys. Lett. **82**, 3248 (2003).

[21] P. G. Schroeder, C. B. France, J. B. Park, and B. A. Parkinson, *Energy Level Alignment and Two-Dimensional Structure of Pentacene on Au(111) Surfaces*, J. Appl. Phys. **91**, 3010 (2002).

[22] S. Lukas, G. Witte, and C. Wöll, *Novel Mechanism for Molecular Self-Assembly on Metal Substrates: Unidirectional Rows of Pentacene on Cu(110) Produced by a Substrate-Mediated Repulsion*, Phys. Rev. Lett. **88**, 028301 (2002).

[23] B. Park et al., *Anomalous Ambipolar Transport of Organic Semiconducting Crystals via Control of Molecular Packing Structures*, ACS Appl. Mater. Interfaces **9**, 27839 (2017).

[24] S. H. Amsterdam et al., *Tailoring the Optical Response of Pentacene Thin Films via Templated Growth on Hexagonal Boron Nitride*, J. Phys. Chem. Lett **12**, 26 (2021).

[25] D. Gunder, K. Watanabe, T. Taniguchi, and G. Witte, *Van der Waals Bound Organic/2D Insulator Hybrid Structures: Epitaxial Growth of Acene Films on hBN(001) and the Influence of Surface Defects*, ACS Appl. Mater. Interfaces **12**, 38757 (2020).

[26] S. M. Schramm, J. Kautz, A. Berghaus, O. Schaff, R. M. Tromp, and S. J. van der Molen, *Low-Energy Electron Microscopy and Spectroscopy with ESCHER: Status and Prospects*, IBM J. Res. & Dev. **55**, 1:1 (2011).

[27] R. M. Tromp, J. B. Hannon, A. W. Ellis, W. Wan, A. Berghaus, and O. Schaff, *A New Aberration-Corrected, Energy-Filtered LEEM/PEEM Instrument. I. Principles and Design*, Ultramicroscopy **110**, 852 (2010).

[28] J. Jobst, J. Kautz, D. Geelen, R. M. Tromp, and S. J. van der Molen, *Nanoscale Measurements of Unoccupied Band Dispersion in Few-Layer Graphene*, Nat. Commun. **6**, 8926 (2015).

[29] J. Jobst, A. J. H. van der Torren, E. E. Krasovskii, J. Balgley, C. R. Dean, R. M. Tromp, and S. J. van der Molen, *Quantifying Electronic Band Interactions in van der Waals Materials Using Angle-Resolved Reflected-Electron Spectroscopy*, Nat. Commun. **7**, 13621 (2016).

[30] J. B. Pendry, *Theory of Photoemission*, Surf. Sci. **57**, 679 (1976).

[31] J. B. Pendry, *The Application of Pseudopotentials to Low-Energyelectron Diffraction II: Calculation of the Reflectedintensities*, J. Phys. C: Solid State Phys. **2**, 2273 (1969).

[32] V. N. Strocov, E. E. Krasovskii, W. Schattke, N. Barrett, H. Berger, D. Schrupp, and R. Claessen, *Three-Dimensional Band Structure of Layered* $TiTe_2$*: Photoemission Final-State Effects*, Phys. Rev. B. **74**, 195125 (2006).

[33] V. N. Strocov, H. I. Starnberg, and P. O. Nilsson, *Mapping the Excited-State Bands above the Vacuum Level with VLEED: Principles, Results for Cu, and the Connection to Photoemission*, J. Phys.: Condens. Matter **8**, 7539 (1996).

[34] J. Götzen, D. Käfer, C. Wöll, and G. Witte, *Growth and Structure of Pentacene Films on Graphite: Weak Adhesion as a Key for Epitaxial Film Growth*, Phys. Rev. B **81**, 085440 (2010).

[35] R. B. Campbell, J. Monteath Robertson, and J. Trotter, *The Crystal and Molecular Structure of Pentacene*, Acta. Cryst. **14**, 705 (1961).

[36] O. Hod, *Graphite and Hexagonal Boron-Nitride Have the Same Interlayer Distance. Why?*, J. Chem. Theory Comput. **8**, 1360 (2012).

[37] H. W. Liu, A. Al-Mahboob, Y. Fujikawa, N. Fukui, T. Hitosugi, T. Hashizume, Q. K. Xue, and T. Sakurai, *Pentacene Growth on Graphite Investigated by Low-Energy Electron Microscope*, J. Cryst. Growth **312**, 967 (2010).

[38] Y. Harada, H. Ozaki, and K. Ohno, *Selective Observation of Outermost Surface Layer during Epitaxial Growth by Penning-Ionization Electron Spectroscopy: Pentacene on Grayhite*, Phys. Rev. Lett. **52**, 2269 (1984).

[39] H. Fukagawa, H. Yamane, T. Kataoka, S. Kera, M. Nakamura, K. Kudo, and N. Ueno, *Origin of the Highest Occupied Band Position in Pentacene Films from Ultraviolet Photoelectron Spectroscopy: Hole Stabilization versus Band Dispersion*, Phys. Rev. B. **73**, 245310 (2006).

[40] W. Chen, H. Huang, A. Thye, and S. Wee, *Molecular Orientation Transition of Organic Thin Films on Graphite: The Effect of Intermolecular Electrostatic and Interfacial Dispersion Forces*, Chem. Commun., 4276 (2008).

[41] G. Giovannetti, P. A. Khomyakov, G. Brocks, P. J. Kelly, and J. Van Den Brink, *Substrate-Induced Band Gap in Graphene on Hexagonal Boron Nitride: Ab Initio Density Functional Calculations*, Phys. Rev. B **76**, 073103 (2007).

[42] W. H. Lee, J. Park, S. H. Sim, S. Lim, K. S. Kim, B. H. Hong, and K. Cho, *Surface-Directed Molecular Assembly of Pentacene on Monolayer Graphene for High-Performance Organic Transistors*, J. Am. Chem. Soc. **133**, 4447 (2011).

[43] T. Breuer, T. Maßmeyer, A. Mänz, S. Zoerb, B. Harbrecht, and G. Witte, *Structure of van der Waals Bound Hybrids of Organic Semiconductors and Transition Metal*

Dichalcogenides: The Case of Acene Films on MoS_2, Phys. Status Solidi RRL **10**, 905 (2016).

[44] K. Kim, E. J. G. Santos, T. H. Lee, Y. Nishi, and Z. Bao, *Epitaxially Grown Strained Pentacene Thin Film on Graphene Membrane*, Small **11**, 2037 (2015).

Supporting Information

Desorption of pentacene from graphite by heating and repeat of the growth experiment

The sequence of LEEM images in Fig. S3.1 shows the desorption process of the pentacene layers from the graphite surface of Fig. 3.1 as a result of heating of the sample up to a temperature of 600˚C. Fig. S3.1(a), resembling Fig. 3.2(a), shows the two different phases of pentacene on graphite. Note that the pentacene area at the bottom left of the image (phase A) is desorbed completely before the pentacene elsewhere on the sample (phase B) shows any change at all. This shows the interaction between the pentacene molecules and graphite is stronger than between the pentacene molecules in phase A. After the desorption of pentacene, the sample was cooled down and the sublimation of pentacene (from the Knudsen cell) on graphite was repeated. Prior to re-sublimation, diffraction patterns on the flake did not contain any features from pentacene, while real-space images in some areas showed non-homogeneity and possible remnants from the previous sublimation round, as well as electron beam imprints (see Fig. S3.2), indicating that the heating of the sample did not completely clean the surface of the entire flake. The new sublimation of pentacene on the graphite flake proceeded mostly the same as the previous round showing the same developments as shown in Fig. 3.1. However, this time, also regions with high photoemission intensity appeared on the flake, similar to those which had appeared on the substrate, as can be seen in Fig. S3.3(a). As expected, the diffraction pattern corresponding to these regions, shown in Fig. S3.3(b), is the same as observed for standing-up thin film pentacene phase.

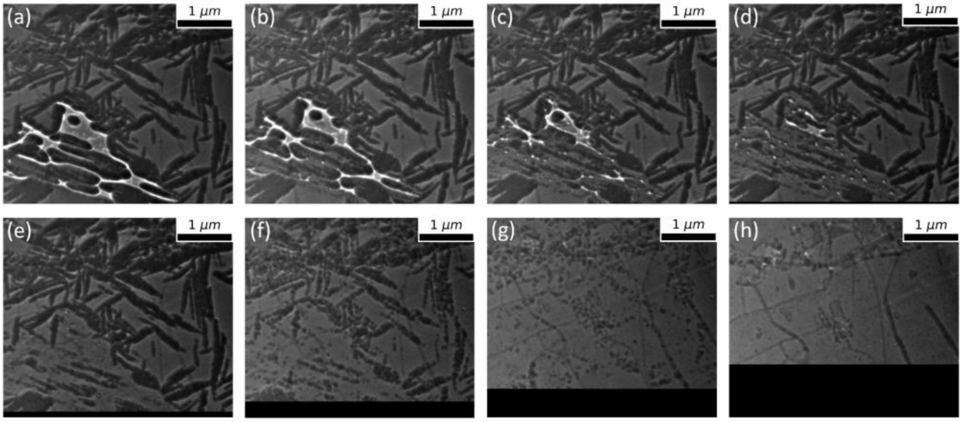

Fig. S3.1 Gradual desorption of pentacene from a graphite flake as a result of heating. Note that before the bright feature at the bottom left (phase A) has evaporated, no change at all can be seen on the rest of the surface (phase B)

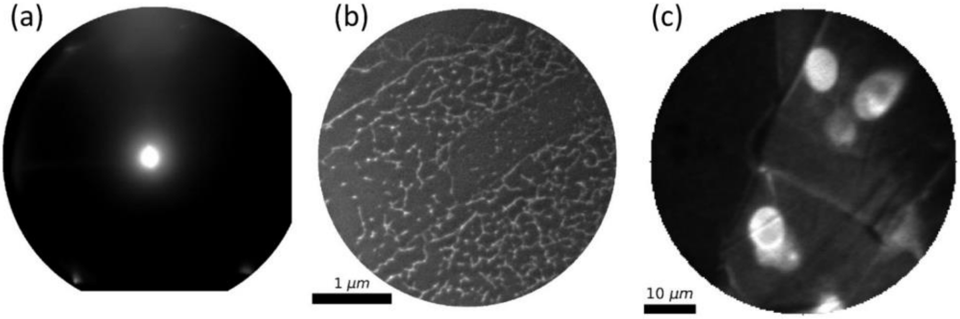

Fig. S3.2 Images of the graphite flake after heating and desorption of pentacene (a) diffraction pattern showing diffraction spots of graphite with no trace of the pentacene crystal diffraction patterns shown in Fig. 3.2(b-c) (b) Real-space image showing features on the surface of the flake, possible remnants from the previous sublimation round (c) beam imprints in a PEEM image

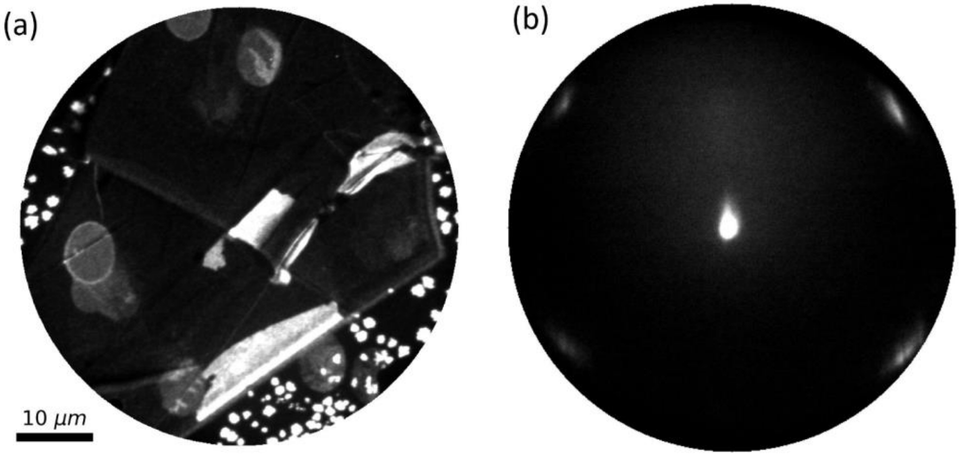

Fig. S3.3 Re-sublimation of pentacene on the same graphite flake. (a) PEEM image showing regions of very high intensity on the flake (b) The diffraction pattern corresponding to such regions

4

Low-Energy Electron Irradiation Damage in Few-Monolayer Pentacene Films *

Abstract

Crystalline films of pentacene molecules, 2-4 monolayers in thickness, are grown via *in situ* sublimation on silicon substrates in the ultrahigh vacuum chamber of a low energy electron microscope. It is observed that the diffraction pattern of the pentacene layers fades upon irradiation with low-energy electrons. The damage cross-section is found to increase by more than an order of magnitude for electron energies from 0 eV to 10 eV, and by another order of magnitude from 10 eV to 40 eV. Close to 0 eV, damage is virtually nil. Creation of chemically reactive atomic centers after electron attachment or impact ionization is thought to trigger chemical reactions between neighboring molecules that gradually transform the layer into a disordered carbon nanomembrane. Additionally, diminishing of spectroscopic features related to the unoccupied band structure of the layers, accompanied by loss of definition in real-space images, as well as an increase in the background intensity of diffraction images during irradiation point to chemical changes and formation of a disordered layer.

---

* This chapter has been published as “Low-Energy Electron Irradiation Damage in Few-Monolayer Pentacene Films”, A. Tebyani, F.B. Baalbergen, R.M. Tromp, S.J. van der Molen, J. Phys. Chem. C 125, 26150 (2021)

4.1 Introduction

Interaction of low-energy electrons (LEEs) with organic materials is of importance in several areas of research and applications. One important example is interaction of biological matter with ionizing radiation. Regardless of the radiation source (electrons or photons), exposure leads to generation of secondary electrons with relatively low energies (below 20 eV). These electrons are responsible for a substantial part of the damage to the organic sample. [1,2] Knock-on displacement of atoms and creation of structural defects occur with electrons of much higher energies (threshold of ~86 keV for knock-on displacement in graphene [3]). Techniques such as low-energy TEM [4], cryo-electron microscopy [5–8], or encapsulation [9] are attempts to reduce the damage and to extend sample lifetime. [10] An understanding of the energy dependence of interaction of LEEs with organic samples is beneficial for designing experiments that cause less damage to the sample under study. Another key example is formed by organic Self-Assembled Monolayers (SAMs), which can be used to modify chemical, physical, and mechanical properties of surfaces. Irradiation of SAMs with LEEs can cause (desirable) chemical changes, transforming SAMs into carbon nanomembranes (CNMs) with different properties. [11–16] Hence, knowledge of the interaction of LEEs with molecules is important in designing SAMs towards the wanted functionality after exposure to LEEs. Synthesis of carbon-based (nano)materials by utilizing an electron beam is a similar application. [17–20] Another technologically important example of interaction of LEEs with organic matter is in e-beam lithography, where electrons are used to cause chemical changes in the resist film. A detailed understanding of the interaction of low-energy (secondary) electrons with the resist is essential for control over the properties of the exposed area, as well as sharpness of the written patterns and overall quality of the lithography process. Knowledge of the role of secondary electrons, which generally have low energies, is also of great importance to understand and improve extreme ultraviolet (EUV) lithography, generally considered the key lithographic technology for the next decade(s). [21,22]

In this work, we use Low-Energy Electron Microscopy (LEEM) to study the interaction of LEEs with crystalline layers of pentacene grown on a silicon (111) substrate. In LEEM, the energy of the electrons interacting with the sample can be tuned in the range 0-100 eV (with respect to the vacuum energy) with 0.25 eV energy spread. Scattering of LEEs from pentacene layers provides information about the surface structure through diffraction, and also reveals spectroscopic features related to the unoccupied band structure [23,24], as well as electronic excitations in electron energy loss spectra. [25] The pentacene layers studied, two to four monolayers in thickness, are grown *in situ* in the ultrahigh vacuum (UHV) chamber of the microscope. Growth is monitored in real-time via both LEEM and

Photo-Electron Emission Microscopy (PEEM). Not only does this offer a high degree of control over pentacene thin film growth, it also ensures that the layers are not at any point contaminated due to exposure to air. The pentacene layers are exposed to electrons with a defined energy, and the main observation reported here is fading of the pentacene diffraction intensity due to beam-induced damage to the crystalline structure. To quantify the damage, line profiles of diffraction spots are analyzed over time. We obtain electron cross-sections for destruction of the pentacene lattice for electron energies between 0 eV and 40 eV, and find that the cross-section becomes vanishingly small for electron energies close to 0 eV. Spectroscopic information on the unoccupied band structure and electron energy loss spectra were also obtained and their evolution upon irradiation was investigated.

4.2 Experimental Technique

A schematic of the LEEM instrument is shown in Fig. 4.1(a). Electrons traveling from the cold-field emission gun through the microscope column with a kinetic energy of 15 keV are deflected towards the sample by magnetic prism 1. The sample voltage is set at -15 kV + V_0 so that the electrons are decelerated just before they interact with the sample to a kinetic energy of $eV_0 + \Delta\Phi$, in an electric field of approximately 10 kV/mm. $\Delta\Phi$ represents the difference between the work functions of the sample and the electron gun. After interaction with the sample, some of the electrons are back-reflected. These electrons are re-accelerated by the same electric field towards the magnetic prism and are deflected towards the detector via an aberration-correcting path comprised of magnetic prism 2 and the correcting electron mirror optics. [26] It is possible to project either the real-space or the diffraction-space image on the detector screen. A high-pressure Hg UV lamp attached to the sample chamber allows for imaging with photoelectrons (PEEM). In addition, a Knudsen cell evaporator is connected to the sample chamber with line of sight to the sample surface. By heating the cell, pentacene (purchased from Sigma Aldrich, with a purity of 99.995%) is sublimated towards the sample for *in situ* thin film growth. The growth of pentacene layers on silicon has been explored in detail in the literature. [27–29] (see also Fig. 4.1(b-c)) By placing a slit in the beam path in a diffraction plane between the objective lens and magnetic prism, Electron Energy Loss Spectroscopy (EELS) data can be obtained. [25] Electrons with different energies are dispersed by the magnetic prism, and hence spectra showing electron intensity vs energy are observed directly on the image screen.

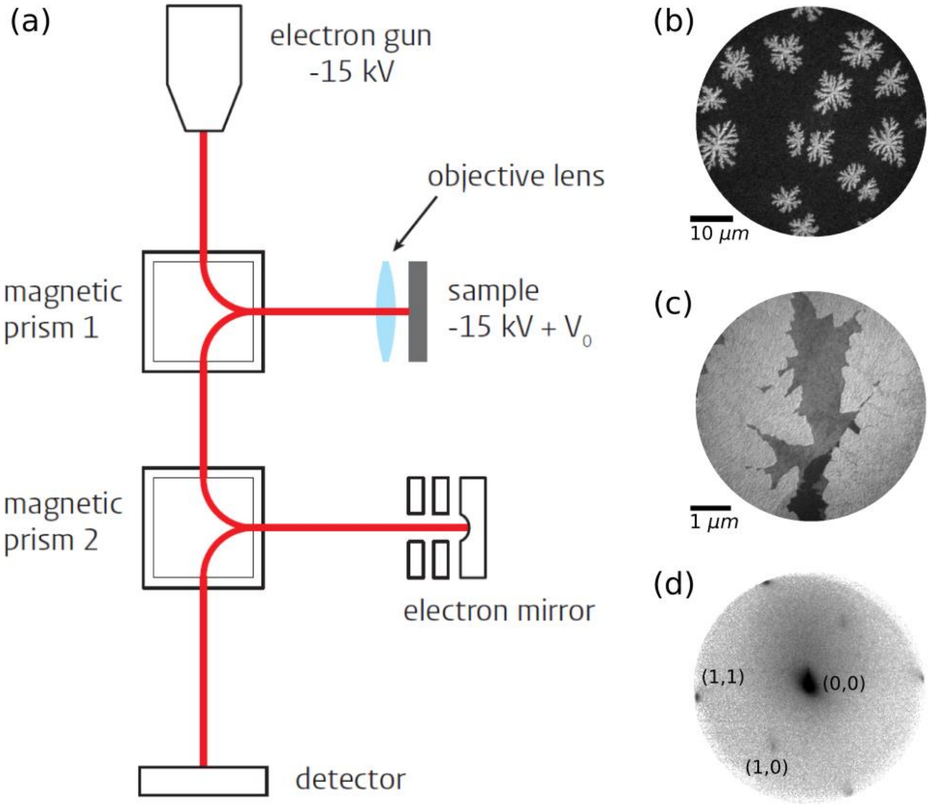

Fig. 4.1 Low-Energy Electron Microscopy (LEEM). (a) A schematic of the LEEM instrument. The red line shows the path traversed by the electrons from the cold-field emission gun to the detector. The electrons are decelerated to an energy close to 0 eV by the electric field between the objective lens and the sample, approximately 10 kV/mm in strength. The precise energy of the electrons upon interaction with the sample is tuned by V_0. The electron mirror corrects lowest-order aberrations. (b) PEEM image showing nucleation of pentacene molecules on the substrate surface and start of growth of the first pentacene layer with herringbone crystal structure (c) Bright-Field LEEM image obtained with a beam of 1.3 eV electrons. The contrast indicates different layer thickness. (d) Low-Energy Electron Diffraction (LEED) pattern of herringbone crystal structure of a pentacene film, with different diffraction orders annotated. Intensities of diffraction spots are in logarithmic scale.

Growth of the pentacene layers *in situ* in a UHV pressure of ~1.0×10^{-9} mbar and below, and keeping them in the same pressure during the entire measurements, ensures cleanliness of the surface. For obtaining the data presented here, an aperture is placed along the illuminating beam path to confine the beam to a smaller, more homogeneous area (below 2 µm in diameter) on the pentacene layer. The diffraction pattern corresponding to the chosen area is recorded over time as the layer is exposed to the electron beam. Recordings are made for exposures to electrons with incident energies in the range 0-40 eV. The measurements are carried out at room temperature.

The total emission current of the electron gun is measured via an anode aperture that transmits about 0.1% of the emitted electrons. The ratio between the beam current that passes through this aperture and the total emission current was determined by placement of an aperture along the magnetic prism diagonal and measurement of the aperture current with a Keithley Picoammeter when the aperture blocked the beam. Electron beam current densities used are 3-45 pA/μm^2, corresponding to ~19-281 $e^-/nm^2/sec$. The surface density of pentacene molecules is about 4.74 molecules/nm^2. [29]

4.3 Results

Pentacene layers grow on silicon (111) substrates in a thin-film phase with a herringbone crystal structure (see Fig. 1.1 in chapter 1). [29] The corresponding diffraction pattern is shown in Fig. 4.1(d). In Fig. S4.1 (Supporting Information, Part A) and the inset in Fig. 4.2, we show a measurement of a typical diffraction spot and its line profile. The line profile is taken in the direction orthogonal to that of the magnetic prism dispersion (which is in vertical direction in Fig. S4.1) in order to avoid asymmetric broadening of the line profile. Next, the background is removed from the images by the following procedure: First, a Fourier transform of the diffraction image for each frame of the recording is generated. Then, a median filter is applied to the Fourier transformed image. This operation removes the low-frequency noise and the background present in the diffraction image. Finally, the filtered image is transformed back and a new diffraction image with reduced noise and background is obtained. The full process is illustrated in Fig. S4.1. Next, Lorentzian functions are fitted to the line profiles of the diffraction spots for each frame of the recording; see the inset in Fig. 4.2. To quantify the rate of fading of the diffraction pattern, we plot the amplitudes of the Lorentzian fits as a function of the cumulative electron dose (number of electrons per nm^2). Fitting an exponential function to these amplitudes yields the cross-section for damage to the pentacene crystal lattice at the incident electron energy corresponding to the recording; see Fig. 4.2. The fitted function has the form $Ae^{-\sigma \cdot D} + B$, where D is the cumulative dose in units of number of electrons per nm^2, σ is the damage cross-section in nm^2, and A and B are constants. By repeating the procedure described above for recordings corresponding to different incident electron energies, we obtain damage cross-sections as a function of electron energy. Fig. 4.3 shows the results of this analysis on diffraction peaks of different orders, obtained from a representative sample, four pentacene monolayers in thickness. Note again that electron energies are determined with respect to the vacuum energy.

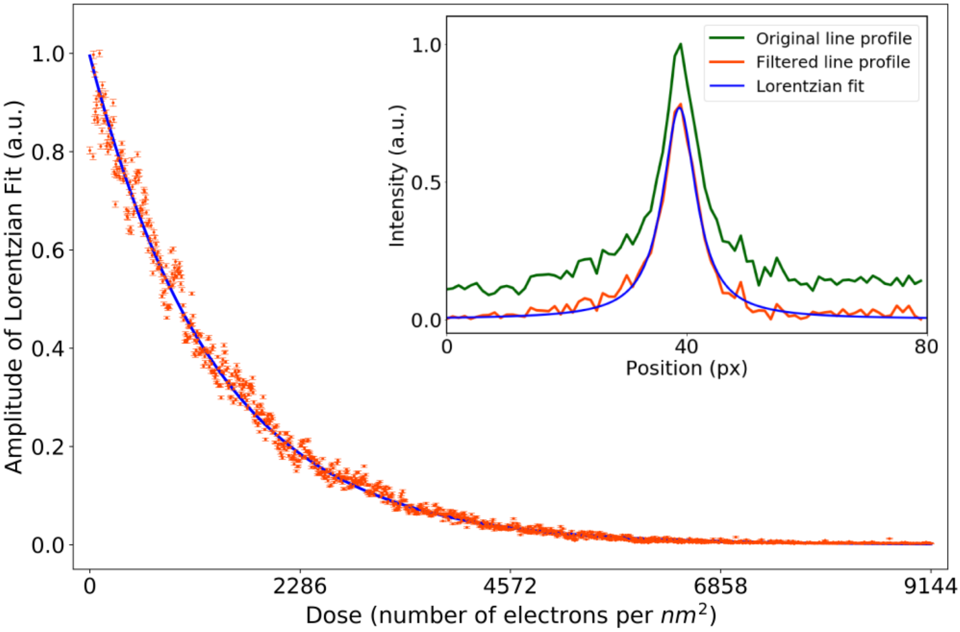

Fig. 4.2 Orange points: Amplitudes of Lorentzian fits to a (1,1) diffraction peak as a function of dose. The latter is proportional to irradiation time. Solid line: exponential fit of the form $Ae^{-\sigma \cdot dose} + B$ to the decay of the peak amplitude. A and B are constants. From the fit, we determine the damage cross-section, defined as σ in the exponent. The pentacene film is 4 monolayers thick and is irradiated with 10 eV electrons. The beam current density is 2.96 pA/μm^2. The inset shows line profile of a (1,1) diffraction peak before and after filtering, corresponding to Fig. S4.1. Lorentzian fit to the diffraction peak after filtering is also depicted.

Fig. 4.3 shows that the damage cross-section decreases sharply below 10 eV. A similar behavior is reproduced in datasets from several other samples (Figs. S4.2-S4.4, Supporting Information, Part B). For the dataset represented in Fig. 4.3, the intensity of the diffraction peaks did not decrease during the duration of the recording for electron energies below 5.5 eV. In some of the other datasets, decays were observed down to about 2 eV, with the damage cross-section becoming vanishingly small for few-eV electrons. In all cases a sharp decrease (in an almost exponential manner) in damage cross-section is observed as the energy of the incident electrons decreases below 10 eV. Changes in damage cross-section span up to two orders of magnitude for electron energies starting from the observed damage threshold for the dataset up to 10 eV. The damage cross-section increases by about another order of magnitude for electron energies between 10 eV and 40 eV, and in general shows a monotonic behavior. Finally, damage cross-sections obtained from higher-order diffraction peaks are consistently higher than those obtained from lower-order diffraction peaks, both in Fig. 4.3 and in the results from several other samples with very few exceptions. This observation indicates that high-resolution information, i.e. short-range order, is lost before loss of order across the entire irradiated area. Faster fading of higher-order diffraction peaks has also been reported in the literature. [10,30] For completeness, Fig. S4.5 (Supporting Information, Part C) shows a typical example of changes in the width of the Lorentzian fits over time, exhibiting a generally increasing trend.

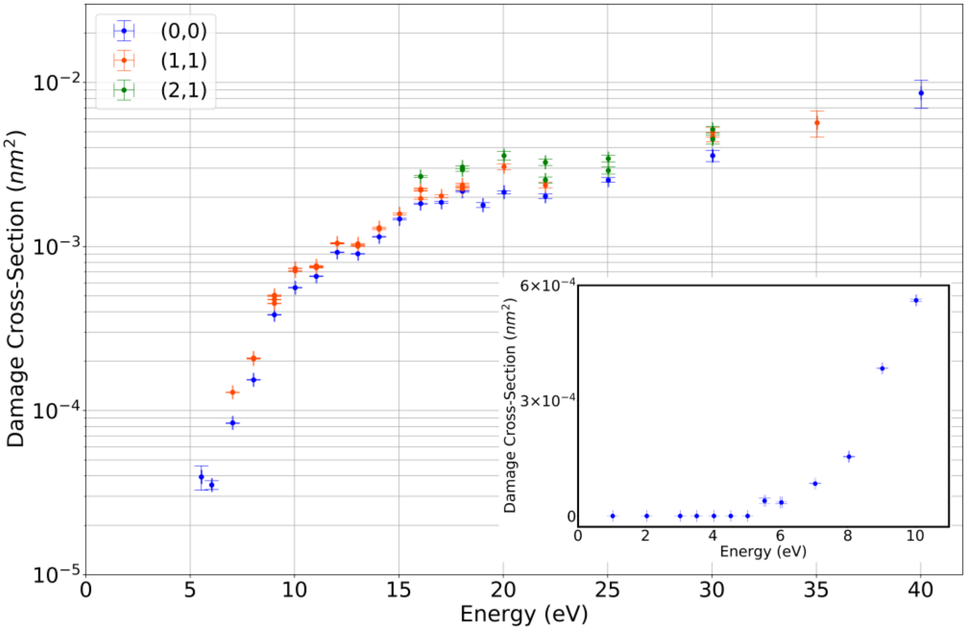

Fig. 4.3 Damage cross-sections (see Fig. 4.2) of different-order diffraction peaks versus incident electron energy for a pentacene sample with thickness of 4 monolayers. The beam current density used for obtaining the cross-sections is 2.96 pA/µm^2. The inset shows the damage cross-section for datapoints up to 10 eV in linear scale, including energies for which no decay in diffraction intensity was observed.

Changes induced in the film upon irradiation are also observed in real-space. During irradiation, the structure of the layer gradually loses definition and sharpness and becomes darker in bright-field images. To obtain bright-field images, a contrast aperture is placed around the 0th-order diffraction peak to exclude all the electrons which are not specularly reflected, including secondary electrons. After a sufficiently long exposure time and disappearance of the diffraction pattern, the irradiated areas look very dark for all incident electron energies in bright-field images (Fig S4.6 in Supporting Information, Part D). This change in the irradiated regions is also reflected in the spectroscopic features, as described below.

In general, the number of electrons reflected from an area of the sample, and hence the image intensity, is a function of the incident electron energy. By plotting the intensity versus the incoming beam energy, we obtain an intensity-vs-voltage plot, or in short, a LEEM-IV curve. A LEEM-IV curve is a spectroscopic fingerprint of the probed area, and is largely determined by the unoccupied band-structure of the sample above the vacuum energy. [23,24] The reflected specular intensity is directly related to the density of states (DOS) in the solid along the surface normal. A low density of unoccupied states lowers the probability that incoming electrons enter the solid, resulting in higher reflectivity. Conversely, a high density of states leads to a low reflectivity. Fig. 4.4 shows LEEM-IV curves of a crystalline pentacene film, three monolayers in thickness, measured repeatedly on the same area. These LEEM-IV curves follow the intensity variations of the 0th-order diffraction peak, corresponding to specularly-reflected electrons. After each subsequent measurement, the features of the LEEM-IV curve are diminished, meaning that a smaller fraction of the incident electrons undergo specular reflection. The latter is consistent with our previous result that irradiated areas appear gradually darker in real-space images. For an area exposed to the electron beam for a sufficiently long time, all the IV curve features are lost, as can be seen in Fig. 4.4. This indicates that the states associated with the original pentacene layer disappear, suggesting a new material with a broad set of unoccupied states is being formed. This is the reason irradiated areas appear very dark with no intensity change in bright-field real-space images obtained by incident electrons of any energy. In a related observation, the background intensity in diffraction images is noted to increase during irradiation (Fig. S4.7, Supporting Information, Part E), indicating that more electrons are scattered incoherently after a period of exposure to the beam.

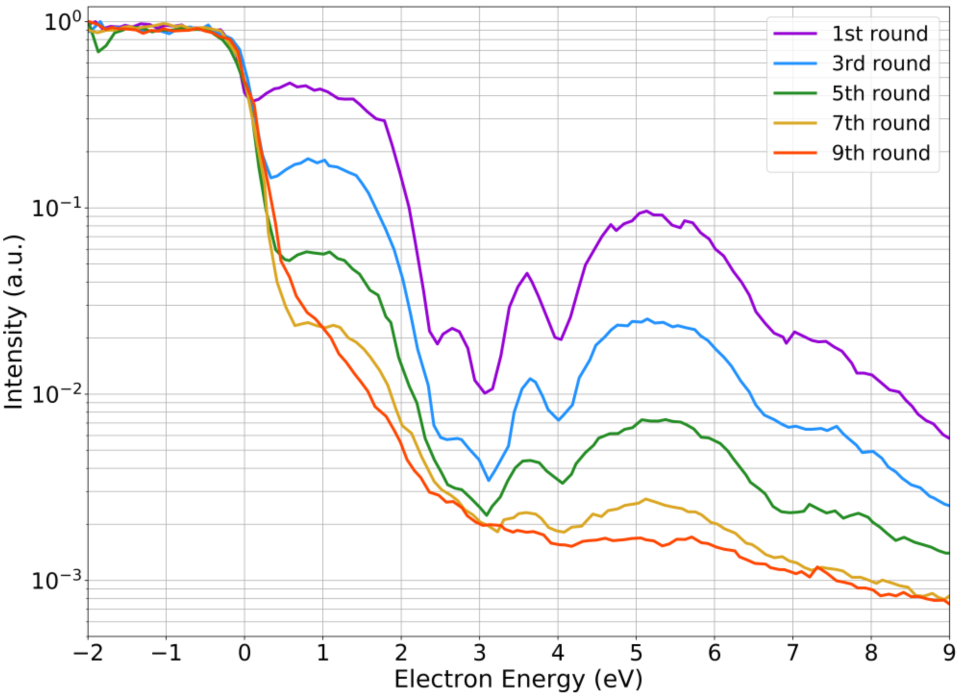

Fig. 4.4 Diminishing of LEEM-IV features through consecutive measurements. The LEEM-IV curves correspond to the intensity of the (0,0) diffraction peak of a sample with film thickness of 3 monolayers. The beam current density for the measurements is 5.3 pA/μm^2.

Finally, Fig. S4.8 (Supporting Information, Part F) shows the changes in the electron energy loss spectra after a period of exposure to the beam. It can be inferred that the energy distribution of the secondary electrons is such that the vast majority of them have an energy of less than ~4 eV. Considering our observations about the damage cross-section in pentacene layers, it can be concluded that the secondary electrons generated during irradiation contribute minimally to the damage cross-sections for the incident electron energies in our study.

4.4 Discussion

To analyze the full energy dependence of the damage cross-section curve depicted in Fig. 4.3, we consider possible mechanisms of interaction of molecules with incoming electrons having different energies. At few-eV incident energies, “electron attachment” is regarded as the primary mechanism. It can lead to either auto-detachment of the electron, leaving the molecule in an excited state, or fragmentation of the molecule, i.e. the case of Dissociative Electron Attachment (DEA), or formation of reactive negatively-charged centers via rearrangement of charge within the molecule. The relative probability of each of these scenarios depends on the energetic landscape (potential energy surfaces) of the molecule. Electron attachment and formation of anions at low electron energies has been investigated with different techniques and reported for pentacene and similar molecules in the literature. In particular, mass-spectroscopic studies of vapors of pentacene molecules bombarded with low-energy electrons found that singly charged anions of pentacene could be detected for electron energies in the range 0-3 eV, demonstrating electron attachment at such energies. [31] In the same study, neutral pentacene molecules were detected, also up to 3 eV. In another similar mass-spectroscopic study [32], singly charged anions of pentacene molecules with one hydrogen missing were detected starting from ~ 5 eV, up to ~ 11 eV, with much smaller quantities (about 100 times lower) found in the range 3-5 eV. Singly charged negative anions of other polycyclic aromatic hydrocarbons with one hydrogen missing were also detected in several other studies [33,34], showing a distribution centered around 8 eV, and becoming increasingly smaller above 10 eV and below 6 eV. In a study of vibrational states of gaseous benzene molecules probed with incident electrons, the cross-section for excitation of the carbon-hydrogen bond is shown to have a resonance between 5.5 eV and 10 eV, with a peak at 8 eV, accompanied by a smaller resonance between 4 eV and 5.5 eV. [35] Electron bombardment of an aromatic thiol ($Au-S-CH_2C_6H_5$) was found to result in creation of H_2 molecules, with the yield becoming drastically smaller below ~6 eV. [36] Irradiation of p-terphenylthiol SAMs with LEEs was found to show a resonance centered at 7.2 eV for excitation of carbon-hydrogen bonds. [37,38]

From these results, we conclude that at energies in the range from 0 eV up to about 10 eV, the incoming electrons can attach to the pentacene molecules, however, towards the lower end of the range, the molecules most probably auto-detach the extra electron, and the temporary attachment is much less likely to lead to fragmentation of the molecule. Towards the upper end of the 0-10 eV range, electron attachment will leave the molecule in a chemically reactive state with consequences that are discussed further below. The new reactive state of the molecule can be a result of scission of the carbon-hydrogen bond and removal of a hydrogen atom from the molecule, charge reorganization after electron attachment or an energetically excited state after detachment of the electron. The increased resistance towards damage at very low electron energies is in contrast to results from similar LEEM experiments on PMMA and the molecular organometallic EUV resist known as tin-oxo cage [21,22], for both of which it was found that electrons with energies all the way down to 0 eV (with respect to vacuum energy) can cause chemical changes in the resist layer. Lower susceptibility of aromatic organic molecules towards irradiation damage, compared to their derivatives which contain also single bonds, such as the case of pentacene and bis(triisopropylsilylethynyl) (TIPS) pentacene [39,40], or compared to saturated molecules [41], has already been reported in various studies. In agreement with our observations on pentacene layers, an Inverse Photo-Emission Spectroscopy (IPES) study on pentacene films also found no remarkable change in the spectra when electrons with kinetic energy of 5 eV were used, in contrast to the case for 10 eV electrons for which spectral changes were observed. [42]

As the incident energy of the electrons increases above a few eV, also other mechanisms for interaction between the incoming electrons and the pentacene molecules become possible. For pentacene molecules bombarded with electrons, a threshold of 6.6 eV has been experimentally measured for ionization of pi-electrons of pentacene [43–47], with more ionizations as the incident electron energy increases. [44] Ionization of sigma bonds in pentacene is identified to start at approximately 11 eV [44], with the ionization leading to scission of carbon-hydrogen bonds starting at 15.2 eV. [43] In a related study, the ionization cross-section in benzene shows a steep rise from incident electron energy of ~9 eV (the ionization threshold in benzene) up to around 100 eV. [48] Similar behavior is expected to be the case for pentacene but starting from a lower ionization threshold. The availability of more pathways for interaction between the incident electrons and the molecules is manifested in the continuous increase of the damage cross-section versus electron energy observed in Fig. 4.3. However, DEA is assumed to contribute to damage in pentacene mostly for electron energies below ~11 eV, given the diminished amounts of singly charged anions of pentacene molecules with one hydrogen missing detected at energies higher than ~11 eV, as found in Ref. [32]. Indeed, electron attachment and formation of a transient negative ion is expected to happen for electron energies below 15 eV. [1,2,49] At higher incident electron energies, impact ionization is expected to be the dominant interaction mechanism.

The cross-sections for damage to the pentacene crystal lattice obtained here are within the range of cross-sections reported in literature for interaction of electrons with gaseous benzene. [48,50–53] A lower damage cross-section for pentacene films could be expected due to higher irradiation damage resistance of pentacene compared to benzene, as a result of a higher degree of electron delocalization both within the molecule and also within the layer with neighboring molecules.

Irradiation with electrons has been reported in various studies to lead to cross-linking within the organic layer, such as the case of 4'-nitro-1,1´-biphenyl-4-thiol SAM (incident electron energies 2.5-100 eV) [54], 1,1’-biphenyl-4-thiol (BPT) SAM (incident electron energy 50 eV) [55], $CH_3(C_6H_4)_2(CH_2)_nSH$ SAM (incident electron energy 10 eV) [56], and p-terphenylthiol SAMs (incident electron energies 6 eV and 50 eV). [37,57] Hence, we propose that the mechanism behind damage to the pentacene crystalline structure is formation of chemical bonds between nearby molecules initiated by reactive atoms. The reactive atoms are created either as a result of (dissociative) electron attachment at lower energies, or impact ionization at energies higher than thresholds for scission of various bonds. This process, repeated many times across the layer, will eventually result in polymerization of the molecular film, and creation of a CNM. At higher electron energies, scission of different bonds, fragmentation of molecules and drifting away of the fragments are also possible.

This conclusion is also compatible with the LEEM-IV measurements, presented in Fig. 4.4. In the first measurement, the LEEM-IV curve shows reflection maxima at about 2 and 5.5 eV, separated by a pronounced minimum (low reflectivity) at about 3.5 eV. As shown previously [23,24], high electron reflectivity corresponds to a gap in the electronic band structure, i.e. low density of states in the conduction band above the vacuum level. The disappearance of the reflection maxima at these energies with consecutive exposures indicates a loss of crystal order, and thereby a loss of electronic structure, including these bandgaps. Given that orbital energies are affected/-shifted corresponding to their environment, creation of a disordered CNM is expected to lead to a more dispersed set of energies for unoccupied orbitals. This in turn results in low reflectivity and featureless LEEM-IV curves for irradiated pentacene areas compared to pristine areas showing clear dips and peaks. Polymerization of the layers, resulting in a more rugged surface, also explains loss of definition in the real-space images upon irradiation, as well as the increase in the background intensity (noncoherent scattering) in diffraction images observed in Fig. S4.7.

4.5 Conclusions

Crystalline thin films consisting of 2-4 pentacene monolayers are grown on silicon substrates *in situ* in the UHV chamber of a low-energy electron microscope. It is observed that irradiation of the films with low-energy electrons leads to fading of their diffraction pattern at a rate that depends on the energy of the incident electrons. Cross-sections for damage to the crystalline structure of the thin films are obtained by analysis of the evolution of the diffraction peaks over time. The results indicate that the damage cross-section increases by more than an order of magnitude for electron energies from 0 eV to 10 eV, and by another order of magnitude from 10 eV to 40 eV. Spectroscopic LEEM-IV measurements also show gradual disappearance of unoccupied band structure as a result of continued irradiation. These observations are explained by the different mechanisms that govern the interaction of pentacene molecules with incoming electrons having different energies. Electron attachment is proposed as the dominant mechanism at low energies, and a contributing factor to damage up to ~10 eV. It can lead to scission of carbon-hydrogen bonds and removal of hydrogen (with a higher likelihood above ~5 eV), or otherwise leave the molecule in a chemically reactive state. Impact ionization plays a bigger role as the energy of the electrons increases beyond various ionization thresholds. Scission of various other bonds and fragmentation of the molecule are assumed to happen at higher energies. The fading of the diffraction pattern and the spectroscopic LEEM-IV features is proposed to be a result of polymerization of the layer and its transformation into a CNM, triggered by scission of molecular bonds and creation of radicals. Loss of definition in real-space images and increase in background intensity in diffraction images also indicate a more disordered surface landscape, likely as a result of polymerization of the layer. From electron energy loss measurements, secondary electrons generated during exposure were found to have energies mostly below ~4 eV and, as a result, have a negligible contribution to the damage cross-sections.

The implications of these results should be taken into account in experiments and processes that expose organic samples and materials to low-energy electrons, in the form of either a primary beam or as secondaries produced upon exposure of the sample to high energy electrons or photons. Note that such secondaries would possess energies within the range studied here. Given the lower damage rate at few-eV incident electron energies, experiments can be designed such that the sample is not destroyed or lasts longer during the experiment. The results can also point to the possible use of aromatic systems as electron resists with a significant energy threshold, to reduce the effects of low-energy secondary electrons in resist exposure. This may reduce the sensitivity of the resist, but also improve resolution and line edge roughness.

References

[1] L. Sanche, *Low Energy Electron-Driven Damage in Biomolecules*, Eur. Phys. J. D **35**, 367 (2005).

[2] B. Boudaïffa, P. Cloutier, D. Hunting, M. A. Huels, and L. Sanche, *Resonant Formation of DNA Strand Breaks by Low-Energy (3 to 20 eV) Electrons*, Science **287**, 1658 (2000).

[3] A. W. Robertson, C. S. Allen, Y. A. Wu, K. He, J. Olivier, J. Neethling, A. I. Kirkland, and J. H. Warner, *Spatial Control of Defect Creation in Graphene at the Nanoscale*, Nat. Commun. **3**, 1144 (2012).

[4] U. Kaiser et al., *Transmission Electron Microscopy at 20kV for Imaging and Spectroscopy*, Ultramicroscopy **111**, 1239 (2011).

[5] J. R. Fryer, C. H. McConnell, F. Zemlin, and D. L. Dorset, *Effect of Temperature on Radiation Damage to Aromatic Organic Molecules*, Ultramicroscopy **40**, 163 (1992).

[6] K. Murata and M. Wolf, *Cryo-Electron Microscopy for Structural Analysis of Dynamic Biological Macromolecules*, BBA - General Subjects **1862**, 324 (2018).

[7] L. A. Baker and J. L. Rubinstein, *Radiation Damage in Electron Cryomicroscopy*, in *Methods in Enzymology*; Jensen, G. J., Ed.; Academic Press (2010); Vol. 481, pp 371−388

[8] B. E. Bammes, J. Jakana, M. F. Schmid, and W. Chiu, *Radiation Damage Effects at Four Specimen Temperatures from 4 to 100 K*, J. Struct. Biol. **169**, 331 (2010).

[9] S. T. Skowron, S. L. Roberts, A. N. Khlobystov, and E. Besley, *The Effects of Encapsulation on Damage to Molecules by Electron Radiation*, Micron **120**, 96 (2019).

[10] J. R. Fryer, *Molecular Arrays and Molecular Structure in Organic Thin Films Observed by Electron Microscopy*, J. Phys. D: Appl. Phys. **26**, B137 (1993).

[11] A. Turchanin, D. Käfer, M. El-Desawy, C. Wöll, G. Witte, and A. Gölzhäuser, *Molecular Mechanisms of Electron-Induced Cross-Linking in Aromatic SAMs*, Langmuir **25**, 7342 (2009).

[12] A. Turchanin and A. Gölzhäuser, *Carbon Nanomembranes*, Advanced Materials **28**, 6075 (2016).

[13] A. Turchanin, *Synthesis of Molecular 2D Materials via Low-Energy Electron Induced Chemical Reactions*, Chimia **73**, 473 (2019).

[14] X. Zhang, C. Neumann, P. Angelova, A. Beyer, and A. Gölzhäuser, *Tailoring the Mechanics of Ultrathin Carbon Nanomembranes by Molecular Design*, Langmuir **30**, 8221 (2014).

[15] P. Angelova et al., *A Universal Scheme to Convert Aromatic Molecular Monolayers into Functional Carbon Nanomembranes*, ACS Nano **7**, 6489 (2013).

[16] S. J. Noever et al., *Transferable Organic Semiconductor Nanosheets for Application in Electronic Devices*, Adv. Mater. **29**, 1606283 (2017).

[17] J. Li and F. Banhart, *The Engineering of Hot Carbon Nanotubes with a Focused Electron Beam*, Nano Lett. **4**, 1143 (2004).

[18] T. W. Chamberlain et al., *Stop-Frame Filming and Discovery of Reactions at the Single-Molecule Level by Transmission Electron Microscopy*, ACS Nano **11**, 2509 (2017).

[19] D. Ugarte, *Curling and Closure of Graphitic Networks under Electron-Beam Irradiation*, Nature **359**, 707 (1992).

[20] F. Banhart and P. M. Ajayan, *Carbon Onions as Nanoscopic Pressure Cells for Diamond Formation*, Nature **382**, 433 (1996).

[21] I. Bespalov, Y. Zhang, J. Haitjema, R. M. Tromp, S. J. van der Molen, A. M. Brouwer, J. Jobst, and S. Castellanos, *Key Role of Very Low Energy Electrons in Tin-Based Molecular Resists for Extreme Ultraviolet Nanolithography*, ACS Appl. Mater. Interfaces **12**, 9881 (2020).

[22] A. Thete, D. Geelen, S. J. van der Molen, and R. M. Tromp, *Charge Catastrophe and Dielectric Breakdown during Exposure of Organic Thin Films to Low-Energy Electron Radiation*, Phys. Rev. Lett. **119**, 266803 (2017).

[23] J. Jobst, J. Kautz, D. Geelen, R. M. Tromp, and S. J. van der Molen, *Nanoscale Measurements of Unoccupied Band Dispersion in Few-Layer Graphene*, Nat. Commun. **6**, 8926 (2015).

[24] J. Jobst, A. J. H. van der Torren, E. E. Krasovskii, J. Balgley, C. R. Dean, R. M. Tromp, and S. J. van der Molen, *Quantifying Electronic Band Interactions in van der*

Waals Materials Using Angle-Resolved Reflected-Electron Spectroscopy, Nat. Commun. **7**, 13621 (2016).

[25] R. M. Tromp, Y. Fujikawa, J. B. Hannon, A. W. Ellis, A. Berghaus, and O. Schaff, *A Simple Energy Filter for Low Energy Electron Microscopy/Photoelectron Emission Microscopy Instruments*, J. Phys.: Condens. Matter. **21**, 314007 (2009).

[26] S. M. Schramm, J. Kautz, A. Berghaus, O. Schaff, R. M. Tromp, and S. J. van der Molen, *Low-Energy Electron Microscopy and Spectroscopy with ESCHER: Status and Prospects*, IBM J. Res. & Dev. **55**, 1:1 (2011).

[27] F. J. Meyer zu Heringdorf, M. C. Reuter, and R. M. Tromp, *Growth Dynamics of Pentacene Thin Films*, Nature **412**, 517 (2001).

[28] F. J. Meyer Zu Heringdorf, M. C. Reuter, and R. M. Tromp, *The Nucleation of Pentacene Thin Films*, Appl. Phys. A **78**, 787 (2004).

[29] A. Al-Mahboob, J. T. Sadowski, Y. Fujikawa, K. Nakajima, and T. Sakurai, *Kinetics-Driven Anisotropic Growth of Pentacene Thin Films*, Phys. Rev. B **77**, 035426 (2008).

[30] M. Misra and R. F. Egerton, *Assessment of Electron Irradiation Damage to Biomolecules by Electron Diffraction and Electron Energy-Loss Spectroscopy*, Ultramicroscopy **15**, 337 (1984).

[31] R. V. Khatymov, R. F. Tuktarov, and M. V. Muftakhov, *Lifetime of Negative Molecular Ions of Tetracene and Pentacene with Respect to the Autodetachment of an Electron*, JETP Lett. **93**, 437 (2011).

[32] M. V. Muftakhov, R. V. Khatymov, and R. F. Tuktarov, *Decomposition of Aromatic Compounds Relevant to Organic Electronics under Exposure to Low-Energy Electrons*, Tech. Phys. **63**, 1854 (2018).

[33] I. Kh. Aminev, V. I. Khvostenko, V. P. Yur’ev, and G. A. Tolstikov, *Mass Spectra of Negative Ions of Condensed Aromatic Hydrocarbons and Biphenyl*, Russ. Chem. Bull. **22**, 1831 (1973).

[34] S. Tobita, M. Meinke, E. Illenberger, L. G. Christophorou, H. Baumgärtel, and S. Leach, *Polycyclic Aromatic Hydrocarbons: Negative Ion Formation Following Low Energy (0-15 eV) Electron Impact*, Chem. Phys. **161**, 501 (1992).

[35] R. Azria and G. J. Schulz, *Vibrational and Triplet Excitation by Electron Impact in Benzene*, J. Chem. Phys. **62**, 573 (1975).

[36] P. Rowntree, P. C. Dugal, D. Hunting, and L. Sanche, *Electron Stimulated Desorption of H_2 from Chemisorbed Molecular Monolayers*, J. Phys. Chem. **100**, 4546 (1996).

[37] L. Amiaud, J. Houplin, M. Bourdier, V. Humblot, R. Azria, C. M. Pradier, and A. Lafosse, *Low-Energy Electron Induced Resonant Loss of Aromaticity: Consequences on Cross-Linking in Terphenylthiol SAMs*, Phys. Chem. Chem. Phys. **16**, 1050 (2014).

[38] J. Houplin, L. Amiaud, C. Dablemont, and A. Lafosse, *DOS and Electron Attachment Effects in the Electron-Induced Vibrational Excitation of Terphenylthiol SAMs*, Phys. Chem. Chem. Phys. **17**, 30721 (2015).

[39] J. Chen, D. C. Martin, and J. E. Anthony, *Morphology and Molecular Orientation of Thin-Film Bis(Triisopropylsilylethynyl) Pentacene*, J. Mater. Res. **22**, 1701 (2007).

[40] A. S. Eggeman, S. Illig, A. Troisi, H. Sirringhaus, and P. A. Midgley, *Measurement of Molecular Motion in Organic Semiconductors by Thermal Diffuse Electron Scattering*, Nat. Mater. **12**, 1045 (2013).

[41] L. E. Firment and G. A. Somorjai, *Surface Structures of Normal Paraffins and Cyclohexane Monolayers and Thin Crystals Grown on the (111) Crystal Face of Platinum. A Low-energy Electron Diffraction Study*, J. Chem. Phys. **66**, 2901 (1977).

[42] W. Han, H. Yoshida, N. Ueno, and S. Kera, *Electron Affinity of Pentacene Thin Film Studied by Radiation-Damage Free Inverse Photoemission Spectroscopy*, Appl. Phys. Lett. **103**, 123303 (2013).

[43] H. W. Jochims, H. Baumgärtel, and S. Leach, *Structure-Dependent Photostability of Polycyclic Aromatic Hydrocarbon Cations: Laboratory Studies and Astrophysical Implications*, ApJ **512**, 500 (1999).

[44] M. S. Deleuze, A. B. Trofimov, and L. S. Cederbaum, *Valence One-Electron and Shake-up Ionization Bands of Polycyclic Aromatic Hydrocarbons. I. Benzene, Naphthalene, Anthracene, Naphthacene, and Pentacene*, J. Chem. Phys. **115**, 5859 (2001).

[45] R. Boschi, J. N. Murrell, and W. Schmidt, *Photoelectron Spectra of Polycyclic Aromatic Hydrocarbons*, Faraday Discuss. Chem. Soc. **54**, 116 (1972).

[46] R. Boschi, E. Clart, and W. Schmidt, *Photoelectron Spectra of Polynuclear Aromatics. III. the Effect of Nonplanarity in Sterically Overcrowded Aromatic Hydrocarbons*, J. Chem. Phys. **60**, 4406 (1974).

[47] W. Schmidt, *Photoelectron Spectra of Polynuclear Aromatics. V. Correlations with Ultraviolet Absorption Spectra in the Catacondensed Series*, J. Chem. Phys. **66**, 828 (1977).

[48] W. Hwang, Y. K. Kim, and M. E. Rudd, *New Model for Electron-Impact Ionization Cross Sections of Molecules*, J. Chem. Phys. **104**, 2956 (1996).

[49] C. R. Arumainayagam, H. L. Lee, R. B. Nelson, D. R. Haines, and R. P. Gunawardane, *Low-Energy Electron-Induced Reactions in Condensed Matter,* Surf. Sci. Rep. **65**, 1 (2010).

[50] C. I. M. Beenakker and F. J. de Heer, *Dissociative Excitation of Benzene by Electron Impact*, Chem. Phys. Lett. **29**, 89 (1974).

[51] P. Mozejko, G. Kasperski, C. Szmytkowski, G. P. Karwasz, R. S. Brusa, and A. Zecca, *Absolute Total Cross Section Measurements for Electron Scattering on Benzene Molecules*, Chem. Phys. Lett. **257**, 309 (1996).

[52] H. Kato, M. C. Garcia, T. Asahina, M. Hoshino, C. Makochekanwa, H. Tanaka, F. Blanco, and G. García, *Absolute Elastic Differential Cross Sections for Electron Scattering by* $C_6H_5CH_3$ *and* $C_6H_5CF_3$ *at 1.5-200 eV: A Comparative Experimental and Theoretical Study with* C_6H_6, Phys. Rev. A **79**, 062703 (2009).

[53] H. Kato, M. Hoshino, H. Tanaka, P. Limo-Vieira, O. Inglfsson, L. Campbell, and M. J. Brunger, *A Study of Electron Scattering from Benzene: Excitation of the* $^1B_{1u}$, $^3E_{2g}$, *and* $^1E_{1u}$ *Electronic States*, J. Chem. Phys. **134**, 134308 (2011).

[54] C. Neumann, R. A. Wilhelm, M. Küllmer, and A. Turchanin, *Low-Energy Electron Irradiation Induced Synthesis of Molecular Nanosheets: Influence of the Electron Beam Energy,* Faraday Discuss. **227**, 61 (2021).

[55] W. Geyer, V. Stadler, W. Eck, M. Zharnikov, A. Gölzhäuser, and M. Grunze, *Electron-Induced Crosslinking of Aromatic Self-Assembled Monolayers: Negative Resists for Nanolithography*, Appl. Phys. Lett. **75**, 2401 (1999).

[56] S. Frey, H. T. Rong, K. Heister, Y. J. Yang, M. Buck, and M. Zharnikov, *Response of Biphenyl-Substituted Alkanethiol Self-Assembled Monolayers to Electron Irradiation: Damage Suppression and Odd-Even Effects*, Langmuir **18**, 3142 (2002).

[57] J. Houplin, C. Dablemont, L. Sala, A. Lafosse, and L. Amiaud, *Electron Processing at 50 eV of Terphenylthiol Self-Assembled Monolayers: Contributions of Primary and Secondary Electrons*, Langmuir **31**, 13528 (2015).

Supporting Information

Part A: Filtering procedure to remove the background from diffraction images

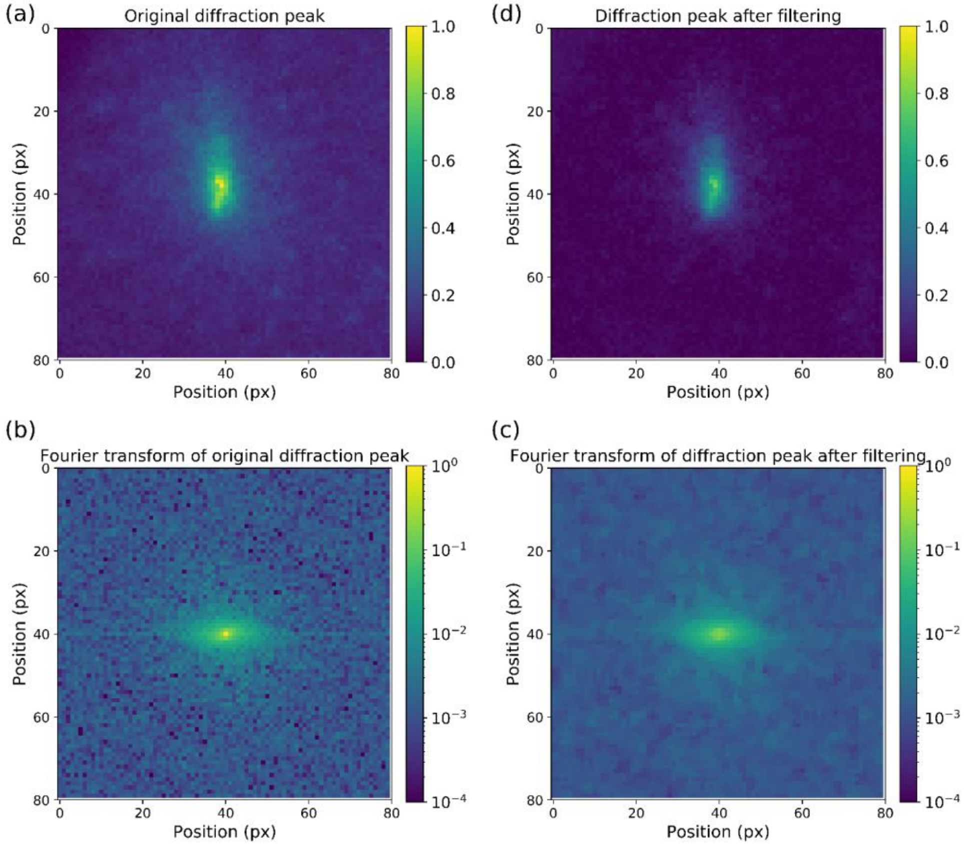

Fig. S4.1 A median filter is applied to the Fourier transform of each diffraction image to remove the low-frequency noise and background. (a) a measured diffraction peak, (b) Fourier transform of the diffraction peak, (c) median filter applied to (b), (d) inverse Fourier transform of (c). The original and filtered images are normalized to the same value, for both the top and the bottom pairs.

Part B: Damage cross-sections of more samples

Damage cross-sections of (0,0) diffraction peak measured with different beam currents on samples with pentacene film thicknesses of 2-4 monolayers.

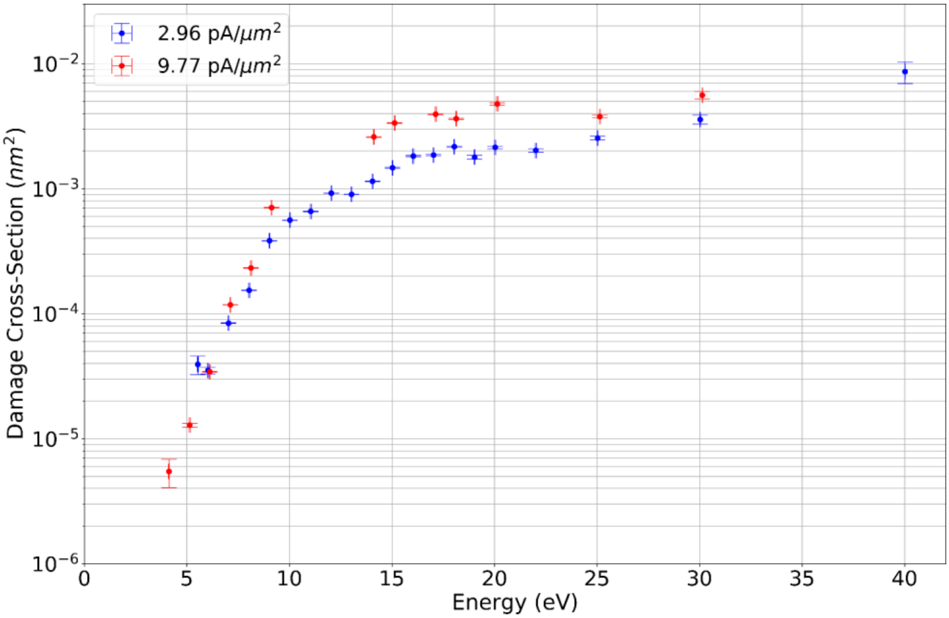

Fig. S4.2 Damage cross-sections of (0,0) diffraction peak versus incident electron energy, measured with two different electron beam currents on the same sample with film thickness of 4 monolayers.

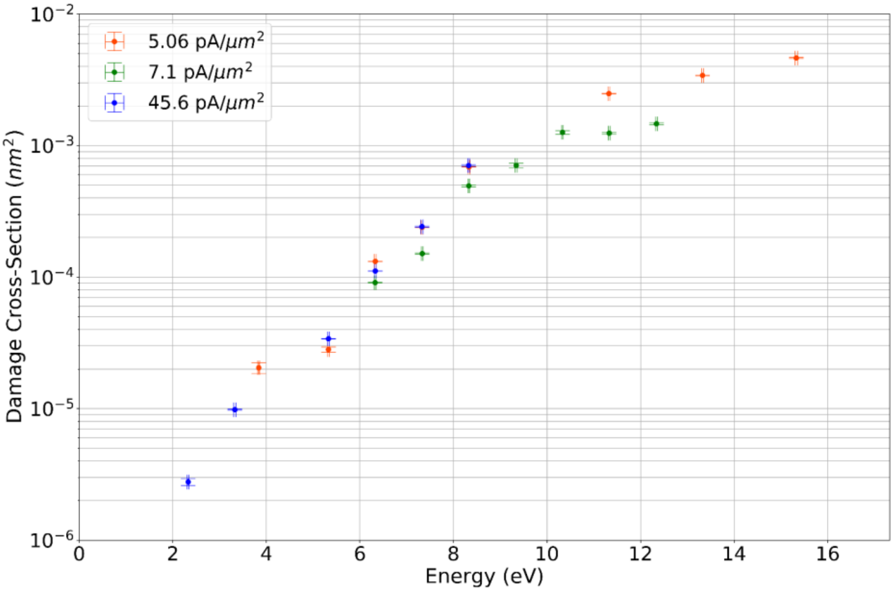

Fig. S4.3 Damage cross-sections of (0,0) diffraction peak versus incident electron energy measured with different electron beam currents. Datasets with beam current densities 45.6 pA/μm^2 and 5.06 pA/μm^2 belong to the same sample. The dataset with beam current density 7.1 pA/μm^2 belongs to a different sample. Both samples have a film thickness of 3 monolayers.

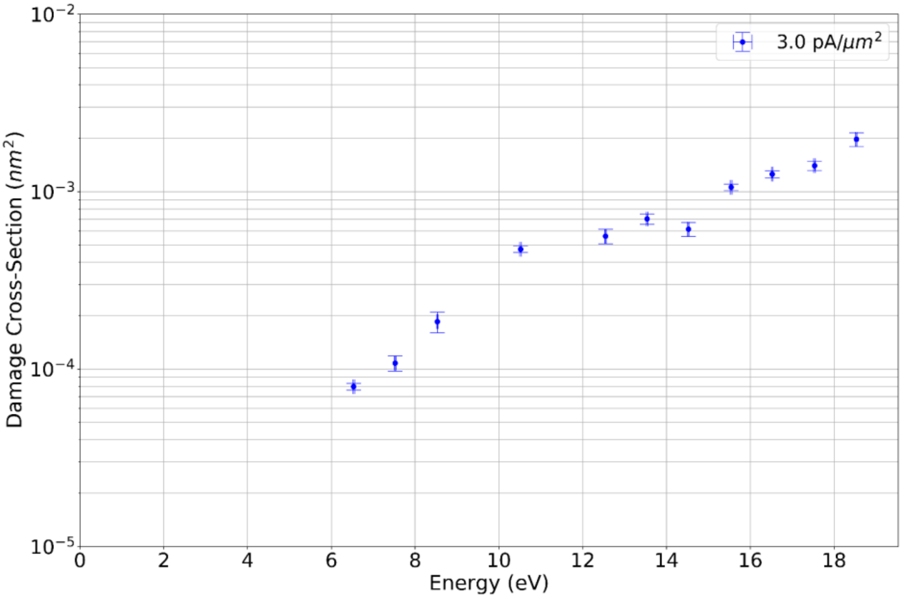

Fig. S4.4 Damage cross-sections of (0,0) diffraction peak versus incident electron energy measured on a sample with pentacene film thickness of 2 monolayers.

Part C: Evolution of widths of Lorentzian fits during irradiation

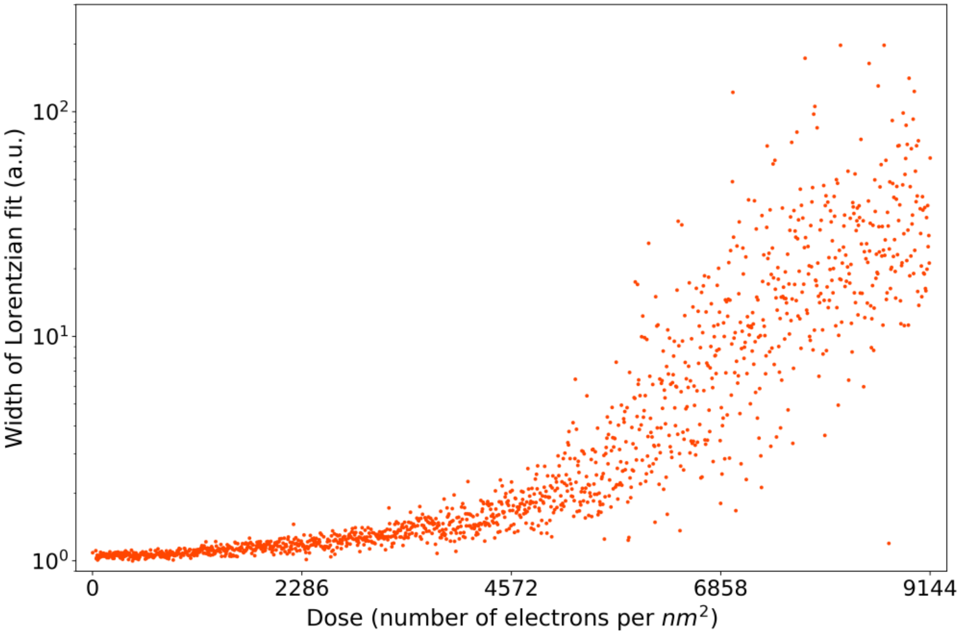

Fig. S4.5 Evolution of widths of Lorentzian fits to line profile of a (1,1) diffraction peak during irradiation with 10 eV electrons. The thickness of pentacene film is 4 monolayers and the beam current density is 2.96 pA/µm^2. This figure is obtained from the same recording as Fig. 4.2

Part D: Irradiation damage in real-space images

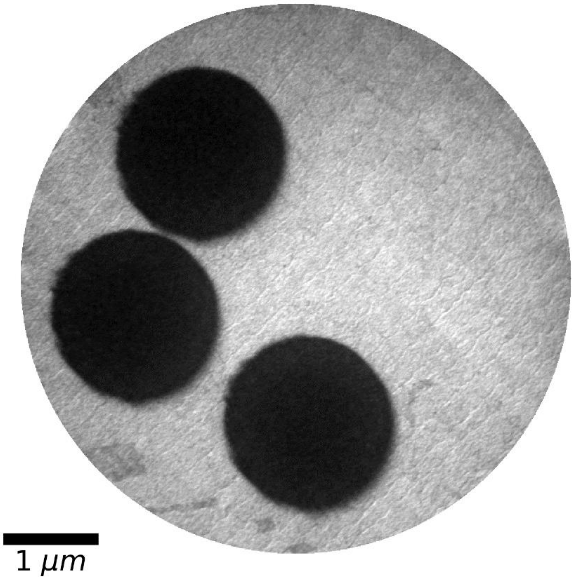

Fig. S4.6 Bright-field LEEM image of a sample with film thickness of 4 monolayers, obtained with electron energy 3.8 eV. The regions selected by an illumination aperture for damage recordings appear dark after irradiation with 16 eV, 14 eV and 12 eV electrons, respectively, from top to bottom.

Part E: Increase of background intensity in diffraction images due to irradiation

The figures below show the percentage of intensity change for all pixels across the entire diffraction image for the last few frames at the end of a period of exposure compared to the beginning. The images show an increase in the background intensity and a decrease in the intensity around the diffraction spots, indicating that more electrons are scattered incoherently.

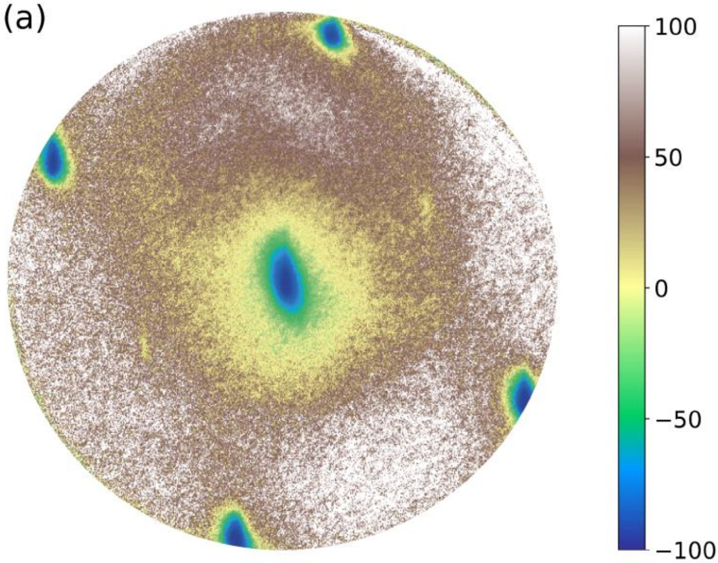

Fig. S4.7 (a) Percentage of change in intensity for all pixels across the diffraction image. The intensity of the last few frames at the end of a period of irradiation is compared with the first few frames. Intensity changes in regions with white color exceed 100%. Thickness of the pentacene film is 4 monolayers. Energy of incident electrons is 8 eV. The beam current density is 2.96 pA/μm^2

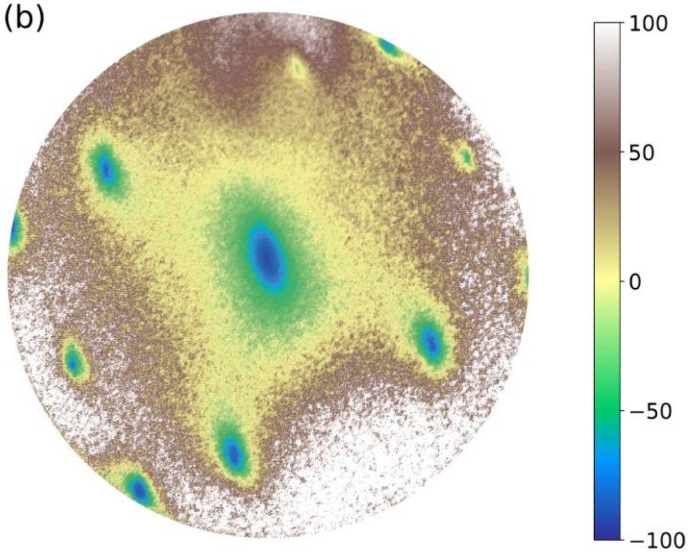

Fig. S4.7 (b) Percentage of change in intensity for all pixels across the diffraction image. The intensity of the last few frames at the end of a period of irradiation is compared with the first few frames. Intensity changes in regions with white color exceed 100%. Thickness of the pentacene film is 4 monolayers. Energy of incident electrons is 16 eV. The beam current density is 2.96 pA/μm^2

Part F: Changes in Electron Energy Loss Spectra due to irradiation

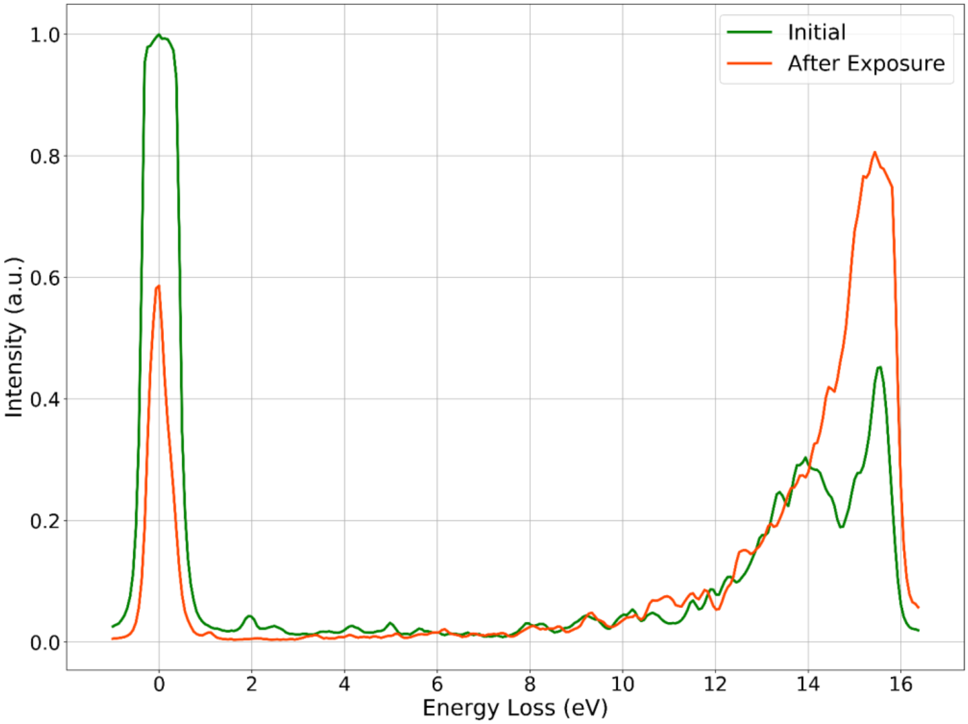

Fig. S4.8 Changes in the Electron Energy Loss Spectra of a sample with film thickness of 3 monolayers after a period of irradiation with electron energy 16.4 eV. The peak at 0 eV is the original beam, i.e. the (0,0) diffraction peak. The peak around 14 eV visible in the initial spectrum is due to excitation within the layer caused by the electrons. The peak at the end of the loss spectrum is associated with secondary electrons. This peak increases in intensity during irradiation.

Part G: Irradiation experiment on a HOPG flake

Similar irradiation experiments on a HOPG flake yield a negligible decay of intensity of diffraction peaks for the same electron doses. Fig. S4.9 shows a representative result for 7-eV electrons. Intensity fluctuations in Fig. S4.9 (especially for the HOPG sample) are attributed to electron beam fluctuations. This result rules out carbon deposition from the background pressure as being responsible for the decay of intensity of the diffraction spots of pentacene.

The HOPG flakes were exfoliated in ambient conditions on a silicon substrate, and subsequently transferred inside the microscope and heated (at UHV pressure of 1.0×10^{-9} mbar or better) at $500^{\circ C}$ for many hours to be cleaned.

Exposure measurements were carried out at room temperature, similar to measurements on pentacene samples.

Note again that both the growth of pentacene layers and the measurements on them are carried out in a UHV pressure of $\sim1.0\times10^{-9}$ mbar or lower to ensure a clean environment for our experiments.

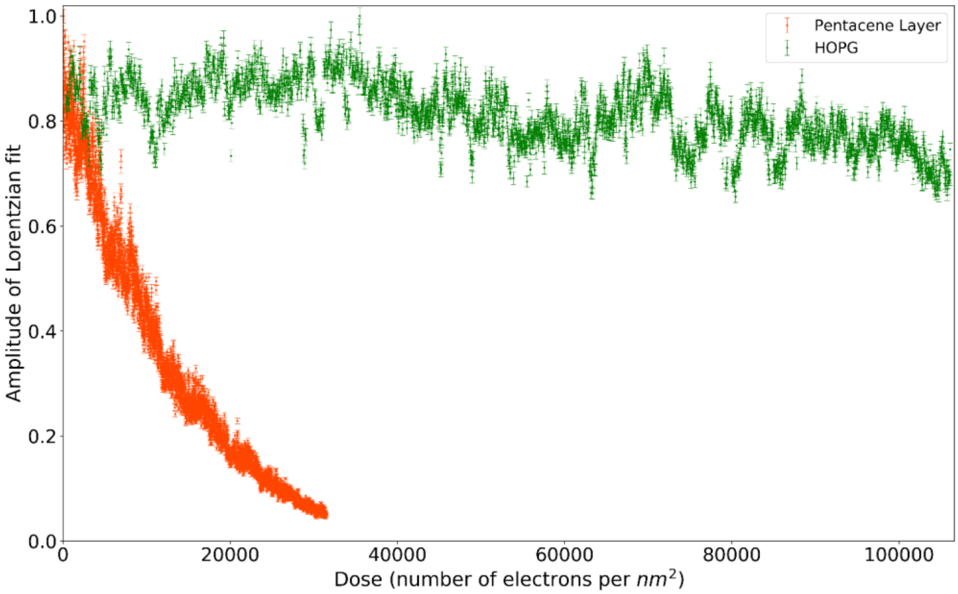

Fig. S4.9 Evolution of amplitudes of Lorentzian fits to 0th-order diffraction spot for an HOPG flake compared to a pentacene film upon irradiation with 7 eV electrons. The pentacene film is four-monolayers in thickness. The beam current density is 2.96 pA/μm^2 for the pentacene sample and 16.1 pA/μm^2 for the HOPG sample.

5

Critical Role of Electronic States above the Vacuum Level in Photo-Electron and Secondary-Electron Emission in Few-Monolayer Pentacene Films *

Abstract

Electron states above the vacuum level are known to play an important role in secondary electron processes, such as photo-electron emission and secondary electron emission, where they act as “final” (or better: “intermediate”) states from which an electron is emitted to the vacuum. However, despite their relevance, these states are typically not well-known, nor independently investigated, mostly due to a lack of proper spectroscopic techniques. Here, we present a spectroscopy study on crystalline pentacene, used as a model system to investigate the influence of these states on secondary electron processes. Using low-energy electron (LEE) spectroscopy, we first gauge the spectrum of such states in few-monolayer pentacene films. We subsequently relate these states to photo-electron and secondary electron emission. Specifically, photo-emission experiments (Hg lamp) show a decrease of intensity with each additional pentacene layer grown. Given an absence of increase in the ionization energy or change in the crystal structure with increasing layer count, we relate the decrease in photo-emission intensity to the emergence of a band gap just above the vacuum level, as observed in LEE reflectivity spectra. Second, we study the energy distribution of secondary electrons. We use electron beam damage to cause controlled changes in the band structure, and find a clear correlation between the evolution of the LEE spectra and the distribution of secondary electrons.

5.1 Introduction

Photoemission spectroscopy techniques are among the most prevalent tools to investigate the electronic band structure of solids. Depending on the energy of the photons, different electronic bands of the material are probed. Techniques such as X-ray photoelectron spectroscopy (XPS), extended X-ray absorption fine structure (EXAFS) or near edge X-ray absorption fine structure (NEXAFS) target the core shells while photoemission electron microscopy (PEEM) and angle-resolved photoelectron spectroscopy (ARPES) among others, probe the occupied (valence) bands. The depth probed is a function of the energy of the incident photons due to the mean free path of both the photons and the ejected photoelectrons [1], and is an important consideration in the correct interpretation of the material properties from photoemission spectroscopies. [2,3] Another important factor is the electron's initial excitation from an occupied state to an intermediate excited state above the vacuum energy, before it exits the material. Although short-lived, such states are known to play an important role in the photoemission process. Unfortunately, in most photoemission studies, there is no independent information on these intermediate states. Hence, the typical approach in the interpretation of photoemission data is to assume that the electrons are excited into a free-electron-like final state, ignoring the details of the unoccupied band structure. [4-7] Still, several authors have successfully incorporated unoccupied intermediate states (confusingly often referred to as "final states" in photoemission literature), usually from theoretical calculations and VLEED measurements, to explain photoemission data and resolve inconsistencies in band structure mapping. Some examples include $TiTe_2$ [4], single-crystal Ni(110) [5], SiC with a graphite overlayer [8], Cu [6,7], and monolayer and bilayer graphene. [9] Also, recently the lifetime of final states of photoelectrons has been experimentally measured in Ni(111), Ag(111) and Au(111), with values reaching ~100 attoseconds for some states. [10,11]

A related phenomenon is the emission of secondary electrons (SEs). SEs generated by exposure to high-energy electrons or photons are responsible for much of the damage caused in biological and organic materials [12,13], but they are also exploited in applications such as lithography to deliberately cause chemical changes in an organic resist material. Nonetheless, after decades of research, our understanding of the fundamental processes regarding the generation of SEs is limited. The energy and momentum of the primary beam

---

* This chapter has been published as "Critical role of electronic states above the vacuum level in photoelectron and secondary electron emission in few-monolayer pentacene films", A. Tebyani, R.M. Tromp, S.J. van der Molen - Phys. Rev. B 108, 045425 (2023)

electrons are transferred to the electrons in the sample via multiple scattering events, leading to a loss of information on the details of the interactions between the beam electrons and the sample electrons. The unoccupied band structure has been shown to also affect the emission of SEs [14], such as the case of graphene layers formed on SiC(0001), for which SEs show energy-dependent intensity distributions with six-fold symmetry and features ascribed to the band structure [15], or in other studies on graphite to explain the features in the SE emission spectra. [16-18]

Here, we use Low-Energy Electron Microscopy (LEEM) to study the interaction of crystalline pentacene films, one to four monolayers in thickness, with low-energy electrons (LEEs) as well as UV photons. Scattering of LEEs from the sample does not only provide real- and reciprocal- space information about the microstructure, but also yields direct information on unoccupied bands above the vacuum level and their dispersion. [19-20] Interestingly, these are exactly the states that can act as intermediates in photoemission and SE emission processes. Hence, their (un)availability directly affects the emission yield of photo-electrons and SEs.

Specifically, we connect LEEM-IV spectra (i.e. the intensity of specularly-reflected low energy electrons as a function of incident energy) to photoemission and SE spectra, performing a series of experiments within the same instrument. Our system of choice is pentacene, which can be grown and studied layer-by-layer in LEEM, in real-time. First, we focus on photoemission due to excitation by a standard Hg lamp ($h\nu = 4.9$ eV). For a series of well-defined layer thicknesses (0-4 monolayers), we correlate photoemission intensity with LEEM-IV spectra, which contain information about the unoccupied states just above the vacuum level. Additionally, we probe the yield and energy distribution of SEs from pentacene, for a series of electron beam energies. [21] Here, we deliberately use electron beam damage to create chemical, structural and electronic changes in the layers. [22] Doing this in a controlled manner allows us to correlate changes in LEEM spectra and SE energy distribution curves. Our experimental observations highlight the influence of the unoccupied states on secondary processes such as photoemission and SE emission.

5.2 Experimental Technique

A schematic of the LEEM instrument is shown in Fig. 5.1(a). A beam of 15 keV electrons is decelerated to a tuneable kinetic energy of just a few eV before interaction with the sample, due to a voltage bias of -15 kV from the objective lens to the sample. Reflected electrons are re-accelerated by the same electric field and guided to the detector after travelling through an aberration-correcting path including electron mirror optics, forming a real-space or diffraction image on the detector screen. [23,24] A high-pressure Hg UV lamp attached to the sample chamber provides the possibility for PEEM. All measurements are carried out in ultrahigh vacuum (UHV) and at room temperature.

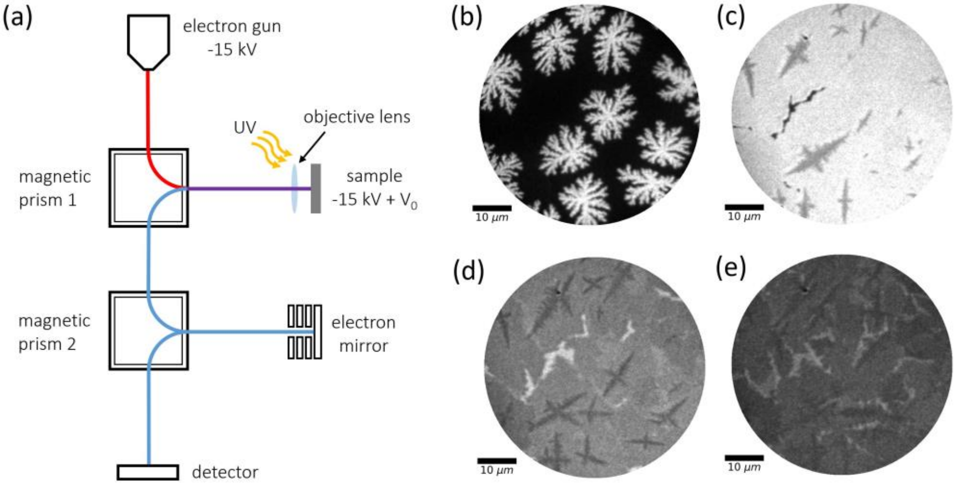

Fig. 5.1 (a) Schematic of LEEM instrument. The electron beam follows the path indicated by the red line towards the sample. The electric field between the sample and the objective lens decelerates the electrons to an energy of eV_0, tuned by setting the sample voltage. The blue line shows the trajectory of the reflected electrons toward the detector. The purple line shows where the path of the incident and the reflected beams overlap. The electron mirror corrects lower-order aberrations. Magnetic prisms separate incoming and outgoing beams and allow for electron energy spectra due to their dispersive character. In PEEM, the electron gun is turned off and the sample is irradiated with photons from a (Hg) light source. Photo-emitted electrons are subsequently imaged. (b-e) PEEM images of various stages of pentacene layer growth: (b) initial stage of nucleation and formation of the first pentacene layer in thin film phase (b) initial stage of nucleation of the second layer, which appears darker (d) initial stage of nucleation of the third layer (e) initial stage of nucleation of the fourth layer, which creates little contrast with the third layer.

5.3 Results and Discussion

The pentacene layers are grown *in situ* on silicon substrates using a Knudsen cell evaporator with line of sight to the sample. The growth dynamics of the layers is monitored in real-time both in LEEM and PEEM, as described in the literature. [25-27] At the start of sublimation, pentacene molecules are chemisorbed due to the dangling bonds on the atomically clean Si surface, leading to a decrease in photoemission intensity [27] (see Fig. S5.1 in Supporting Information Part A [28]). Afterwards, nucleation spots with higher photoemission intensity appear, which grow and merge as the sublimation continues (Fig. 5.1(b)). These nucleation spots thus evolve into the first pentacene layer in the standing-up thin-film phase. The diffraction pattern of this layer shows that it is in a herringbone crystal structure, consistent with the literature. [25] As growth continues, subsequent layers form on top of the first layer. From the diffraction patterns of these additional layers, we find the same crystal structure as for the first layer (see Fig. S5.2 in Supporting Information Part B [28]).

Hg PEEM images capturing various stages of growth are shown in Fig. 5.1(b-e). The weak photoemission signal from the substrate is due to the higher ionization energy (IE) of silicon compared to the energy of the incoming photons (the IE being the minimum amount of energy required to extract a photoelectron from the sample). [29] As is evident from Fig. 5.1(b-e), the photoemission intensity drops for each subsequent pentacene layer after the first, even though the crystalline structure of the layers remains the same. This suggests an increase in IE with increasing layer thickness.

In the literature, the addition of consecutive layers has been reported to increase the polarization energy of a molecular layer, thereby resulting in a reduction of the ionization energy. [30] Furthermore, although ionization energies reported for the thin film pentacene phase on SiO_2 range between 4.69 eV and 4.93 eV for 1-20 nm films, no consistent dependence of IE on film thickness has been observed. [31-36] In fact, a decrease in IE of pentacene films on SiO_2 with increasing thickness in the 1-20 nm range, accompanying broadening and splitting of the HOMO band, has been reported. [35] As the PEEM intensity changes observed in Fig. 5.1(b-e) cannot be explained by these reports, another explanation is due. This prompts us to investigate the role of unoccupied states. If the unoccupied states just above the vacuum level were to change as a function of pentacene layer thickness, the photoemission yield would also become a function of thickness. In LEEM, the energy of the incident electrons can be precisely tuned by changing the sample potential. Measuring the intensity of specularly reflected electrons as a function of the incident electron energy yields an intensity-vs-voltage plot, a LEEM-IV spectrum. Such LEEM-IV spectra are largely determined by the unoccupied band structure above the vacuum level. [4,7,19,20, 37-39] At electron energies corresponding to a bandgap (zero density of unoccupied states), incoming electrons cannot enter the sample, resulting in high reflectivity. At energies corresponding to an unoccupied state (or band) in the material, the reflectivity will be low. In the latter case, the reflectivity is determined by the coupling strength of the electron plane wave (coming from the vacuum) to the unoccupied sample state, i.e. by the Schrödinger equation. Since both key parameters (unoccupied DOS *and* coupling probabilities) also affect photoemission, LEEM spectra are particularly helpful in understanding the intricacies of photoemission. [9,40]

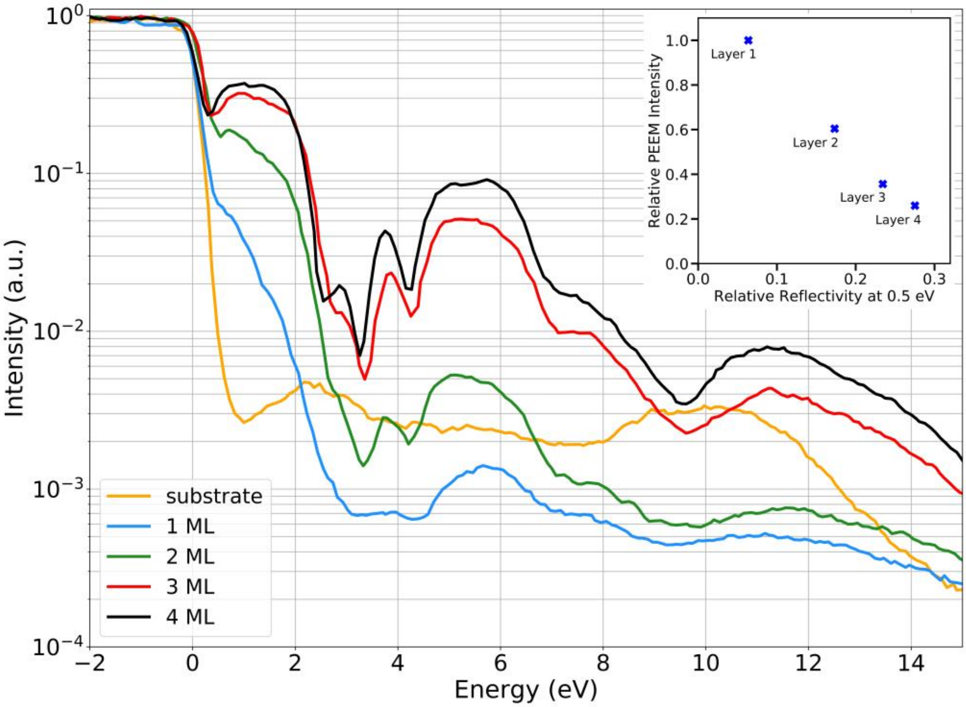

Fig. 5.2 (main) LEEM-IV spectra showing the evolution of reflectivity of a pentacene film across four layer counts. An energy of 0 eV corresponds to vacuum level. Negative energies indicate the electrons do not have enough kinetic energy to reach the sample, resulting in total reflection. The spectra for higher layer counts are more pronounced. Note the emergence of a bandgap 0-2 eV above the vacuum level as the number of layers increases. (inset) Relative PEEM intensity of various layer counts obtained from Fig. 5.1 vs. the reflectivity from LEEM-IV spectra at 0.5 eV.

In Fig. 5.2, we show LEEM-IV spectra for pentacene films of one to four monolayers in thickness, as well as for the Si substrate. Here, 0 eV corresponds to the vacuum level, and negative energies indicate insufficient kinetic energy for the incoming electrons to reach the sample (due to the negative sample bias), resulting in total reflection. The spectra in Fig. 5.2 are obtained from the same sample. The growth was paused after each subsequent layer, and several (2-6) LEEM-IV spectra were measured. Each of the spectra in Fig. 5.2 is the average of the spectra of the same layer count on the sample. The relative reflection intensity for different layer counts was consistent in all these measurements, i.e. higher layer counts resulted in higher reflection also in each of the individual measurements. The LEEM-IV spectra in Fig. 5.2, as well as the PEEM images in Fig. 5.1, were reproduced in several other samples.

The most noticeable observation in Fig. 5.2 is that the pentacene-related spectral features become more pronounced with increasing layer count. This is partly due to the better crystallinity of higher layers (as evidenced by sharper diffraction peaks) resulting in sharper spectra, and partly due to the diminishing effect of the substrate (which has generally lower reflectivity) on the measured reflectivity in thicker films, and also partly due to the developing pentacene band structure with increasing layer thickness.

The intensity in all five LEEM-IV spectra starts to drop at the same electron energy of ~0 eV, indicating an absence of any change in work function (i.e. the distance between Fermi energy and vacuum level) between films of different thicknesses. This indeed confirms previous articles reporting the work function of pentacene films on SiO_2 and ITO to exhibit almost no change for film thicknesses from 1 nm to 20 nm. [35,41] The main feature in Fig. 5.2, however, is a marked increase in reflectivity between 0 eV and 2 eV, as the film gets thicker. That is, a bandgap appears to develop in this energy range. Moreover, given the Hg photon energy and the IEs reported for the pentacene film in the literature, the photoelectrons are expected to have “final-state” energies located within this developing bandgap. Hence, for thicker films, electrons are less likely to be photo-excited, decreasing the probability of photoemission. We note that the LEEM-IV’s show a smaller degree of change in reflectivity for each consecutive layer in the 0-2 eV region; i.e. whereas the difference in reflectivity between the one-monolayer and two-monolayer films is considerable, the relative difference between three-monolayer and four-monolayer films is much smaller. This observation is compatible with the slowing changes in PEEM intensities for thicker layers, see Fig. 5.1(b-e). To highlight their relation, the inset of Fig. 5.2 plots PEEM intensity vs. electron reflectivity at 0.5 eV for the different layer counts. We find a clear, negatively sloped relation. From the above, and the previous discussion on IE, we conclude that the changes observed in photoemission are directly related to changes in the unoccupied DOS just above the vacuum energy, not to changes in IE.

Next, we focus on the role of unoccupied states in secondary electron emission (resulting from impinging primary electrons). Influence of the unoccupied electronic states on the ejection of both low-energy photoelectrons and SEs can be found in the literature in the form of observed similarities between photoelectron and SE spectra. [42,43] A study of silver islands on Si(111) found Ag(111) islands to appear brighter in PEEM and also exhibit higher SE emission compared to Ag(001) islands, an observation attributed to the differences in the DOS above the vacuum level between the two. [44,45] Here, we measure and analyze LEEM-IV spectra in conjunction with SE energy spectra to provide further insight into the emission of SEs. SE energy spectra can be obtained *in situ* in LEEM, taking advantage of the energy dispersion of the magnetic prism arrays (Fig. 5.1(a)). [21]

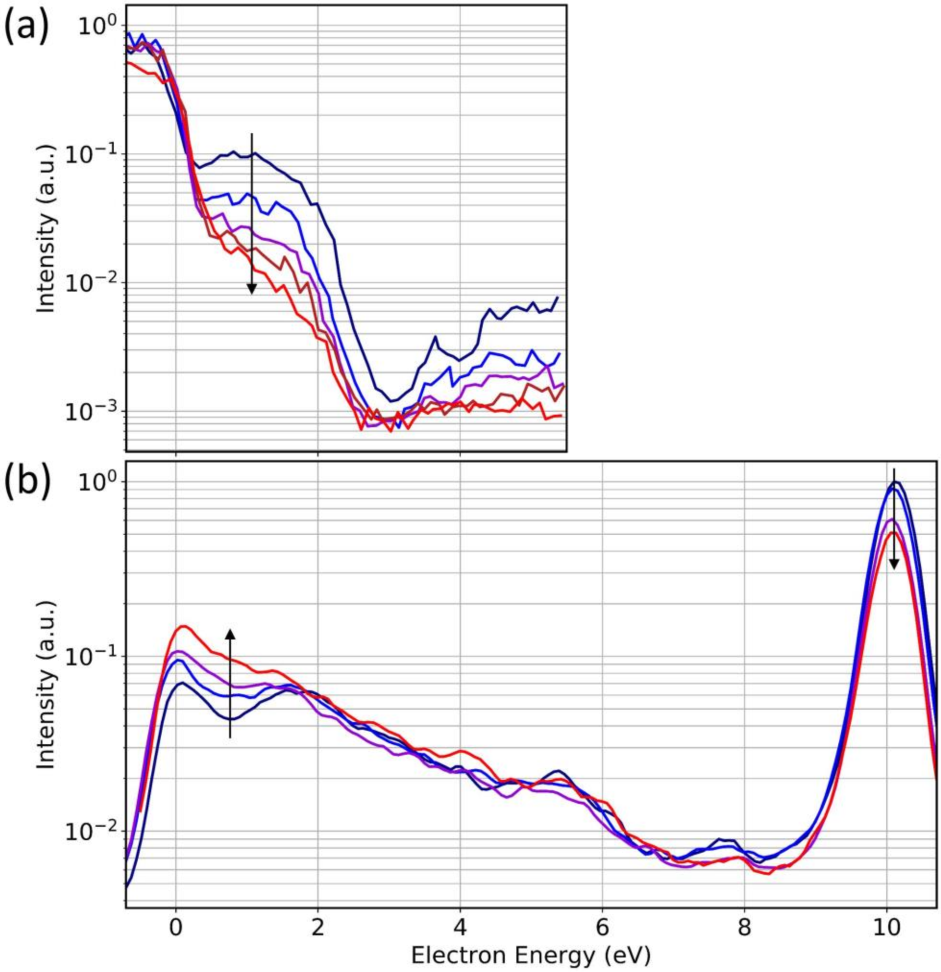

Fig. 5.3 Concomitant evolution of LEEM-IV spectra (a) and electron energy spectra (b) as a result of continued exposure to the electron beam (dark blue towards red). The pentacene film is three monolayers in thickness. (a) Changes in LEEM-IV spectra show the disappearance of the bandgap located at 0-2 eV above the vacuum energy (0 eV). (b) The dip in secondary electron distribution gradually disappears as a result of exposure to 10.1 eV electrons. (b) is measured on the same area as (a) and in between LEEM-IV measurements. The black arrows in (a) and (b) point in the direction of increased exposure to the beam. The beam current density during measurements of spectra as well as during exposure to 10.1 eV electrons was 6.72 pA/μm^2. Also, an aperture with an area of 1.15 μm^2 was placed along the beam's path in order to limit the measurements to a homogeneous area.

In a previous study [22], we reported a gradual diminishing of LEEM-IV features as a result of continued exposure of pentacene layers to an electron beam, attributed to beam damage and loss of crystalline order in the layers. Here, we use this change as an independent tool to correlate SE emission and unoccupied states. In Fig. 5.3 (a) we show the evolution of LEEM-IV spectra as a 3-monolayer pentacene film is exposed to a beam of 10.1 eV electrons. Clear changes are observed, most notably the disappearance of the bandgap-related structure around 1 eV as damage progresses. The increased level of noise in LEEM-IV spectra in Fig. 5.3(a) compared to Fig. 5.2 is due to placement of a small aperture along the beam's path, lower beam current as well as to the spectra not being averaged. In Fig. 5.3 (b), we show a set of electron energy spectra that were measured alternatingly with the LEEM-IV spectra, on the same area. The strong peak at 10.1 eV corresponds to the intensity of the reflected primary electron beam, whereas the low-energy distribution (0-5 eV) corresponds to SEs (see also Supporting Information Part C [28]). Note the clear dip in the spectrum around 1 eV. As beam damage proceeds, the electron energy spectra exhibit both a reduction in the intensity of the elastic peak at 10.1 eV and an increase in SE emission around 1 eV (figure colors: dark blue toward red). Specifically, the dip between 0 and 2 eV disappears in the later spectra (see Fig. S5.3 in Supporting Information Part C [28] for more examples). This change in SE spectra thus happens concomitant with the diminishing of the bandgap between 0 eV and 2 eV in Fig. 5.3 (a) due to beam damage. These observations were reproduced in several other samples as well. We note that the measurements of the LEEM-IV spectra themselves (taken in-between measurements of the electron energy spectra) are expected to cause only minimal damage. This is due to the negligible damage cross-section of pentacene films for electrons of energies up to ~5.5 eV [22], i.e. the energy up to which the LEEM-IV spectra in Fig. 5.3(a) were obtained. Hence, the changes in Fig. 5.3(b) are only caused by exposure to electrons of fixed energy (10.1 eV). The exposure period varied between ~1 minute for the exposure between the first two electron energy spectra, and ~10 minutes between the last two spectra, indicating a faster rate of change in the electronic properties of the sample at the beginning, i.e. when the sample is pristine.

Our interpretation is that the states above the vacuum level play a key role in the SE spectra observed. Specifically, the bandgap at energies 0-2 eV above the vacuum energy suppresses the ejection of SEs with those energies, due to a lower density of available (intermediate) states. This results in the appearance of a dip in the energy distribution of SEs for pristine pentacene layers. The disappearance of a well-defined bandgap - as a result of chemical and electronic changes in the sample due to beam exposure - results in a higher density of available states for the SEs, hence creating a pathway for emission of SEs. This is similar to the case of photoemission discussed above. Note that previous UPS measurements on pentacene films on SiO_2 and ITO, with the same herringbone-like structure, have also reported a dip in the energy distribution of SEs. Interestingly, such a pattern was not observed in pentacene films on HOPG, where the molecules adopt a recumbent orientation. [35,41]

This marked difference led to the attribution of the SE pattern to film structure-dependent unoccupied DOS, similarly to what is discussed here.

5.4 Conclusions

Summarizing, we have highlighted the importance of the unoccupied band structure in the interpretation of data from photoemission spectroscopies and secondary electron measurements. For this, we have combined and compared direct measurements of LEEM-IV spectra above the vacuum level in thin pentacene layers, performed by LEEM, with photoemission and secondary electron energy distribution measurements. We find that knowledge of the DOS above the vacuum energy is essential for a detailed analysis of photoemission measurements. Our data also indicate that the energy distribution and yield of secondary electrons are modulated by unoccupied states above the vacuum level. Hence, this material property should also be taken into account to understand and model generation and ejection of secondary electrons. In conclusion, we have demonstrated that LEEM-IV spectra, which provide direct information on the unoccupied states, form an essential piece of information in the analysis of both photoemission and secondary electron emission processes.

References

[1] M. P. Seah and W. A. Dench, *Quantitative Electron Spectroscopy of Surfaces: A Standard Data Base for Electron Inelastic Mean Free Paths in Solids*, Surf. Interface Anal. **1**, 2 (1979).

[2] T. Wagner, G. Antczak, M. Györök, A. Sabik, A. Volokitina, F. Gołek, and P. Zeppenfeld, *Attenuation of Photoelectron Emission by a Single Organic Layer*, ACS Appl. Mater. Inter. **14**, 23983 (2022).

[3] T. Wagner, G. Antczak, E. Ghanbari, A. Navarro-Quezada, M. Györök, A. Volokitina, F. Marschner, and P. Zeppenfeld, *Standard Deviation of Microscopy Images Used as Indicator for Growth Stages*, Ultramicroscopy **233**, 113427 (2022).

[4] V. N. Strocov, E. E. Krasovskii, W. Schattke, N. Barrett, H. Berger, D. Schrupp, and R. Claessen, *Three-Dimensional Band Structure of Layered $TiTe_2$: Photoemission Final-State Effects*, Phys. Rev. B **74**, 195125 (2006).

[5] X. Y. Cui, E. E. Krasovskii, V. N. Strocov, A. Hofmann, J. Schäfer, R. Claessen, and L. Patthey, *Final-State Effects in High-Resolution Angle-Resolved Photoemission from Ni(110)*, Phys. Rev. B **81**, 245118 (2010).

[6] V. N. Strocov et al., *Absolute Band Mapping by Combined Angle-Dependent Very-Low-Energy Electron Diffraction and Photoemission: Application to Cu*, Phys. Rev. Lett. **81**, 4943 (1998).

[7] V. N. Strocov, H. I. Starnberg, and P. O. Nilsson, *Mapping the Excited-State Bands above The vacuum Level with VLEED: Principles, Results For Cu, and the Connection to Photoemission*, J. Phys.: Condens. Matter **8**, 7539 (1996).

[8] N. Barrett, E. E. Krasovskii, J. M. Themlin, and V. N. Strocov, *Elastic Scattering Effects in the Electron Mean Free Path in a Graphite Overlayer Studied by Photoelectron Spectroscopy and LEED*, Phys. Rev. B **71**, 035427 (2005).

[9] E. Krasovskii, *One-Step Theory View on Photoelectron Diffraction: Application to Graphene*, Nanomaterials **12**, 4040 (2022).

[10] Z. Tao, C. Chen, T. Szilvási, M. Keller, M. Mavrikakis, H. Kapteyn, and M. Murnane, *Direct Time-Domain Observation of Attosecond Final-State Lifetimes in Photoemission from Solids*, Science **353**, 62 (2016).

[11] R. Locher, L. Castiglioni, M. Lucchini, M. Greif, L. Gallmann, J. Osterwalder, M. Hengsberger, and U. Keller, *Energy-Dependent Photoemission Delays from Noble Metal Surfaces by Attosecond Interferometry*, Optica **2**, 2334 (2015).

[12] L. Sanche, *Low Energy Electron-Driven Damage in Biomolecules*, Eur. Phys. J. D **35**, 367 (2005).

[13] B. Boudaïffa, P. Cloutier, D. Hunting, M. A. Huels, and L. Sanche, *Resonant Formation of DNA Breaks by Low-Energy (3 to 20 eV) Electrons*, Science **287**, 1658 (2000).

[14] A. Bellissimo, G. M. Pierantozzi, A. Ruocco, G. Stefani, O. Y. Ridzel, V. Astašauskas, W. S. M. Werner, and M. Taborelli, *Secondary Electron Generation Mechanisms in Carbon Allotropes at Low Impact Electron Energies*, J. Electron Spectrosc. **241**, 146883 (2020).

[15] H. Hibino, H. Kageshima, F. Z. Guo, F. Maeda, M. Kotsugi, and Y. Watanabe, *Two-Dimensional Emission Patterns of Secondary Electrons from Graphene Layers Formed on SiC(0 0 0 1)*, Appl. Surf. Sci. **254**, 7596 (2008).

[16] F. Maeda, T. Takahashi, H. Ohsawa, S. Suzuki, H. Suematsu, *Unoccupied-Electronic-Band Structure of Graphite Studied by Angle-Resolved Secondary-Electron Emission and Inverse Photoemission*, Phys. Rev. B **37**, 4482 (1988).

[17] K. Ueno, T. Kumihashi, K. Saiki, and A. Koma, *Characteristic Secondary Electron Emission from Graphite and Glassy Carbon Surfaces*, Jpn. J. Appl. Phys. **27**, L759 (1988).

[18] W. S. M. Werner, V. Astašauskas, P. Ziegler, A. Bellissimo, G. Stefani, L. Linhart, and F. Libisch, *Secondary Electron Emission by Plasmon-Induced Symmetry Breaking in Highly Oriented Pyrolytic Graphite*, Phys. Rev. Lett. **125**, 196603 (2020).

[19] J. Jobst, A. J. H. van der Torren, E. E. Krasovskii, J. Balgley, C. R. Dean, R. M. Tromp, and S. J. van der Molen, *Quantifying Electronic Band Interactions in van der Waals Materials Using Angle-Resolved Reflected-Electron Spectroscopy*, Nat. Commun. **7**, 13621 (2016).

[20] J. Jobst, J. Kautz, D. Geelen, R. M. Tromp, and S. J. van der Molen, *Nanoscale Measurements of Unoccupied Band Dispersion in Few-Layer Graphene*, Nat. Commun. **6**, 8926 (2015).

[21] R. M. Tromp, Y. Fujikawa, J. B. Hannon, A. W. Ellis, A. Berghaus, and O. Schaff, *A Simple Energy Filter for Low Energy Electron Microscopy/Photoelectron Emission Microscopy Instruments*, J. Phys. - Condens. Mat. **21**, 314007 (2009).

[22] A. Tebyani, F. B. Baalbergen, R. M. Tromp, and S. J. van der Molen, *Low-Energy Electron Irradiation Damage in Few-Monolayer Pentacene Films*, J. Phys. Chem. C **125**, 26150 (2021).

[23] S. M. Schramm, J. Kautz, A. Berghaus, O. Schaff, R. M. Tromp, and S. J. van der Molen, *Low-Energy Electron Microscopy and Spectroscopy with ESCHER: Status and Prospects*, IBM J. Res. Dev. **55**, 1:1 (2011).

[24] R. M. Tromp, J. B. Hannon, A. W. Ellis, W. Wan, A. Berghaus, and O. Schaff, *A New Aberration-Corrected, Energy-Filtered LEEM/PEEM Instrument. I. Principles and Design*, Ultramicroscopy **110**, 852 (2010).

[25] A. Al-Mahboob, J. T. Sadowski, Y. Fujikawa, K. Nakajima, and T. Sakurai, *Kinetics-Driven Anisotropic Growth of Pentacene Thin Films*, Phys. Rev. B **77**, 035426 (2008).

[26] F. J. Meyer zu Heringdorf, M. C. Reuter, and R. M. Tromp, *The Nucleation of Pentacene Thin Films*, Appl. Phys. A **78**, 787 (2004).

[27] Frank-J. Meyer zu Heringdorf, M. C. Reuter, and R. M. Tromp, *Growth Dynamics of Pentacene Thin Films*, Nature **412**, 517 (2001).

[28] See Supporting Information for PEEM during initial stage of sublimation, diffraction pattern of pentacene thin film phase and secondary electron Energy Spectra.

[29] C. Sgiarovello, N. Binggeli, and A. Baldereschi, *Influence of Surface Morphology on the Si(100) and (111) Ionization Potentials*, Phys. Rev. B **64**, 195305 (2001).

[30] S. M. Ryno, C. Risko, and J. L. Brédas, *Impact of Molecular Orientation and Packing Density on Electronic Polarization in the Bulk and at Surfaces of Organic Semiconductors*, ACS Appl. Mater. Inter. **8**, 14053 (2016).

[31] F. Bussolotti, S. Kera, K. Kudo, A. Kahn, and N. Ueno, *Gap States in Pentacene Thin Film Induced by Inert Gas Exposure*, Phys. Rev. Lett. **110**, 267602 (2013).

[32] I. Salzmann et al., *Intermolecular Hybridization Governs Molecular Electrical Doping*, Phys. Rev. Lett. **108**, 035502 (2012).

[33] Y. M. Lee, J. W. Kim, H. Min, T. G. Lee, and Y. Park, *Growth Morphology and Energy Level Alignment of Pentacene Films on* SiO_2 *Surface Treated with Self-Assembled Monolayer*, Curr. Appl. Phys. **11**, 1168 (2011).

[34] S. Duhm, I. Salzmann, G. Heimel, M. Oehzelt, A. Haase, R. L. Johnson, J. P. Rabe, and N. Koch, *Controlling Energy Level Offsets in Organic/Organic Heterostructures Using Intramolecular Polar Bonds*, Appl. Phys. Lett. **94**, 033304 (2009).

[35] H. Fukagawa, H. Yamane, T. Kataoka, S. Kera, M. Nakamura, K. Kudo, and N. Ueno, *Origin of the Highest Occupied Band Position in Pentacene Films from Ultraviolet Photoelectron Spectroscopy: Hole Stabilization versus Band Dispersion*, Phys. Rev. B **73**, 245310 (2006).

[36] H. Fukagawa, S. Kera, T. Kataoka, S. Hosoumi, Y. Watanabe, K. Kudo, and N. Ueno, *The Role of the Ionization Potential in Vacuum-Level Alignment at Organic Semiconductor Interfaces*, Adv. Mater. **19**, 665 (2007).

[37] E. Bauer, *Surface Microscopy with Low Energy Electrons* (Springer New York, NY, 2014)

[38] J. B. Pendry, *The Application of Pseudopotentials to Low-Energy Electron Diffraction II: Calculation of the Reflected Intensities*, J. Phys. C: Solid State Phys. **2**, 2273 (1969).

[39] J. B. Pendry, *Theory of Photoemission*, Surf. Sci. **57**, 679 (1976).

[40] J. I. Flege and E. E. Krasovskii, *Intensity-Voltage Low-Energy Electron Microscopy for Functional Materials Characterization*, Phys. Status Solidi **8**, 463 (2014).

[41] W. Han, H. Yoshida, N. Ueno, and S. Kera, *Electron Affinity of Pentacene Thin Film Studied by Radiation-Damage Free Inverse Photoemission Spectroscopy*, Appl. Phys. Lett. **103**, 123303 (2013).

[42] N. Ueno, S. Kiyono, and T. Watanabe, *Electron Scattering from Pentacene and Coronene Polycrystals*, Chem. Phys. Lett. **46**, 89 (1977).

[43] K. Seki, T. Hirooka, Y. Kamura, and H. Inokuchi, *Photoemission from Polycyclic Aromatic Crystals in the Vacuum-Ultraviolet Region. V. Photoelectron Spectroscopy by the Rare Gas Resonance Lines and Vacuum-Ultraviolet Absorption Spectra*, B. Chem. Soc. Jpn. **49**, 904 (1976).

[44] Y. Fujikawa, T. Sakurai, and R. M. Tromp, *Surface Plasmon Microscopy Using an Energy-Filtered Low Energy Electron Microscope*, Phys. Rev. Lett. **100**, 126803 (2008).

[45] Y. Fujikawa, T. Sakurai, and R. M. Tromp, *Micrometer-Scale Band Mapping of Single Silver Islands in Real and Reciprocal Space*, Phys. Rev. B **79**, 121401(R) (2009).

Supporting Information

Part A: PEEM during initial stage of sublimation

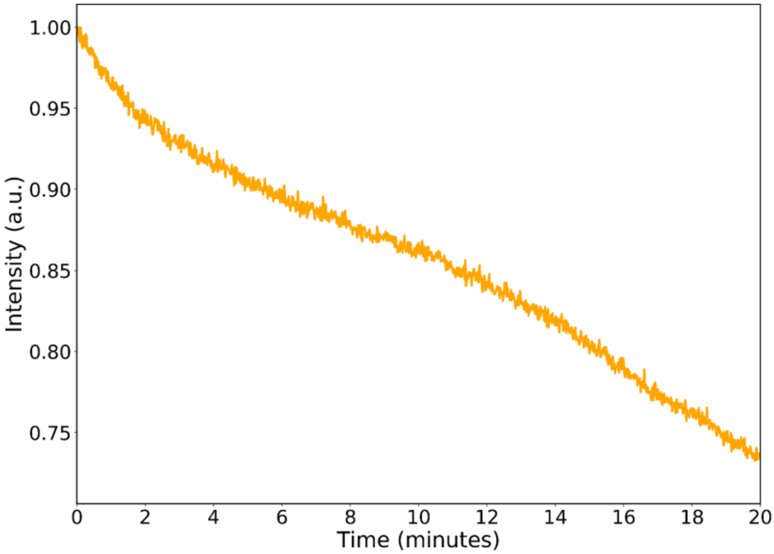

Fig. S5.1 Change in PEEM intensity during the initial stage of sublimation of pentacene on silicon (chemisorption stage), before nucleation spots of the standing-up thin-film phase appear

Part B: Diffraction pattern of pentacene thin film phase

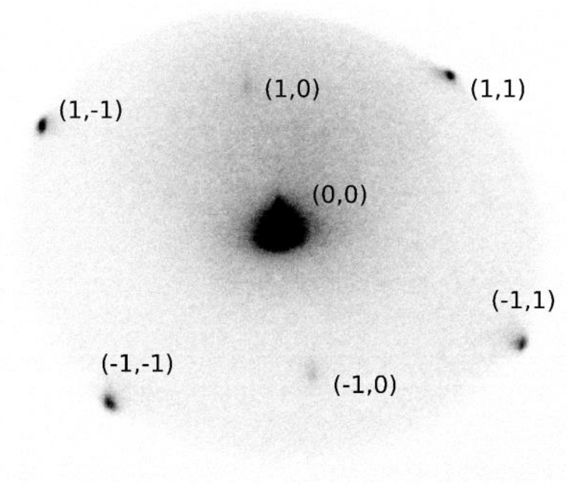

Fig. S5.2 Diffraction pattern corresponding to the standing-up thin-film pentacene phase with herringbone crystal structure, obtained from a film with four monolayers in thickness

Part C: Secondary Electron Energy Spectra

Fig. S5.3 shows energy spectra obtained for a pentacene film, four monolayers in thickness, for a series of incident electron beam energies. There are two curves for each incident beam energy. The first corresponds to the pristine area (black curves), while the second curve (orange) refers to the same area after a period of exposure to the beam, causing intentional beam damage. The strong peak at the right in all the spectra corresponds to the intensity of the elastically reflected electron beam. The distribution at the left corresponds to secondary electrons (SEs), which have kinetic energies of mostly 0-5 eV. Any peaks in between these ranges are due to inelastic scattering causing excitations in the sample, and as a result occur at specific material-dependent energies with respect to the primary beam, although their intensities are in general a function of the primary beam energy. For pentacene layers, the first five energy loss peaks are reported to occur at 2.15 eV, 4.29 eV, 5.68 eV, 6.81 eV and 8.16 eV lower energies compared to the primary beam. [1] The first two of these peaks are indicated in Fig. S5.3 by blue and green lines, respectively. As expected for peaks caused by specific, identifiable excitations in the pentacene layer, these peaks track with the peak associated with the elastically reflected electrons. The two spectra in each subfigure of Fig. S5.3 are normalized to the same value (maximum of the black curve).

Examining the energy distribution of the SEs of pristine areas, i.e. the black curves in Fig. S5.3, we notice the same pattern in all of them: a clear dip in intensity is seen between 0 and 2 eV, independent of the incident electron beam energy (black lines). After prolonged electron beam exposure, this dip is seen to disappear (orange lines), similar to what is seen in Fig. 5.3(b).

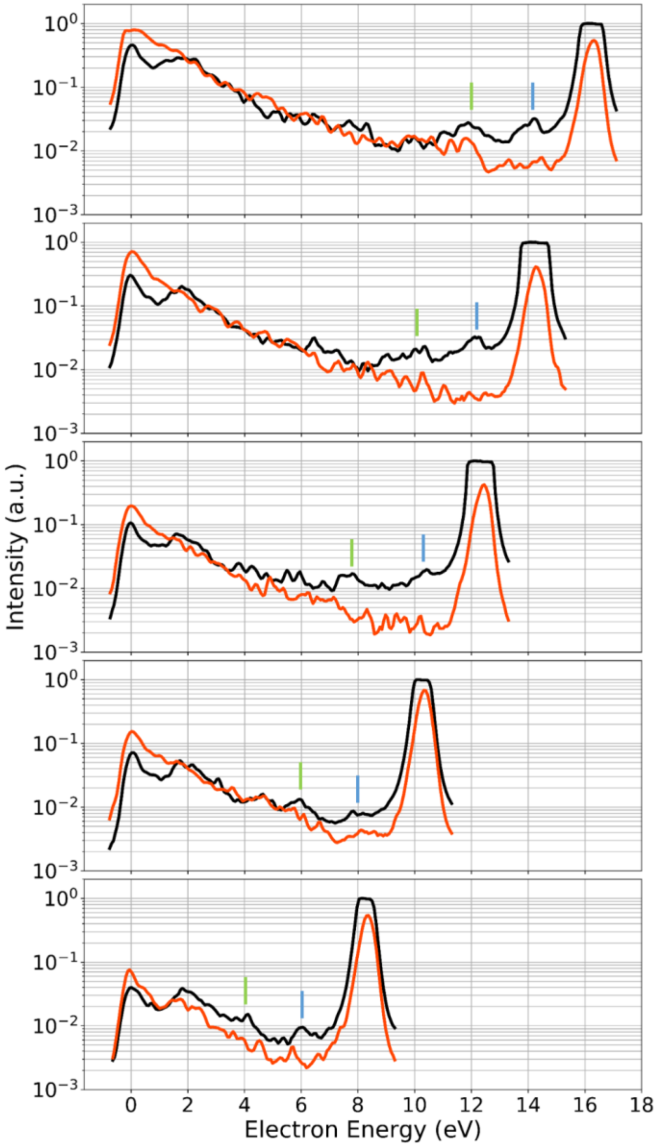

Fig. S5.3 Electron Energy Spectra of a four-monolayer pentacene film before (black) and after (orange) electron-beam irradiation, obtained for various incident energies of the electron beam. In each curve, the strong peak at the right corresponds to the primary beam intensity, which has an energy of 16.3 eV, 14.3 eV, 12.3 eV, 10.3 eV and 8.3 eV for the subfigures from the top toward the bottom, respectively. The distribution at low energies corresponds to the secondary electrons. Any peaks in between are a result of inelastic scattering causing crystal excitations. Two of such excitations are indicated in each plot by blue and green lines. The secondary electron energy distribution of all the spectra before irradiation (black) show a pattern of two peaks at 0 eV (vacuum level) and ~2 eV, separated by a dip. The same pattern is observed irrespective of the incident beam energy indicating that the peaks are not caused by inelastic scattering causing crystal excitations. This dip is virtually gone after irradiation (orange curves). See also Fig. 5.3(b).

References

[1] N. Ueno, S. Kiyono, and T. Watanabe, *Electron Scattering from Pentacene and Coronene Polycrystals*, Chem. Phys. Lett. **46**, 89 (1977).

6

Band Structure of Few-Monolayer Pentacene Films Above the Vacuum Level

Abstract

In the previous chapter, we examined the evolution of unoccupied electronic states above the vacuum level in pentacene films of one to four monolayers in thickness. We then discussed how these states affect secondary electron processes, such as photo-electron and secondary electron emission. These unoccupied states were measured for electrons at normal incidence to and reflection from the sample. In this chapter, we show measurements related to unoccupied states for incident electrons with non-zero in-plane momentum. This allows us to obtain a fuller picture of the unoccupied band structure of pentacene films.

6.1 Introduction

In this chapter, we discuss the unoccupied band structure of pentacene films above the vacuum level obtained using Angle-Resolved Reflected Electron Spectroscopy (ARRES). [1,2] We show the results obtained on pentacene films of two and three monolayers in thickness as well as the evolution of pentacene band structure as a result of beam damage, and discuss the features observed in the band structure.

6.2 Experimental Technique and Results

Fig. 6.1 shows the diffraction pattern corresponding to the thin film pentacene phase with a herringbone crystal structure. This pattern is obtained on a three-monolayer film. A few of the diffraction spots are annotated in the figure. The first-order spots (indicated by crosses) are not visible at the specific beam energy used for recording this diffraction pattern. The central spot, Γ (Gamma), corresponds to normal incidence and reflection of electrons, i.e. diffraction spot (0,0). In Fig. 6.1, we see also two rectangles. The bigger rectangle, with dashed lines, indicates the Brillouin zone of the pentacene crystal. Any point within this rectangle other than Γ represents electronic states with non-zero in-plane momenta. The smaller rectangle is discussed below.

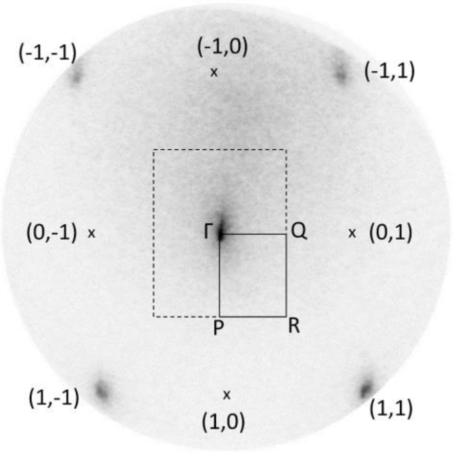

Fig. 6.1 Diffraction pattern of pentacene thin film with a herringbone crystal structure. A few of the diffraction spots are annotated. Γ spot denotes normal incidence and reflection of electrons, i.e. diffraction spot (0,0). Lower-order diffraction peaks are not visible at the beam energy used for recording the pattern. The dashed rectangle denotes the Brillouin zone. The solid rectangle denotes the region of the Brillouin zone imaged at various electron beam intensities (Fig. 6.2). The crosses indicate the position of the 1st-order diffraction peaks, not visible at the beam energy used for imaging the diffraction pattern.

We discussed earlier that we can probe the electronic density of states (DOS) above the vacuum level with LEEM-IV spectra. More precisely, the intensity of reflected electrons as a function of incident beam energy depends on the presence of such states as well as the probability of transmission into such states. The latter can in principle be calculated from the Schrödinger equation. In Fig. 5.2 of the previous chapter, LEEM-IV spectra of one to four monolayer films were shown, obtained by following the intensity variations at Γ, i.e. for normal incidence and reflection. By providing the incident electrons with non-zero in-plane momentum when interacting with the sample, i.e. by tilting the electron beam, we can measure the specular reflectivity (i.e. measure the LEEM-IV spectrum) of other points within the Brillouin zone as well. That is, by scanning the electron beam over (a part of) the Brillouin zone, instead of keeping it fixed at point Γ, we can obtain information about the DOS across the Brillouin zone. Thus, a fuller characterization of the band structure above the vacuum energy becomes possible. This technique is called 'scanning Angle-Resolved Reflected Electron Spectroscopy (ARRES)'. [1,2]

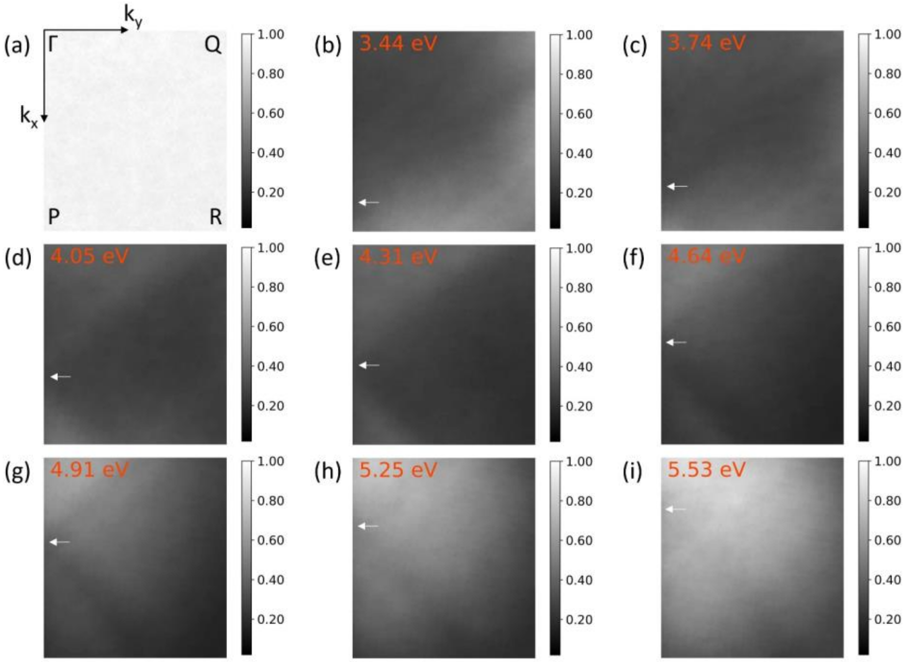

Fig. 6.2 Electron beam reflectivities of the part of pentacene thin film Brillouin zone denoted by the solid rectangle in Fig. 6.1, imaged at various beam energies. The corners of the imaged area annotated as Γ, P, Q and R in (a) correspond to the points in Fig. 6.1. The k_x and k_y axes indicate the directions of the in-plane momenta of the electrons. The Γ spot (top left corner) indicates normal incidence and reflection of electrons, i.e. no in-plane momenta. The white arrows highight the evolution of an electronic state along the k_x axis, i.e its movement towards the Γ spot, as a function of energy. The pentacene film is three monolayers in thickness. The image in (a) is recorded at a beam energy corrsponding to total reflection.

For the results in this chapter, we have measured the reflectivity as a function of position in reciprocal space. More exactly, for the portion of the Brillouin zone indicated by the smaller rectangle in Fig. 6.1, with solid lines and its corners annotated with Γ, P, R and Q. The results at nine different energies are shown in Fig. 6.2. They have been obtained locally on a three-monolayer pentacene film. In Fig. 6.2, each of the images show the reflectivity across the measured part of the Brillouin zone at the indicated energies. The corners of the reflectivity images in Fig. 6.2 (a-i) correspond to points Γ, P, R and Q, as annotated in Fig. 6.2(a). The interpretation of the images is similar to LEEM-IV spectra; existence of electronic states at certain in-plane momenta at a given energy results in a lower reflectivity, while lower DOS and bandgaps will generally result in a higher reflectivity. Given that each reflectivity image contains information about the DOS across (a portion of) the Brillouin zone at a given energy, stacking such reflectivity images obtained for electron energies within a given range, creates a full representation with all possible in-plane momenta across (the measured portion of) the Brillouin zone as a function of energy. In other words, it creates a full mapping related to the unoccupied band structure above the vacuum level. Figure 6.3(a) shows such a stack for the measurement that includes the selection of ARRES images shown in Fig. 6.2. We emphasize that, as mentioned earlier, the reflectivity also depends on the quantum mechanical probability of coupling of both the incident and reflected vacuum electron plane waves to the wavefunction of the available electronic states. The higher this probability, the lower the reflectivity. Furthermore, we note that the DOS measured with 'scanning ARRES' is the projection of the three-dimensional DOS of the sample along the out-of-plane direction (k_z).

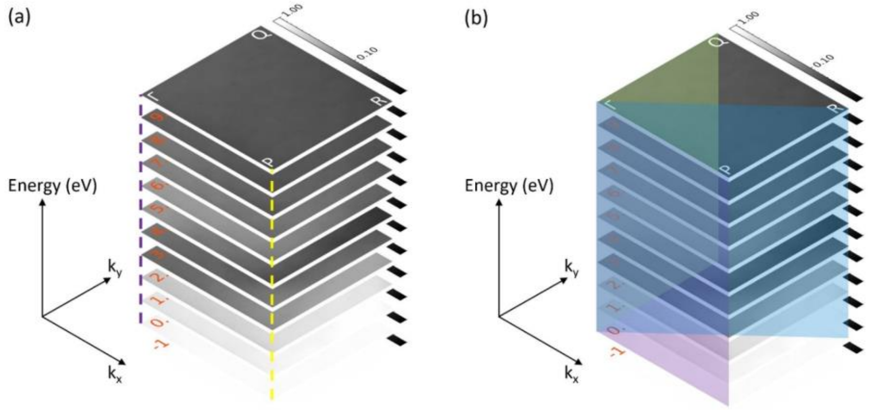

Fig. 6.3 A stack of reflectivity images of part of pentacene thin film Brillouin zone (solid rectangle in Fig. 6.1) imaged within the energy range -1 eV to 10 eV. 0 eV corresponds to the vacuum level. Such a stack visualizes the dependence of the unoccupied DOS on energy and in-plane momentum. The purple and yellow dashed lines in (a) correspond to Fig. 6.4, and show energy-dependence of the unoccupied DOS at various k_x values (with $k_y = 0$). The three planar cuts through the stack in (b) corresponds to Fig. 6.5.

As mentioned before, this ‘scanning ARRES’ technique is a generalization of LEEM-IV spectroscopy. Fig. 6.3(a) clarifies the relation between the two. Plotting the intensity variations as a function of incident electron energy along the purple dashed line yields the LEEM-IV spectrum at the point Γ, i.e. for normal incidence and reflection of electrons. This curve is shown in Fig. 6.4, with the corresponding color. It is essentially the same as the LEEM-IV curve for a three-monolayer pentacene film shown in Fig. 5.2 in the previous chapter, except that some details of the spectrum are more smeared out. With information about the DOS now available also for states with non-zero in-plane momenta (k_x and k_y), we can plot LEEM-IV spectra for any given state with arbitrary k_x and k_y. For example, the yellow dashed line in Fig. 6.3(a) corresponds to the LEEM-IV spectrum at point P (see Fig. 6.1). Fig. 6.4 shows LEEM-IV spectra for points Γ and P, as well as three equally-spaced intermediate points between the two. In the figure, the curves are annotated with numbers from 1 (point Γ) to 5 (point P).

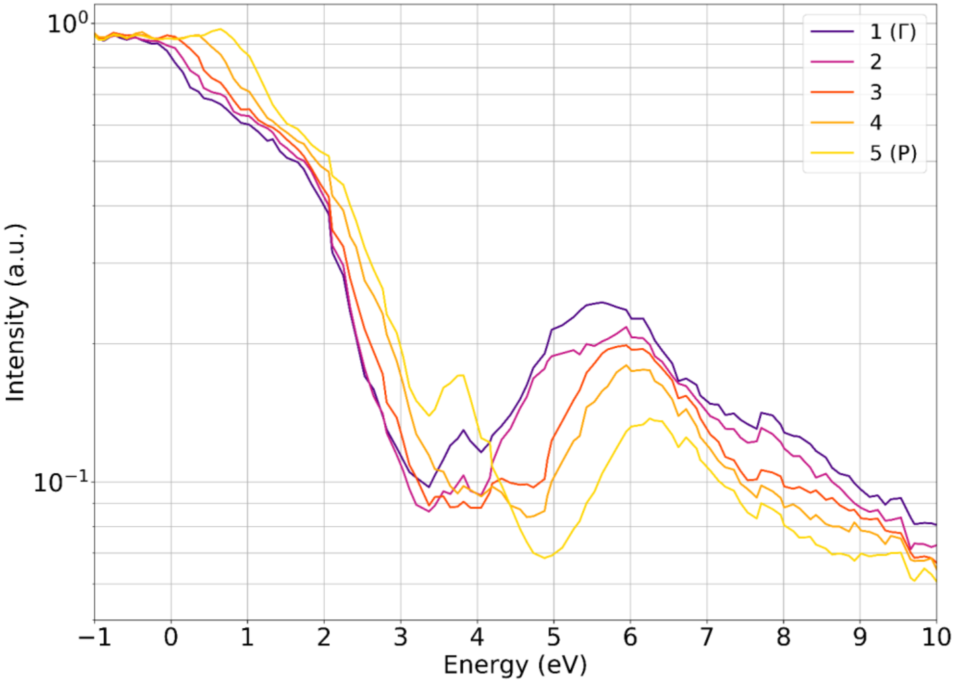

Fig. 6.4 The unoccupied DOS of a pentacene film three monolayers in thickness as a function of energy, obtained at five different points within the Brillouin zone along the Γ-P line in Fig. 6.3.

In addition to LEEM-IV spectra at points corresponding to specific in-plane momenta (k_x and k_y), such as those in Fig. 6.4, we can also plot the measured signal across arbitrary lines in the Brillouin zone. Three such lines extend from point Γ to each of the other corners of the rectangle, i.e. points P, Q and R. Fig. 6.3(b) visualizes these linecuts with planes in colors purple, green and blue, corresponding to Γ-P, Γ-Q and Γ-R linecuts, respectively. The results from each of these planes are shown in Fig. 6.5, for a three-monolayer pentacene film. Note that the LEEM-IV spectra in Fig. 6.4 correspond to intensity variations along five equally-spaced (with regards to k_x) vertical lines in Fig. 6.5(a). Two of these lines are highlighted (dashed purple and yellow), corresponding to LEEM-IV spectra at points Γ and P, respectively.

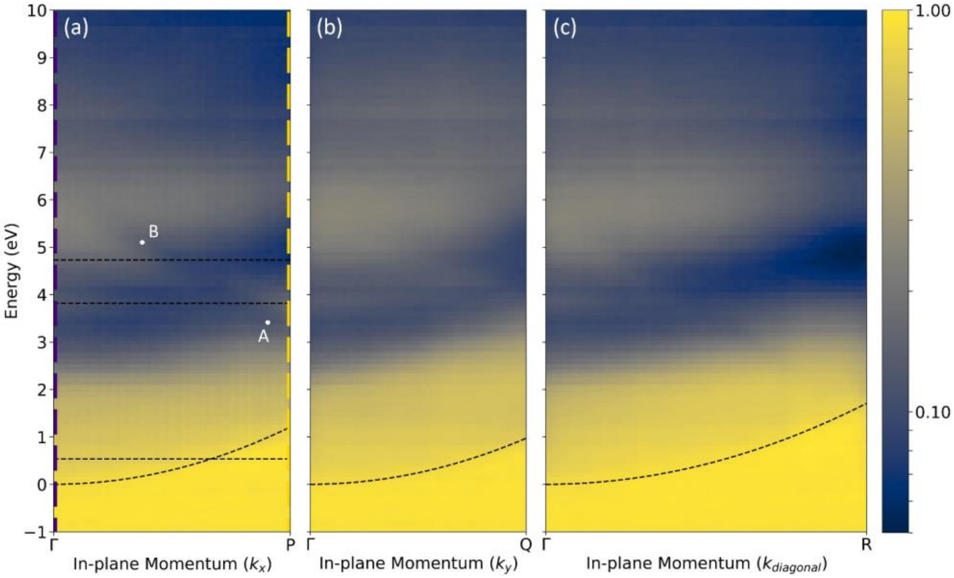

Fig. 6.5 Planar cuts through the stack in Fig. 6.3. Each subfigure shows the dependence of the unoccupied DOS of a three-monolayer pentacene film on both energy and in-plane momentum along three different directions (x, y and diagonal). The purple and yellow dashed lines in (a) correspond to dashed lines of the same colour in Fig. 6.3 and Fig. 6.4. The parabolic black dahsed line in (a), centered at point Γ, is a fit to the derivative of the linecut subfigure along the energy direction. This parabola indicates the mirror-mode transition energy as a function of in-plane momentum. The three horizontal black dashed lines in (a) correspond to Fig. 6.7. Points denoted “A” and “B” in (a) correspond to the evolution of an electronic state as a function of energy and in-plane momentum, also denoted by white arrows in Fig. 6.2.

Linecuts such as those in Fig. 6.5 and series of ARRES reflectivity images at constant energies such as those in Fig. 6.2, help us follow the evolution of electronic states across energy and in-plane momenta. For example, in Fig. 6.5(a) we see the movement of an electronic state near point P around 3.3 eV toward point Γ as the energy increases, forming a negatively sloped line. The two ends of this line are indicated by white dots called A and B in Fig. 6.5(a). This development can be observed also in Fig. 6.2 by following the position of the small white arrow moving toward Γ with increasing energy.

In all three subfigures of Fig. 6.5, we see black dashed lines with the shape of a parabola centered at point Γ and energy of 0 eV. These parabolas are obtained from parabolic fits to the derivatives of the linecut images in Fig. 6.5 along the energy direction. We discussed previously that in LEEM-IV spectra, negative energies indicate that the incident electrons do not have sufficient kinetic energy to reach the sample, resulting in total reflection. The energy at which the electrons reach the sample with an interaction energy of 0 eV is called the mirror-mode transition (MMT) energy. The electrons with this energy are slowed down to a kinetic energy of 0 eV by the electric field of 10 kV/mm between the grounded objective lens and the sample. Given that the energy of the incident electrons can be written as

$$\mathrm{E} = \frac{h^2}{8m\pi^2}\,(k_x^2 + k_y^2 + k_z^2),$$

it is easy to see that if the electrons have non-zero in-plane momenta, a higher kinetic energy is required for k_z (out-of-plane momentum) to be sufficient for the electrons to reach the sample. In other words, the MMT is shifted to higher values if the incident electrons have non-zero in-plane momenta. The schematic in Fig. 6.6 illustrates this point for three electrons with the same energy but different values of in-plane momenta (k_x). Here, electrons with larger in-plane momentum are reflected earlier than those with smaller in-plane momentum (and, hence, larger out-of-plane momentum). The shift of the MMT toward higher energies can also be seen in the LEEM-IV spectra in Fig. 6.4, where the spectra obtained at points with higher in-plane momenta (closer to point P) come out of total reflection at higher energies.

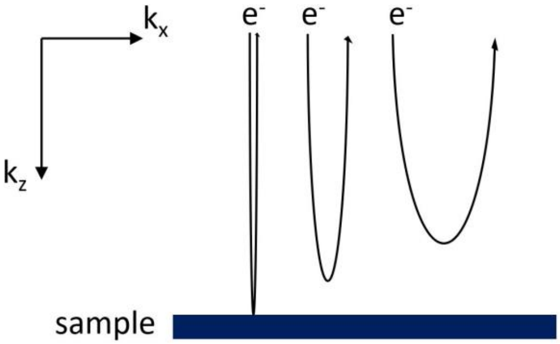

Fig. 6.6 Schematic illustrating the reflection of three electrons with the same energy but different in-plane momentum from the sample. The electrons with larger values of in-plane momentum are reflected earlier. In other words, they require higher energies to reach the sample, leading to the dependence of mirror-mode transition energy on in-plane momentum (see the parabolic dashed line in Fig. 6.5(a)).

In Fig. 6.5, all the points below the parabola correspond to total reflection. This is also observable in Fig. 6.7. Here, we have plotted reflected intensity as a function of in-plane momentum (k_x) at several fixed energies, obtained from profiles of the black horizontal dashed lines in Fig. 6.5(a). The line profile obtained at 0.53 eV shows high reflectivity close to point P (larger in-plane momentum and near-total reflection), and lower reflectivity close to point Γ (smaller in-plane momentum). The other two line profiles in Fig. 6.7, obtained at energies 3.82 eV and 4.73 eV show that the specular reflectivity (indicative of DOS) varies as a function of in-plane momentum. In other words, the electronic bands of pentacene films do not appear to be flat (see also Fig. 6.5). This is a surprising finding compared to the reports of relatively flat bands in pentacene at lower energies, such as around the Fermi energy. Photoemission measurements on thin film phase pentacene found a dispersion of only ~190 meV at room temperature [3]. Angle-Resolved Ultraviolet Photoelectron Spectroscopy (ARUPS) measurements on pentacene crystals also show dispersion values below 0.5 eV at room temperature. [4] Similarly, various theoretical calculations of pentacene in thin film and bulk phases show similar dispersion values, all well below 1 eV. [5,6] In contrast, the electronic bands in Fig. 6.5 appear to have a higher degree of dependence of DOS on in-plane momentum. We note the non-flatness of the DOS in Fig. 6.5 is not necessarily indicative of higher dispersion. The regions with higher DOS (lower reflectivity) in Fig. 6.5 can be a superimposition of several bands that are not individually resolved in our measurements. [7] Nonetheless, the band structure of pentacene shows a higher degree of dependence on in-plane momentum above the vacuum level compared to around Fermi energy.

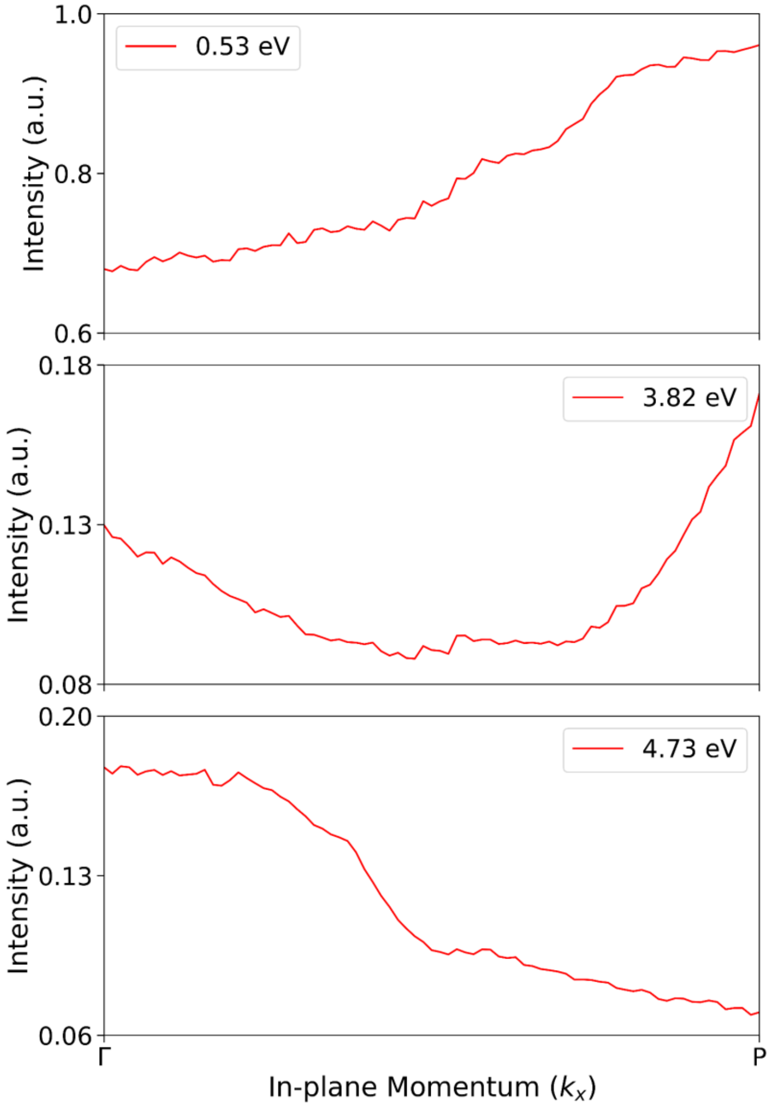

Fig. 6.7 Dependence of the unoccupied DOS of a three-monolayer pentacene film on in-plane momentum (k_x), obtained at three different energies of 0.53 eV, 3.82 eV and 4.73 eV above the vacuum level. The linecuts correspond to the horizontal black dashed lines in Fig. 6.5(a).

Furthermore, the width of the electronic bands in Fig. 6.5 appears to be greater than those around the Fermi energy. For example, the apparent width of the high-DOS region centered at 3.5 eV in a LEEM-IV at Γ (see Fig. 6.4) is bigger than 1 eV, while the width of the valence band in pentacene single crystals is a fraction of 1 eV. There are a few possible explanations for this. Theoretical calculations of pentacene band structure show that the bands near the Fermi level are widely separated/ fairly isolated from each other, while those much below or above the Fermi level are densely packed and overlapping. [8] Hence, the relatively wide bands in Fig. 6.5 can be the superimposition of several unresolved bands. [7] Another possible reason has to do with the molecular orbitals. Bandwidths of electronic bands are very sensitively dependent on the orbital overlap between adjacent molecules (or more generally, elements of a crystal), with more overlap expected to result in wider bands. Generally, higher-energy molecular orbitals are more delocalized. Hence, it is not surprising if the molecular orbitals of the unoccupied states above the vacuum level have stronger interactions with each other, leading to wider bands, and possibly more dispersion at these high energies. A third possible reason is the relatively low lifetime of the electronic states above the vacuum level, experimentally measured and found to vary between a few attoseconds and about 100 attoseconds in Ni(111), Ag(111) and Au(111). [9,10] From the Heisenberg uncertainty principle, a relatively short lifetime for these states results in larger uncertainty about their energies, manifested as larger apparent bandwidths. We note that from our measurements it is not possible to conclude which of these factors is dominant.

In Fig. 6.8, we show similar ARRES linecut measurements obtained on a two-monolayer pentacene film. Fig. 6.9 shows vertical linecuts (i.e. LEEM-IV spectra) at five equally-spaced intervals along k_x direction between the points Γ and P. Interestingly, the general shapes of the features in Fig. 6.8 do not differ much from those observed for the three-monolayer film. The main difference is that the features in the thicker film are more pronounced, as evident from a comparison of Fig. 6.4 and Fig. 6.9. This observation was discussed in the previous chapter, regarding the evolution of the LEEM-IV spectra for specularly-reflected electrons for pentacene films of one to four monolayers in thickness (Fig. 5.2). The fact that the features and dispersions in the two-monolayer film do not differ much from the three-monolayer film can be a result of relatively weak electronic interactions between the layers. In other words, the band structure of the film is probably mostly derived from that of an individual layer.

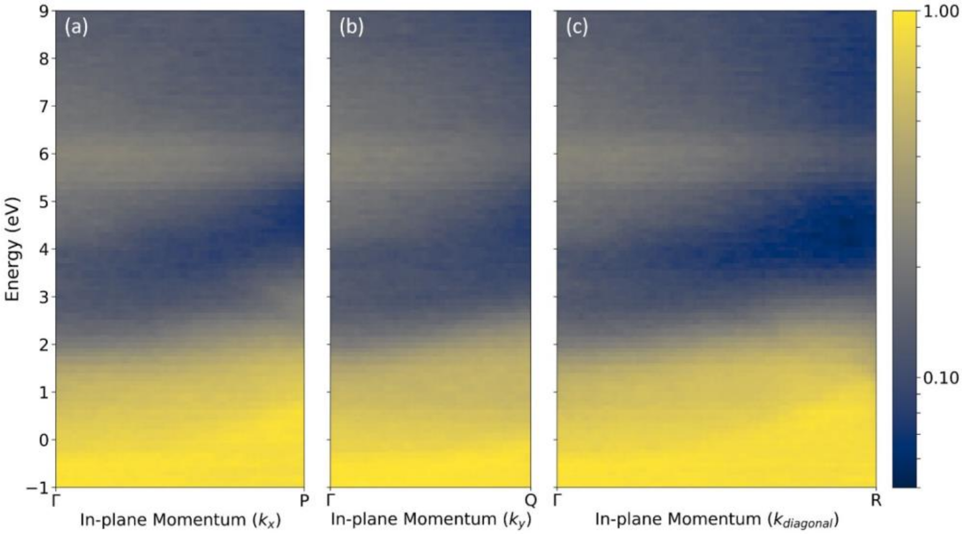

Fig. 6.8 Dependence of the unoccupied DOS of a two-monolayer pentacene film on energy and in-plane momentum along three different directions (x, y and diagonal). The points Γ, P, Q and R correspond to locations of the Brillouin zone indicated in Fig. 6.1. Note that two-monolayer and three-monolayer pentacene thin films have the same crystal structure.

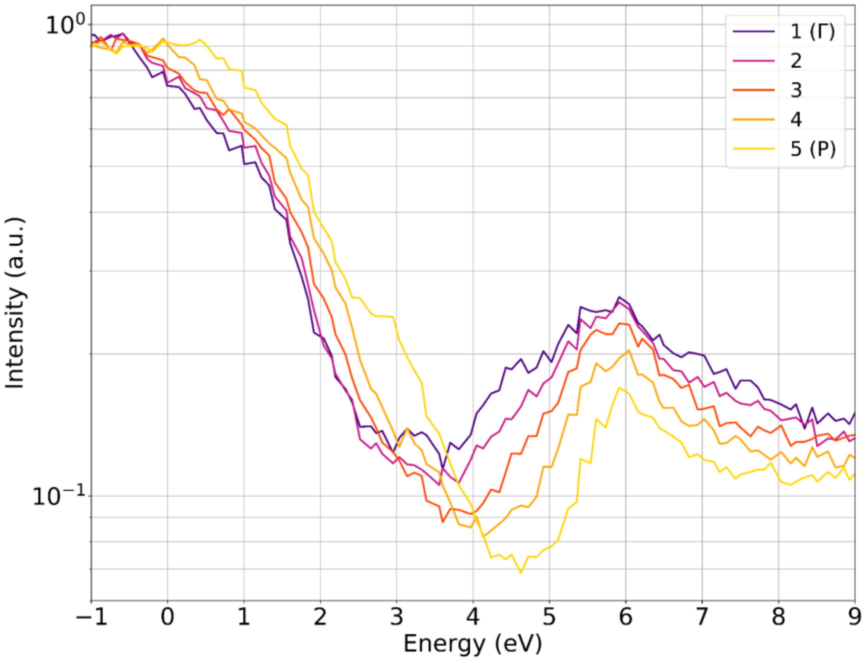

Fig. 6.9 Dependence of the unoccupied DOS of a two-monolayer pentacene film on energy, obtained at five diffferent spots along the Γ-P line (see Fig. 6.3).

In chapter 4, we explored electron beam irradiation damage to pentacene films and discussed the energy dependence of damage cross-section. In Fig. 4.4 of chapter 4, we demonstrated that the features in LEEM-IV spectra gradually diminish upon consecutive measurements on the same area of the sample, as a result of destruction of pentacene crystal lattice. [11] Here we show similar developments in ARRES measurements. Fig. 6.10 illustrates the changes in the Γ-P linecuts in three consecutive ARRES measurements on the same area. The increasing noise for the later measurements is due to the shorter integration time in obtaining the images in order to limit the amount of irradiation damage. Ignoring the noise, we observe lower intensity for the features in the later measurements. This is illustrated in Fig. 6.11, where the three spectra in each subfigure compare the LEEM-IV at Γ (left) and P (right) points between the three measurements. The band structure features in Fig. 6.10 also seem to be smeared out in the later measurements, although the noise makes it difficult to reach a definite conclusion. We also point out that given the diminishingly small damage cross-section found in chapter 4 for electrons up to 5-6 eV, the main features in the ARRES linecut plots for the three-monolayer and two-monolayer films (Fig. 6.5 and Fig. 6.8) are not an artefact of beam damage, and represent genuine characteristics of the DOS (modulated by the efficiency of coupling of the free electron wavefunction to those of the electronic states [12]).

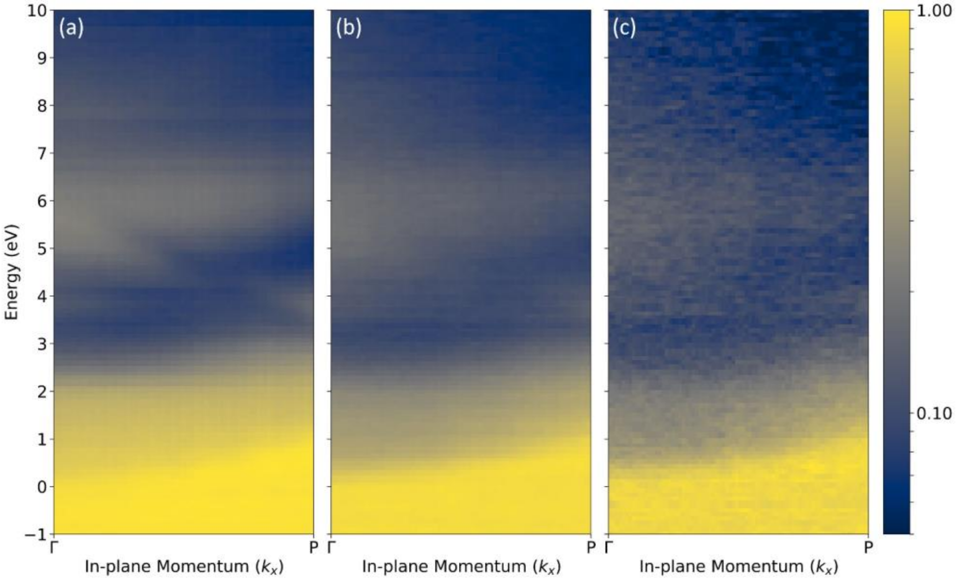

Fig. 6.10 The unoccupied band structure of a three-monolayer pentacene film in three consecutive measurements on the same area. The points Γ and P correspond to those in Fig. 6.1. The decrease in reflected intensity in each subsequent measurement is a result of electron beam irradiation damage. The increasing noise in the later measurements is due to the reduced integration time in obtaining the data.

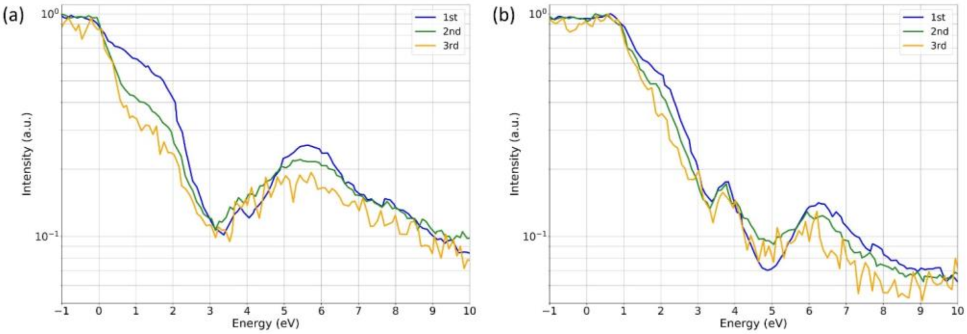

Fig. 6.11 Changes in the unoccupied DOS at points Γ and P, subfigures (a) and (b) respectively, during three consecutive measurements on the same area.

6.3 Conclusions

To summarize, we have performed scanning ARRES experiments on three-monolayer and two-monolayer pentacene films. The resulting signal gives direct information about the unoccupied band structure above the vacuum level. The films used are crystalline, in the thin film phase with a herringbone structure. We found a surprising degree of dependence of DOS on in-plane momenta, in contrast to the (nearly-) flat bands reported at energies below the vacuum level. We compared the band structure of three-monolayer and two-monolayer films and found the features to be generally the same on both, but more pronounced on the thicker film, in agreement with our observation of the evolution of LEEM-IV spectra as a function of layer count in the previous chapter. We also discussed the changes in ARRES linecuts as a result of electron beam damage from consecutive measurements on the same area. We found similar developments to those observed in chapter 4 for LEEM-IV spectra, i.e. diminishing of features due to damage to the pentacene film.

In the previous chapter, we discussed the critical role of unoccupied electronic states above the vacuum level, acting as ‘intermediate’ states, in photo-electron and secondary electron emission. Here, we demonstrated, for pentacene films, the dependence of these intermediate states on in-plane momentum. Our results, combined with information about the in-plane dispersion of the occupied ‘initial’ states, provide a fuller picture for the analysis of secondary electron processes, i.e. photo-electron and secondary electron emission, in pentacene films.

References

[1] J. Jobst, A. J. H. van der Torren, E. E. Krasovskii, J. Balgley, C. R. Dean, R. M. Tromp, and S. J. van der Molen, *Quantifying Electronic Band Interactions in van der Waals Materials Using Angle-Resolved Reflected-Electron Spectroscopy*, Nat. Commun. **7**, 13621 (2016).

[2] J. Jobst, J. Kautz, D. Geelen, R. M. Tromp, and S. J. van der Molen, *Nanoscale Measurements of Unoccupied Band Dispersion in Few-Layer Graphene*, Nat. Commun. **6**, 8926 (2015).

[3] N. Koch, A. Vollmer, I. Salzmann, B. Nickel, H. Weiss, and J. P. Rabe, *Evidence for Temperature-Dependent Electron Band Dispersion in Pentacene*, Phys. Rev. Lett. **96**, 156803 (2006).

[4] Y. Nakayama, Y. Mizuno, M. Hikasa, M. Yamamoto, M. Matsunami, S. Ideta, K. Tanaka, H. Ishii, and N. Ueno, *Single-Crystal Pentacene Valence-Band Dispersion and Its Temperature Dependence*, J. Phys. Chem. Lett. **8**, 1259 (2017).

[5] M. L. Tiago, S. G. Louie, M. L. Tiago, S. G. Louie, and J. E. Northrup, *Ab Initio Calculation of the Electronic and Optical Properties of Solid Pentacene*, Phys. Rev. B **67**, 115212 (2003).

[6] D. Nabok, P. Puschnig, C. Ambrosch-Draxl, O. Werzer, R. Resel, and D. M. Smilgies, *Crystal and Electronic Structures of Pentacene Thin Films from Grazing-Incidence x-Ray Diffraction and First-Principles Calculations*, Phys. Rev. B **76**, 235322 (2007).

[7] Björn Baumeier, *Private Communication*.

[8] X. Leng, J. Feng, T. Chen, C. Liu, and Y. Ma, *Optical Properties of Acene Molecules and Pentacene Crystal from the Many-Body Green's Function Method*, Phys. Chem. Chem. Phys. **18**, 30777 (2016).

[9] Zhensheng Tao, Cong Chen, Tibor Szilvási, Mark Keller, Manos Mavrikakis, Henry Kapteyn, and Margaret Murnane, *Direct Time-Domain Observation of Attosecond Final-State Lifetimes in Photoemission from Solids*, Science **353**, 62 (2016).

[10] R. Locher, L. Castiglioni, M. Lucchini, M. Greif, L. Gallmann, J. Osterwalder, M. Hengsberger, and U. Keller, *Energy-Dependent Photoemission Delays from Noble Metal Surfaces by Attosecond Interferometry*, Optica **2**, 405 (2015).

[11] A. Tebyani, F. B. Baalbergen, R. M. Tromp, and S. J. van der Molen, *Low-Energy Electron Irradiation Damage in Few-Monolayer Pentacene Films*, J. Phys. Chem. C **125**, 26150 (2021).

[12] J. I. Flege and E. E. Krasovskii, *Intensity-Voltage Low-Energy Electron Microscopy for Functional Materials Characterization*, Phys. Status Solidi RRL **8**, 463 (2014).

7

Low Energy Electron Microscopy at Cryogenic Temperatures *

Abstract

We describe a cryogenic sample chamber for low energy electron microscopy (LEEM), and present first experimental results. Modifications to our IBM/SPECS aberration-corrected LEEM instrument are presented first. These include incorporation of mechanisms for cooling the sample and its surroundings, and reduction of various sources of heat load. Using both liquid nitrogen and liquid helium, we have reached sample temperatures down to about 15 K. We also present first results for low-temperature LEEM, obtained on a three-monolayer pentacene film. Specifically, we observe a reduction of the electron beam irradiation damage cross-section at 15 eV by more than a factor of five upon cooling from 300 K down to 52 K. We also observe changes in the LEEM-IV spectra of the sample upon cooling, and discuss possible causes.

---

* This chapter has been published as "Low energy electron microscopy at cryogenic temperatures", A. Tebyani, S. Schramm, M. Hesselberth, D. Boltje, J. Jobst, R.M. Tromp, S.J. van der Molen - Ultramicroscopy 253, 113815 (2023)

7.1 Introduction

Since its realization in 1985 [1], low-energy electron microscopy (LEEM) has been successfully employed to study a plethora of surface phenomena, in particular for real-time observation of dynamic processes at surfaces including phase transitions and growth of a large variety of materials such as molecular layers, oxide films, metals, two-dimensional materials, etc. [2–15] Advancements such as the addition of aberration-correction [16–18], spin-polarization of the electron beam [19,20] and the possibility for complementary imaging with low-energy electrons transmitted through the sample (eV-TEM) [21] have further enhanced the capabilities of LEEM. Moreover, various other techniques related to LEEM have made it possible to not only investigate the microstructure of the sample surface in real and reciprocal space, but also to extract information about other properties (such as electronic band structure) and perform various forms of spectroscopy. Some examples include photoemission electron microscopy (PEEM) and angle-resolved photoemission spectroscopy (ARPES), energy filtering and electron energy loss spectroscopy (EELS) [22–25], angle-resolved reflected-electron spectroscopy (ARRES) [26,27] and low energy electron potentiometry (LEEP) [28].

So far, LEEM measurements have mostly been performed on samples with temperatures above room temperature. However, there have been a number of reports of LEEM operation at cryogenic temperatures. In 2000, Tober et. al. reported the first spin-polarized LEEM images obtained below room temperature (at 118 K) on Co thin films grown on Au(111), using a liquid-nitrogen-cooled spin-polarized LEEM instrument [29]. Some other examples include measurements of magnetic transitions in ultrathin Fe films on Cu(100) down to 248 K [8], growth of indium on Si(111) down to -100˚C [14], the Verwey transition of the magnetic material Fe_3O_4 down to 100 K [7,30], evolution of magnetic domains of a Tb film on W(110) cooled down to 80 K [31], and the report of sample temperatures >100 K reached in the ALBA LEEM instrument [32]. Meanwhile, advancements in instrumentation have been reported in similar (cathode-lens based) microscopy techniques, extending the range of available sample temperatures into cryogenic temperatures. For example, in 2012, Doran et. al. reported an X-ray PEEM (X-PEEM) instrument capable of imaging down to 25 K. [33] In 2015, Tusche et. al. reported a spin resolving microscope, with cathode objective lens design, capable of high resolution imaging of the momentum distribution of photoelectrons down to 18 K [34]. More recently, G. Schönhense et. al. have reported electronic band mapping of various materials such as $TiTe_2$, Mo, Re, $YbRh_2Si_2$ and W(110), using X-ray photoelectron microscopy down to 20-30 K [35–38]. Some other examples of PEEM and X-ray Magnetic Circular Dichroism (XMCD) measurements at cryogenic temperatures include evolution of magnetic domains of Fe_3GeTe_2 down to 110 K [39], structural phase transition of V_2O_3 down to 150 K [40], imaging of a superconducting-ferromagnet hybrid at 45 K [41], linear dichroism of FeSe at 11 K and $BaFe_2(As_{0.87}P_{0.13})_2$ at 65 K [42], growth of anthracene layers on silicon at ~ -40˚C [6], and measurements on van der Waals ferromagnet Fe_5GeTe_2 down to 50 K [43], among others.

Here, we present a cryogenic sample chamber, incorporated into the aberration-corrected IBM/SPECS LEEM instrument [16,17]. It has the capability to cool the sample to controllable cryogenic temperatures down to ~15 K. Our design is compatible with the stringent requirements imposed by the nature of LEEM. Such requirements include the fact that the sample itself is biased with a voltage of -15 kV (as it acts as the cathode in the cathode objective lens). Furthermore, vibrations from the cooling mechanism are not to compromise the desired imaging resolution. Next, we present our first results for low-temperature LEEM on a three-monolayer pentacene film.

7.2 Experimental Technique

The cryogenic sample chamber is incorporated in the ESCHER LEEM instrument at Leiden University, an aberration-corrected IBM/SPECS LEEM instrument. [16,17] The overall design has previously been reported in Ref. [44]. As shown in Fig. 7.1, in ESCHER, the central illumination and projector column is shared between a room/high-temperature sample chamber and the low-temperature chamber on which we focus here. Via the top magnetic prism we can direct the electron beam to either of the sample chambers, by controlling the current direction. The design of the cryogenic chamber resembles that of the typical room/high-temperature chamber; however, the requirements for low-temperature operation have led to various modifications, as discussed in detail below.

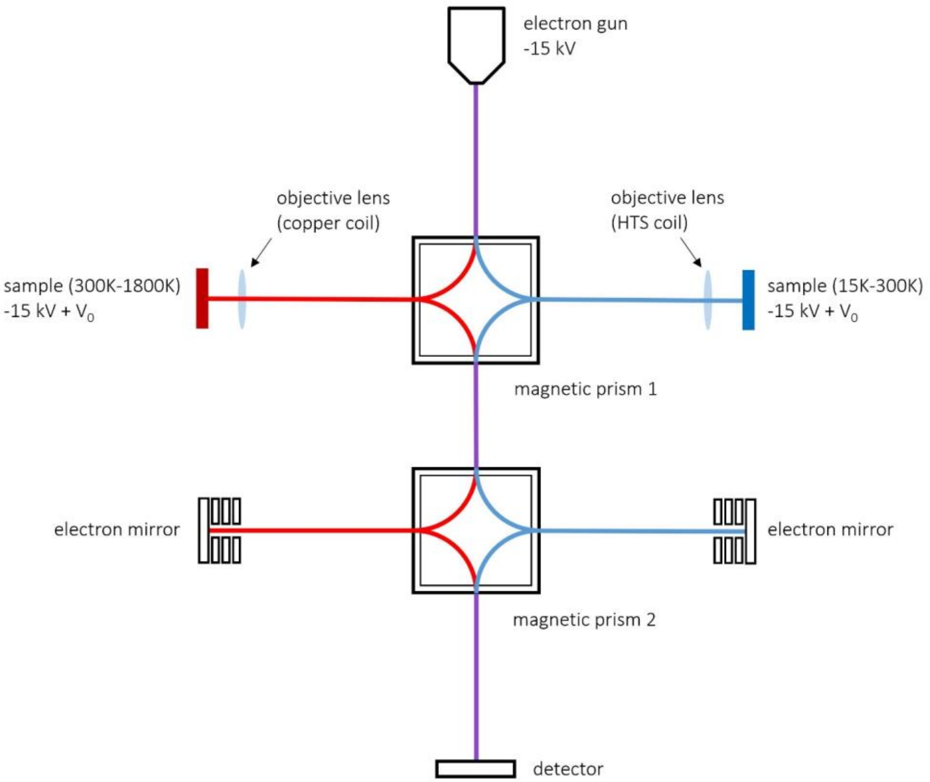

Fig. 7.1 Schematic of the ESCHER LEEM instrument. Electrons are emitted from the gun and go through the column with a kinetic energy of 15 keV. Before interaction with the sample, they are decelerated to a kinetic energy of eV_0. The beam path for the cryogenic and room/high-temperature operation is indicated in blue and red, respectively. The central column is shared between the cryogenic and room/high-temperature sides (purple beam path). To maintain the required symmetry, the two sides have separate aberration-correcting electron mirrors. The objective lens coil for the room/high-temperature side is comprised of a copper coil, while for the cryogenic side, a high-temperature superconducting (HTS) coil is used to prevent Joule heating and, hence, reduce the total heat load.

After emission from the electron gun and traversing the column with a kinetic energy of 15 keV, the electron beam is directed toward the sample (from the left in Fig. 7.1 and Fig. 7.2(a)) via magnetic prism 1. Before interacting with the sample, the incoming beam is decelerated to an energy of only a few eV, as a result of an electric field between the sample and the objective lens (~15 kV/mm). This interaction energy is tuned precisely via the sample potential. Afterwards, the reflected electrons are collected by the same electric field and, after passing through an aberration-correcting path comprising of an electron mirror, are guided toward the detector. The entire beam path is shown in Fig. 7.1. The aberration-correcting section for the cryogenic and the room/high-temperature operation are separate, as can be seen in Fig. 7.1. Furthermore, the cryogenic chamber is equipped with its own separate load lock and sample transfer mechanism. However, sample transfer between the cryogenic and the room/high-temperature chambers without exposure of the sample to ambient conditions is not possible. The two sample chambers share the central column of the microscope, so that simultaneous measurements in the cryogenic and the room/high-temperature chambers are not possible. Alternating between measuring at either sides (i.e. on different samples) is quick and simple, however.

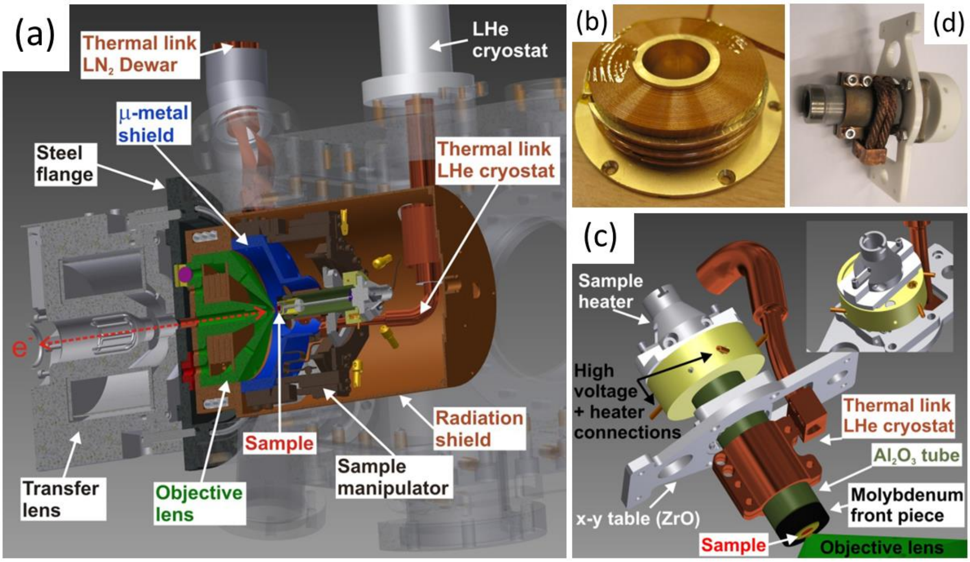

Fig. 7.2 Detailed schematic of the cryogenic sample chamber. (a) Schematic cross-section of the cryogenic setup. Electrons enter the chamber from the left. Various elements are highlighted and annotated. (b) Photograph showing the HTS coil assembly. The four disks are separated by 1-mm thick Au-plated copper plates (c) Schematic of the cryogenic sample holder, with its various components highlighted and annotated. The copper clamp around the sapphire tube is connected to the helium flow cryostat. (d) Photograph of the sample holder assembly

A detailed schematic of the cryogenic sample chamber is illustrated in Fig. 7.2(a). In the cryogenic chamber, the electromagnetic objective lens is excited by a high-temperature superconducting (HTS) coil, instead of a copper coil as used in the room/high-temperature chamber, in order to avoid Joule heating of the cryogenic set-up. The HTS assembly is comprised of a stack of four disk-shaped windings of a HTS tape (SCS3050-i, Superpower Inc.) separated by 1-mm thick Au-plated copper plates, cooled to liquid-nitrogen temperature. A picture of the HTS coil assembly, mounted to the objective lens base, is shown in Fig. 7.2(b).

Regarding heat transfer mechanisms, we are mainly concerned with minimizing radiative heat transfer through vacuum as well as conductive heat transfer through solids and solid/solid interfaces. In our design, the entire cathode objective lens and the sample stage are cooled with liquid nitrogen to a fixed temperature of ~80K. Furthermore, all these elements are enclosed in an Au-plated copper cylinder which is also cooled to the same temperature. This cylinder acts as a radiation shield against the room temperature environment, and reduces the radiative heat load on the sample holder by an estimated ~99.6% [45]. This is due to the fact that the net exchange of radiative heat is proportional to $(T_h^4 - T_c^4)$, T_h and T_c being the temperature of the hotter and colder sides of heat transfer, respectively. Placement of a cooled heat shield reduces T_h from 300K to 80K. Cooling the lens also prevents radiative heat load from an otherwise-warm lens on the sample. The cooling of all these elements is carried out via a flexible copper braid connection to a liquid nitrogen bath dewar (see Fig. 7.2(a)). The flexibility of this connection dampens the vibrations coming from the dewar, hence allowing for high-resolution imaging afforded by the aberration-correcting optics. Cooling all these elements also minimizes cryogenic pumping by the sample and has the added value of reducing thermal gradients.

Additionally, the sample itself can be cooled further via a flexible copper braid connected to a low-vibration helium flow cryostat (Advanced Research Systems Inc. LT3B), allowing for operation at further reduced temperatures. The copper braid mounted on the cold finger of the flow cryostat is clamped around a sapphire tube, at the end of which the sample (inside a molybdenum cap) is mounted. A schematic and a picture of these parts are shown in Fig. 7.2(c-d). The sapphire tube provides electrical insulation between the sample (biased at -15kV) and the flow cryostat, whilst having a relatively high thermal conductivity that increases with decreasing temperature. Only the sample and its immediate vicinity are cooled by the flow cryostat. Sample temperatures down to 15K have been achieved. The thermometer (silicon diode) for this readout is connected to the copper braid at the point of connection to the flow cryostat. Sample temperatures were calibrated with a second thermometer placed on the sample, and showed a difference of about 2K with the flow cryostat. The entire cool down process from room temperature until the microscope is operational takes about 8 hours. This time scale is dominated by the time it takes for the HTS lens to have sufficient critical current. We note that the sample itself can be cooled much faster. Also, the stabilisation time is negligible. Fig. 7.3 shows the final stage of the sample cool down (to 19K here). Cooling the sample with liquid helium via the flow cryostat while the HTS lens is being cooled can expedite reaching the required critical current in the lens. Future improvements by replacing the copper braid connection to the liquid nitrogen bath dewar with a stronger one can be expected to further reduce this waiting time. A resistive heater element placed behind the sample can be used to heat the sample by electron bombardment up to ~1400K, allowing for *in situ* sample cleaning and preparation at elevated temperatures. Furthermore, an evaporator connected to the sample chamber allows for *in situ* deposition of various materials at ultrahigh vacuum (UHV) pressures.

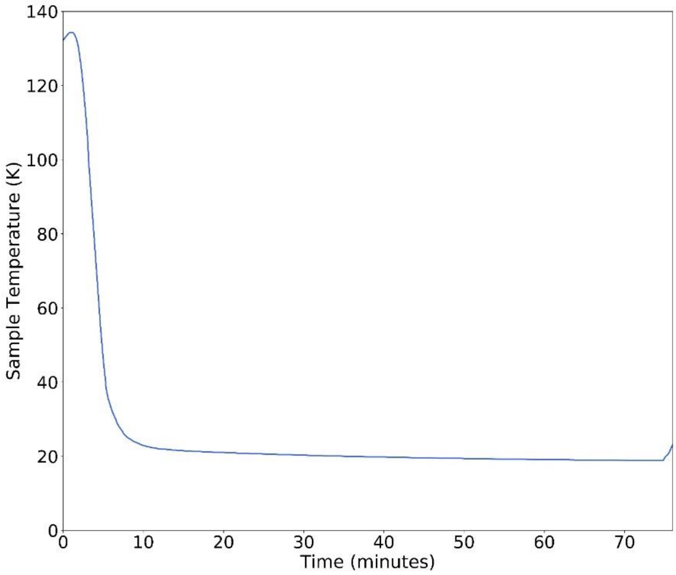

Fig. 7.3 Sample temperature during the final stage of sample cooling to 19 K. Note that the liquid He supply was stopped after 75 minutes.

The mounting of the cryogenic components has been designed such that the conductive heat transfer from the rest of the microscope (which is at room temperature) to the aforementioned liquid-nitrogen-cooled parts is minimized. We chose for mechanical mounts consisting of only three ZrO screws and four ZrO spheres, with minimal contact area with the room-temperature parts. [45] One of these spheres is colored as a purple circle behind the objective lens in Fig. 7.2(a). Finally, the sample also needs to be adjustable with five degrees of freedom: x and y in-plane movements to change the illuminated area on the sample, z-adjustment as well as two perpendicular tilt-angles to align the sample with respect to the optical axis (i.e. the illuminating electrons). These movements are powered by piezo elements in the sample stage. For low-temperature operation, the SmarAct piezomotors used at the room/high-temperature side did not suffice. Hence, new piezomotors capable of generating sufficient force at liquid nitrogen temperature, have been designed and produced in our lab. The piezomotors employ compact actuators coupled to a thermal-expansion-compensating preload mechanism and have optimized tribological elements and compact roller bearings. The actuators in each motor are driven mutually out of phase using custom power electronics. Actuator control signals are linear ramps with a slope-matched parabolic onset. These motors, each measuring 30x17x8.5 mm, achieve a driving force of 7N at 77K. They are incorporated in the cryogenic sample stage and provide high-precision control of sample position and tilt in all directions. The piezomotors will be described in a separate publication.

7.3 Results and Discussion

First, we present a real-space image obtained in the cryogenic chamber. Figure 7.4 shows a bright-field image of a Si(111) surface, imaged at 58 K with 10.3 eV electrons. Silicon was first flashed at high temperature in order to remove the native oxide layer. Upon cooling down, the surface undergoes a 7×7 reconstruction, [46] also manifested in the diffraction pattern. The bright domains in Fig. 7.4 are a result of the surface reconstruction.

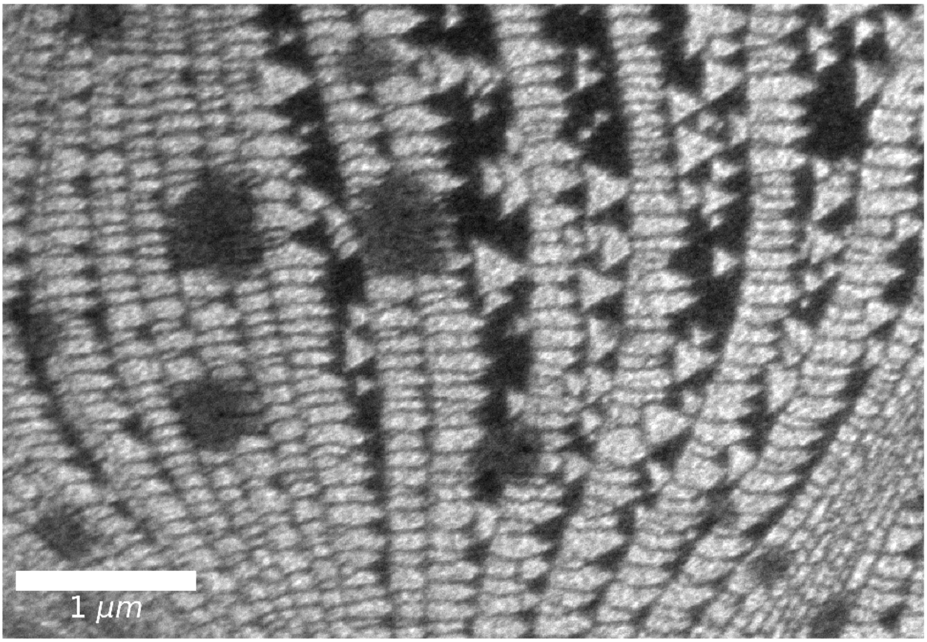

Fig. 7.4 Bright-field image of Si(111) 7×7 surface reconstruction, imaged at 58 K with 10.3 eV electrons

Next, we present the first systematic LEEM measurements within our cryogenic chamber, obtained on a pentacene film. The pentacene layers have first been grown on a Si(111) substrate via sublimation from a Knudsen cell evaporator. Growth is monitored in real-time with both LEEM and PEEM. [2,3,47] The film is covered mostly with three monolayers of pentacene, but there exist layer count variations within the beam diameter (60 μm^2), because the growth of each subsequent layer starts before the previous layer is fully finished. Since sublimation of molecules was not possible in the cryogenic chamber at the time, the sample was made in the room/high-temperature chamber and was subsequently transferred to the cryogenic chamber, with less than 30 minutes exposure to ambient atmosphere. After transfer to the cryogenic chamber and cooling down, we observe a sharp diffraction pattern corresponding to the herringbone crystal structure of pentacene (see Fig. 1.1 in chapter 1), similar to what we had observed in the room-temperature chamber after growth. Below, we show electron beam irradiation damage and spectroscopy measurements on the sample, all carried out at a range of low temperatures, in the cryogenic chamber. At low temperatures, we observed slight charging from the electron beam. Shining UV photons (from a Hg lamp connected to the chamber) during the measurements successfully counteracted the charging effect. We have established that the pentacene films are stable during prolonged Hg-UV ($h\nu$=4.9 eV) illumination.

First, we investigate electron irradiation damage to the sample. In chapter 4, [48] we examined damage to the crystalline structure of two- to four-monolayer pentacene films as a result of exposure to electrons with energies in the 0-40 eV range, and found the corresponding damage cross-section for each energy. Here, we show the results for a fixed beam energy of 15 eV, obtained at four different temperatures. The procedure followed to quantify the damage has been described in detail in Ref. [48]. In short, we observe and record the decay of the diffraction pattern of a pentacene area in real-time. Afterwards, Lorentzian curves are fitted to the line profile of the 0^{th}-order diffraction peak in each frame of the recording. Fig. 7.5 shows the evolution of the amplitudes of these Lorentzian fits over time (i.e. with accumulating dose), obtained at four different temperatures. A simple exponential fit of the form $Ae^{-\sigma \cdot D} + B$ to the data yields the damage cross-section at a given temperature and beam energy. Here, D is the accumulated dose over time in units of number of electrons per nm^2, σ is the damage cross-section in nm^2, and A and B are constants. It is evident from Fig. 7.5 that the decay of the diffraction peak intensity proceeds at a slower rate as the temperature of the sample decreases. The inset shows that the damage cross-section is reduced by a factor of ~5.4 upon cooling down from 300 K to 52 K. This is not surprising, given that in Transmission Electron Microscopy (TEM), cryogenic temperatures are used in order to reduce beam damage and extend sample lifetime. [49–52]

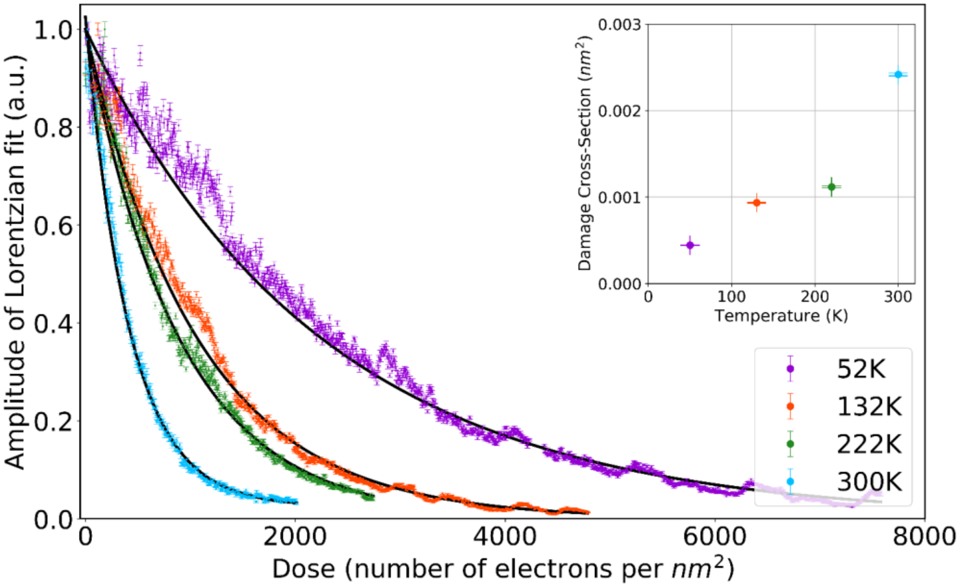

Fig. 7.5 Irradiation damage from a beam of 15 eV electrons to a pentacene film three monolayers in thickness. To quantify the damage, Lorentzian curves are fit to the spot profile of the 0th-order diffraction peak. The plot shows the decay of diffraction intensity over time, as a result of accumulated dose. Beam damage is obtained at four different temperatures of 52 K, 132 K, 222 K and 300 K. The solid black curves are simple exponential fits of the form $Ae^{-\sigma \cdot D} + B$, where D is the accumulated dose (horizontal axis), σ is damage cross-section in nm^2, and A and B are constants. Cross-sections obtained from the fits are displayed in the inset figure. The colors correspond to the temperatures in the main figure legend.

The key to understanding our observations is consideration of the mechanisms that lead to damage. These include electron attachment, particularly at lower electron energies, as well as impact excitation and impact ionization (dominant at higher energies). Each of these mechanisms leads to chemical changes in the molecule and beam damage in a different way, with the activation energies for various damage mechanisms not being the same. Hence, they will likely not be suppressed equally upon cooling. Irradiation studies of self-assembled monolayers in the range 50-300 K suggest that reactions involving transport of small fragments or single atoms proceed nearly independent of temperature, while those involving transport of heavy fragments are efficiently suppressed by cooling. [53] Another beam damage study in aromatic organic single crystals reported two activation energies between 4K and 293K, with the higher-energy component ascribed to violent atomic movement and bond scission. [51]

Dissociative electron attachment is reported to be most effective in the electron energy range 5-10 eV for pentacene. [54,55] This energy range also largely coincides with the wide resonance for the excitation of the carbon-hydrogen bond in benzene from 5.5 eV to 10 eV with a shoulder at 4-5.5 eV [56], that can lead to hydrogen removal. For the beam energy of 15 eV, as used here, we expect impact excitation and ionization to be dominant, with the ionization of π-electrons starting at 6.6 eV and the ionization of σ bonds starting at 11 eV. [57–61] Given the notable temperature-dependence in the damage cross-sections observed in Fig. 7.5, it is possible that the main damage mechanism at 15 eV is fragmentation of pentacene into bigger fragments and the diffusion of those fragments, rather than scission of carbon-carbon double bonds or carbon-hydrogen bond and removal of hydrogen. However, further measurements at different beam energies are required to reach conclusions about damage at low temperatures.

Next, we study LEEM-IV spectra of pentacene as a function of temperature. As mentioned earlier, in LEEM the interaction energy of the electrons with the sample can be precisely tuned. Plotting the changes in the intensity of the 0^{th}-order diffraction peak (i.e. specularly-reflected electrons) as a function of the incident beam energy yields a so-called LEEM-IV (intensity vs. voltage) spectrum. LEEM-IV spectra are a fingerprint of the crystal and electronic band structure of the probed area, and -at low energies as used here- are predominantly determined by the unoccupied electronic density of states (DOS) above the vacuum level. [26,27,62–66] At beam energies where the DOS is high, incoming electrons can enter the sample, resulting in lower reflectivity in the LEEM-IV spectrum. Vice versa, a bandgap leads to high reflectivity. LEEM-IV spectra of the three-monolayer pentacene film obtained at different temperatures from 52 K to 300 K are plotted in Fig. 7.6. Each spectrum is obtained from a pristine area on the sample. The spectra are individually shifted (by no more than 0.3 eV) so that their mirror-mode transition energies (from full reflection to interaction with the sample) are at 0 eV; this is to compensate for slight beam tilt in the original recordings. Note that an energy of 0 eV corresponds to electrons having kinetic energy of 0 eV when they reach the sample. Negative energies imply the electrons do not have sufficient kinetic energy to reach the sample, resulting in total reflection.

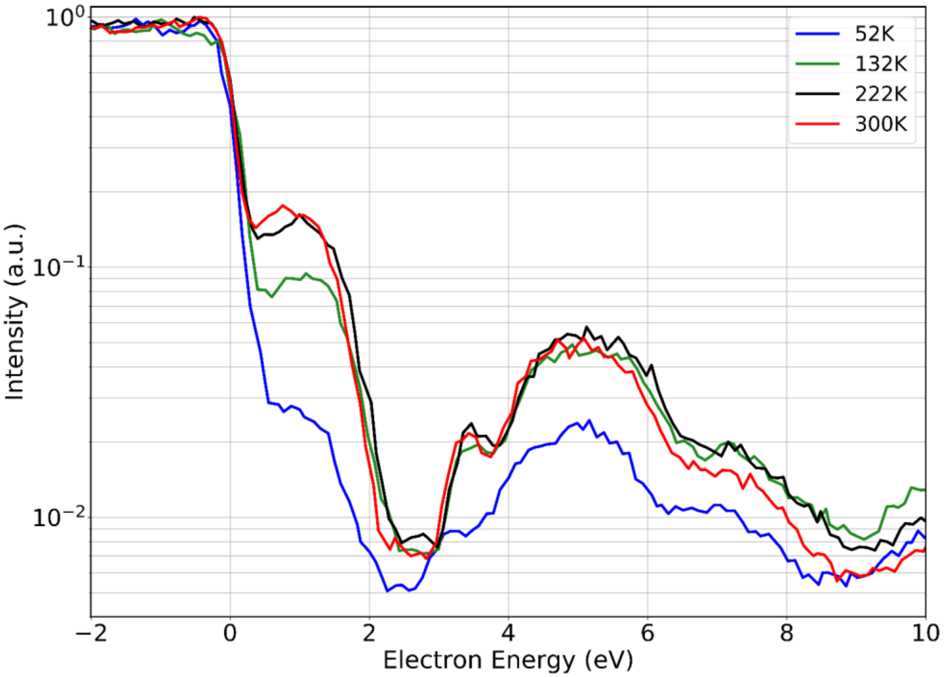

Fig. 7.6 LEEM-IV spectra of a three-monolayer pentacene film measured at different temperatures

Interestingly, in Fig. 7.6 we observe that most spectral features become weaker and less sharp upon cooling the sample. There are several possible explanations for this. The first would be the creation of disorder in the film upon cooling, as a result of the different thermal expansion coefficients between the silicon substrate and the pentacene layer. In our beam damage study [48] we observed that repeated measurements of LEEM-IV spectra on the same area lead to the diminishing and ultimate disappearance of the spectral features. The observation was attributed to irreversible chemical and structural changes to the film with increasing exposure to the beam, leading to disorder and fading of the diffraction pattern. However, in that study, all LEEM-IV features decreased in intensity with increasing damage and disorder. Here, on the other hand, a comparison of LEEM-IV spectra at 132 K and 222 K shows that while the intensity around 1 eV is lower for the LEEM-IV at 132 K, the intensity at the wide peak around 5 eV is the same for both. Another possible explanation is adsorption of contaminants on the sample surface upon cooling (note that the measurements were carried out at a pressure of ~1.0×10^{-9} mbar). However, this can be considered as another form of disorder at the surface, and hence, expected to reduce the intensity of all parts of the LEEM-IV spectra equally. Furthermore, the diffraction pattern of the sample was continuously recorded during warm-up from 52 K up to 300 K. Line profiles of the 0th-order diffraction spot in these recordings did not show any change as a function of temperature, i.e. neither widening nor sharpening. This rules out the emergence of lattice disorder and surface contamination upon cooling as causes of the changes observed in the LEEM-IV spectra in Fig. 7.6. A third possible explanation is that upon cooling, the overlap of the unoccupied molecular orbitals increases, due to contraction of the pentacene lattice. This, in turn, can lead to a broadening of the electronic bands and suppression of bandgaps. Such a development is then expected to result in lower reflectivity at lower temperatures. Note, however, that in that case, the exact changes expected will depend on the details of the electronic states and orbital overlaps. And of course, the changes in the LEEM-IV spectra could be a combination of several factors. Further measurements, for example to investigate possible changes in the dispersion of these electronic states upon cooling using ARRES [26,27], and/or to study temperature-dependent changes in electron irradiation damage cross-sections as a function of incident electron energy, are required to clarify the observations in Figs. 7.5 and 7.6.

7.4 Conclusions

We have presented the design of a cryogenic LEEM sample chamber, as well as the first results from low-temperature measurements on a pentacene film. Although similar to the room/high-temperature sample chamber of an IBM/SPECS LEEM, the low-temperature requirements lead to several design modifications to reduce the heat load, apart from the features to cool down the sample. Sample temperatures as low as 15K have been achieved, utilizing a helium flow cryostat that cools the sample and its vicinity as well as a nitrogen dewar that cools the superconducting objective lens, the entire sample stage and a radiation shield around it. Our first observations on a three-monolayer pentacene film are promising, showing a reduction in beam damage cross-section by more than a factor of 5 upon cooling from 300K to 52K, for 15 eV electrons. The LEEM-IV spectra of the sample also exhibited systematic change with temperature, although further measurements are required to conclusively explain the observations. With the cryogenic chamber, the ESCHER microscope will give access to physical phenomena over a very broad temperature range from ~15K up to 1800K, enabling novel experiments to address questions in surface science and condensed matter physics in both cryogenic and high temperatures.

References

[1] W. Telieps and E. Bauer, *An Analytical Reflection and Emission UHV Surface Electron Microscope*, Ultramicroscopy **17**, 57 (1985).

[2] Frank-J. Meyer zu Heringdorf, M. C. Reuter, and & R. M. Tromp, *Growth Dynamics of Pentacene Thin Films*, Nature **412**, 517 (2001).

[3] A. Al-Mahboob, J. T. Sadowski, Y. Fujikawa, K. Nakajima, and T. Sakurai, *Kinetics-Driven Anisotropic Growth of Pentacene Thin Films*, Phys. Rev. B **77**, 035426 (2008).

[4] J. Kautz, M. W. Copel, M. S. Gordon, R. M. Tromp, and S. J. van der Molen, *Titration of Submonolayer Au Growth on Si(111)*, Phys. Rev. B **89**, 035416 (2014).

[5] A. J. H. van der Torren, S. J. van der Molen, and J. Aarts, *Imaging Pulsed Laser Deposition Growth of Homo-Epitaxial* $SrTiO_3$ *by Low-Energy Electron Microscopy*, Nanotechnology **27**, 495702 (2016).

[6] N. M. Buckanie and F.-J. Meyer zu Heringdorf, *Photoemission Electron Microscopy Study of Anthracene Growth on Si(1 1 1)*, Surf. Sci. **601**, 1701 (2007).

[7] J. de la Figuera et al., *Real-Space Imaging of the Verwey Transition at the (100) Surface of Magnetite*, Phys. Rev. B **88**, 161410(R) (2013).

[8] K. L. Man, M. S. Altman, and H. Poppa, *Spin Polarized Low Energy Electron Microscopy Investigations of Magnetic Transitions in Fe/Cu(1 0 0)*, Surf. Sci. **480**, 163 (2001).

[9] H. Hibino, S. Wang, C. M. Orofeo, and H. Kageshima, *Growth and Low-Energy Electron Microscopy Characterizations of Graphene and Hexagonal Boron Nitride*, Prog. Cryst. Growth Ch. **62**, 155 (2016)

[10] H. W. Liu, H. T. Yuan, N. Fukui, L. Zhang, J. F. Jia, Y. Iwasa, M. W. Chen, T. Hashizume, T. Sakurai, and Q. K. Xue, *Growth of Topological Insulator* Bi_2Te_3 *Ultrathin Films on Si(111) Investigated by Low-Energy Electron Microscopy*, Cryst. Growth Des. **10**, 4491 (2010).

[11] A. Makoveev, P. Procházka, A. Shahsavar, L. Kormoš, T. Krajňák, V. Stará, and J. Čechal, *Kinetic Control of Self-Assembly Using a Low-Energy Electron Beam*, Appl. Surf. Sci. **600**, 154106 (2022).

[12] R. Zdyb, A. Locatelli, S. Heun, S. Cherifi, R. Belkhou, and E. Bauer, *Nanomagnetism Studies with Spin-Polarized Low-Energy Electron Microscopy and x-Ray Magnetic Circular Dichroism Photoemission Electron Microscopy*, Surf. Interface Anal. **37**, 239 (2005).

[13] T. Yasue, T. Koshikawa, and E. Bauer, *Low Energy Electron Microscopy/Diffraction Study on Growth of Ge on Si(113) Surface*, J. Vac. Sci. Technol. B **20**, 2496 (2002).

[14] A. Pavlovska, E. Bauer, and M. Giessen, *Low Energy Electron Microscopy Study of In on Si(111)*, J. Vac. Sci. Technol. B **20**, 2478 (2002).

[15] C. Klein, R. Ramchal, M. Farle, and A. K. Schmid, *Direct Imaging of Spin-Reorientation Transitions in Ultrathin Ni Films by Spin-Polarized Low-Energy Electron Microscopy*, Surf. Interface Anal. **38**, 1550 (2006).

[16] R. M. Tromp, J. B. Hannon, A. W. Ellis, W. Wan, A. Berghaus, and O. Schaff, *A New Aberration-Corrected, Energy-Filtered LEEM/PEEM Instrument. I. Principles and Design*, Ultramicroscopy **110**, 852 (2010).

[17] R. M. Tromp, J. B. Hannon, W. Wan, A. Berghaus, and O. Schaff, *A New Aberration-Corrected, Energy-Filtered LEEM/PEEM Instrument II. Operation and Results*, Ultramicroscopy **127**, 25 (2013).

[18] R. Wichtendahl et al., *SMART: An Aberration-Corrected XPEEM/LEEM with Energy Filter*, Surf. Rev. Lett. **5**, 1249 (1998).

[19] L. Yu et al., *Aberration Corrected Spin Polarized Low Energy Electron Microscope*, Ultramicroscopy **216**, 113017 (2020).

[20] M.S. Altman, H. Pinkvos, J. Hurst, H. Poppa, G. Marx, and E. Bauer, *Spin Polarized Low Energy Electron Microscopy of Surface Magnetic Structure*, Mater. Res. Soc. Symp. Proc. **232**, 125 (1991).

[21] D. Geelen, A. Thete, O. Schaff, A. Kaiser, S. J. van der Molen, and R. Tromp, *eV-TEM: Transmission Electron Microscopy in a Low Energy Cathode Lens Instrument*, Ultramicroscopy **159**, 482 (2015).

[22] R. M. Tromp, Y. Fujikawa, J. B. Hannon, A. W. Ellis, A. Berghaus, and O. Schaff, *A Simple Energy Filter for Low Energy Electron Microscopy/Photoelectron Emission Microscopy Instruments*, J. Phys.: Condens. Matter. **21**, 314007 (2009).

[23] Y. Fujikawa, T. Sakurai, and R. M. Tromp, *Micrometer-Scale Band Mapping of Single Silver Islands in Real and Reciprocal Space*, Phys. Rev. B **79**, 121401(R) (2009).

[24] Y. Fujikawa, T. Sakurai, and R. M. Tromp, *Surface Plasmon Microscopy Using an Energy-Filtered Low Energy Electron Microscope*, Phys. Rev. Lett. **100**, 126803 (2008).

[25] Lee H.Veneklasen, *Design of a Spectroscopic Low-Energy Electron Microscope*, Ultramicroscopy **36**, 76 (1991).

[26] J. Jobst, J. Kautz, D. Geelen, R. M. Tromp, and S. J. van der Molen, *Nanoscale Measurements of Unoccupied Band Dispersion in Few-Layer Graphene*, Nat. Commun. **6**, 8926 (2015).

[27] J. Jobst, A. J. H. van der Torren, E. E. Krasovskii, J. Balgley, C. R. Dean, R. M. Tromp, and S. J. van der Molen, *Quantifying Electronic Band Interactions in van der Waals Materials Using Angle-Resolved Reflected-Electron Spectroscopy*, Nat. Commun. **7**, 13621 (2016).

[28] J. Kautz, J. Jobst, C. Sorger, R. M. Tromp, H. B. Weber, and S. J. van der Molen, *Low-Energy Electron Potentiometry: Contactless Imaging of Charge Transport on the Nanoscale*, Sci. Rep. **5**, 13604 (2015).

[29] E. D. Tober, G. Witte, and H. Poppa, *Variable Temperature and Ex Situ Spin-Polarized Low-Energy Electron Microscope*, J. Vac. Sci. Technol. A **18**, 1845 (2000).

[30] L. Martín-García, A. Mascaraque, B. M. Pabón, R. Bliem, G. S. Parkinson, G. Chen, A. K. Schmid, and J. de la Figuera, *Spin Reorientation Transition of Magnetite (001)*, Phys. Rev. B **93**, 134419 (2016).

[31] J. E. Prieto, G. Chen, A. K. Schmid, and J. de la Figuera, *Magnetism of Epitaxial Tb Films on W(110) Studied by Spin-Polarized Low-Energy Electron Microscopy*, Phys. Rev. B **94**, 174445 (2016).

[32] L. Aballe, M. Foerster, E. Pellegrin, J. Nicolas, and S. Ferrer, *The ALBA Spectroscopic LEEM-PEEM Experimental Station: Layout and Performance*, J. Synchrotron Rad. **22**, 745 (2015).

[33] A. Doran, M. Church, T. Miller, G. Morrison, A. T. Young, and A. Scholl, *Cryogenic PEEM at the Advanced Light Source*, J. Electron. Spectrosc. **185**, 340 (2012).

[34] C. Tusche, A. Krasyuk, and J. Kirschner, *Spin Resolved Bandstructure Imaging with a High Resolution Momentum Microscope*, Ultramicroscopy **159**, 520 (2015).

[35] S. Babenkov et al., *High-Accuracy Bulk Electronic Bandmapping with Eliminated Diffraction Effects Using Hard X-Ray Photoelectron Momentum Microscopy*, Commun. Phys. **2**, 107 (2019).

[36] S. Y. Agustsson et al., *Temperature-Dependent Change of the Electronic Structure in the Kondo Lattice System* $YbRh_2Si_2$, J. Phys.: Condens. Matter. **33**, 205601 (2021).

[37] K. Medjanik et al., *Progress in HAXPES Performance Combining Full-Field k - Imaging with Time-of-Flight Recording*, J. Synchrotron. Rad. **26**, 1996 (2019).

[38] K. Medjanik et al., *Direct 3D Mapping of the Fermi Surface and Fermi Velocity*, Nat. Mater. **16**, 615 (2017).

[39] Q. Li et al., *Patterning-Induced Ferromagnetism of* Fe_3GeTe_2 *van der Waals Materials beyond Room Temperature*, Nano Lett. **18**, 5974 (2018).

[40] I. Valmianski, A. F. Rodríguez, J. Rodríguez-Álvarez, M. García Del Muro, C. Wolowiec, F. Kronast, J. G. Ramírez, I. K. Schuller, A. Labarta, and X. Batlle, *Driving Magnetic Domains at the Nanoscale by Interfacial Strain-Induced Proximity*, Nanoscale **13**, 4985 (2021).

[41] A. Palau et al., *Encoding Magnetic States in Monopole-Like Configurations Using Superconducting Dots*, Adv. Sci. **3**, 1600207 (2016).

[42] T. Shimojima et al., *Discovery of Mesoscopic Nematicity Wave in Iron-Based Superconductors*, Science **373**, 1122 (2021).

[43] R. Fujita, P. Bassirian, Z. Li, Y. Guo, M. A. Mawass, F. Kronast, G. van der Laan, and T. Hesjedal, *Layer-Dependent Magnetic Domains in Atomically Thin* Fe_5GeTe_2, ACS Nano **16**, 10545 (2022).

[44] S. M. Schramm, J. Kautz, A. Berghaus, O. Schaff, R. M. Tromp, and S. J. van der Molen, *Low-Energy Electron Microscopy and Spectroscopy with ESCHER: Status and Prospects*, IBM J. Res. & Dev. **55**, 1:1 (2011).

[45] S. Schramm, PhD Thesis (Leiden University): *Imaging with aberration-corrected low energy electron microscopy* (2013), ISBN: 978-90-8593-152-2. http://hdl.handle.net/1887/20843

[46] G. Binnig, H. Rohrer, C. Gerber, and E. Weibel, *7 × 7 Reconstruction on Si(111) Resolved in Real Space*, Phys. Rev. Lett. **50**, 120 (1983).

[47] F.-J. Meyer Zu Heringdorf, M. C. Reuter, and R. M. Tromp, *The Nucleation of Pentacene Thin Films*, Appl. Phys. A **78**, 787 (2004).

[48] A. Tebyani, F. B. Baalbergen, R. M. Tromp, and S. J. van der Molen, *Low-Energy Electron Irradiation Damage in Few-Monolayer Pentacene Films*, J. Phys. Chem. C **125**, 26150 (2021).

[49] B. E. Bammes, J. Jakana, M. F. Schmid, and W. Chiu, *Radiation Damage Effects at Four Specimen Temperatures from 4 to 100 K*, J. Struct. Biol. **169**, 331 (2010).

[50] K. Murata and M. Wolf, *Cryo-Electron Microscopy for Structural Analysis of Dynamic Biological Macromolecules*, BBA-Gen. Subjects **1862**, 324-334 (2018)

[51] J. R. Fryer, C. H. Mcconnell, F. Zemlin, and D. L. Dorset, *Effect of Temperature on Radiation Damage to Aromatic Organic Molecules*, Ultramicroscopy **40**, 163 (1992).

[52] L. A. Baker and J. L. Rubinstein, *Radiation Damage in Electron Cryomicroscopy*, in *Methods in Enzymology*, Jensen, G. J., Ed.; Academic Press (2010); Vol. 481, pp 371−388

[53] P. Feulner, T. Niedermayer, K. Eberle, R. Schneider, D. Menzel, A. Baumer, E. Schmich, A. Shaporenko, Y. Tai, and M. Zharnikov, *Strong Temperature Dependence of Irradiation Effects in Organic Layers*, Phys. Rev. Lett. **93**, 178302 (2004).

[54] R. V. Khatymov, R. F. Tuktarov, and M. V. Muftakhov, *Lifetime of Negative Molecular Ions of Tetracene and Pentacene with Respect to the Autodetachment of an Electron*, JETP Lett. **93**, 437 (2011).

[55] M. V. Muftakhov, R. V. Khatymov, and R. F. Tuktarov, *Decomposition of Aromatic Compounds Relevant to Organic Electronics under Exposure to Low-Energy Electrons*, Tech. Phys. **63**, 1854 (2018).

[56] R. Azria and G. J. Schulz, *Vibrational and Triplet Excitation by Electron Impact in Benzene*, J. Chem. Phys. **62**, 573 (1975).

[57] M. S. Deleuze, A. B. Trofimov, and L. S. Cederbaum, *Valence One-Electron and Shake-up Ionization Bands of Polycyclic Aromatic Hydrocarbons. I. Benzene, Naphthalene, Anthracene, Naphthacene, and Pentacene*, J. Chem. Phys. **115**, 5859 (2001).

[58] H. W. Jochims, H. Baumgärtel, and S. Leach, *Structure-Dependent Photostability of Polycyclic Aromatic Hydrocarbon Cations: Laboratory Studies and Astrophysical Implications*, ApJ **512**, 500 (1999).

[59] R. Boschi, E. Clart, and W. Schmidt, *Photoelectron Spectra of Polynuclear Aromatics. III. the Effect of Nonplanarity in Sterically Overcrowded Aromatic Hydrocarbons*, J. Chem. Phys. **60**, 4406 (1974).

[60] W. Schmidt, *Photoelectron Spectra of Polynuclear Aromatics. V. Correlations with Ultraviolet Absorption Spectra in the Catacondensed Series*, J. Chem. Phys. **66**, 828 (1977).

[61] R. Boschi, J. N. Murrell, and W. Schmidt, *Photoelectron Spectra of Polycyclic Aromatic Hydrocarbons*, Faraday Discuss. Chem. Soc. **54**, 116 (1972).

[62] J B Pendry, *The Application of Pseudopotentials to Low-Energy Electron Diffraction II: Calculation of the Reflected Intensities*, J. Phys. C: Solid State Phys. **2**, 2273 (1969).

[63] E. Bauer, *Surface Microscopy with Low Energy Electrons* (2014), Springer New York, ISBN: 978-1-4939-0934-6

[64] J. B. Pendry, *Theory of Photoemission*, Surf. Sci. **57**, 679 (1976).

[65] V. N. Strocov, E. E. Krasovskii, W. Schattke, N. Barrett, H. Berger, D. Schrupp, and R. Claessen, *Three-Dimensional Band Structure of Layered* $TiTe_2$*: Photoemission Final-State Effects*, Phys. Rev. B **74**, 195125 (2006).

[66] V. N. Strocov, H. I. Starnberg, and P. O. Nilsson, *Mapping the Excited-State Bands above the Vacuum Level with VLEED: Principles, Results for Cu, and the Connection to Photoemission*, J. Phys.: Condens. Matter **8**, 7539 (1996).

Summary

Molecular materials have been a subject of interest in both fundamental research as well as applications for decades, and have been studied as bulk crystals, (thin) films and as individual molecules. The differences in the physical, chemical and mechanical properties of molecular materials as well as the large variety of these properties among different categories of molecules, allow for tunability of material properties for a desired functionality or application. This dissertation explores pentacene crystals near the two-dimensional limit, i.e. in films of one to a few monolayers, a range of thickness less explored in the literature. Specifically, this dissertation focuses on real-time studies of such pentacene layers, starting with dynamics of layer growth, and including changes in the film's electronic and optical properties as a result of varying thickness or external stimuli. Pentacene was chosen as a representative of small polycyclic aromatic molecules.

For this purpose, an experimental technique called Low Energy Electron Microscopy (LEEM) is employed, since it satisfies several important criteria. LEEM probes at most the top few nanometers of the sample, and hence it is suitable for studying ultrathin films. Furthermore, it allows for real-time imaging and spectroscopy, provides high spatial and spectroscopic/energy resolution, and the range of electron energies is relevant for studying both electronic properties as well as chemical processes. Chapter 2 of this dissertation describes the LEEM instrument and the various measurement techniques it provides.

In the growth of molecular layers, the substrate has significant influence on the crystal structure as well as various properties of the adlayer. In chapter 3, we study the growth of crystalline pentacene layers on hexagonal boron-nitride (hBN) and graphite flakes, two members of an emerging class of substrates, i.e. van der Waals materials. These two substrates have nearly identical atomic surface lattices that closely match the aromatic ring structure of pentacene, yet graphite is a conductor while hBN is an insulator. We observe that on both substrates, pentacene first forms a flat-lying wetting layer due to a templating effect by the substrates. Next, however, pentacene grows in a standing-up thin film phase on hBN, but forms tilted recumbent (i.e. pentacene molecules lying down) crystalline domains on graphite. We ascribe this to the differences in the electronic properties of the substrates, which result in a stronger electronic interaction between pentacene and graphite, compared to hBN. This chapter highlights the multi-faceted way in which substrate properties, such as surface lattice, electronic properties, as well as cleanliness, affect the growth of the molecular adlayer.

In chapter 4, we study chemical changes in molecules as a result of interaction with low energy electrons. This topic is of immense importance in various applications, such as electron-beam lithography, or for reduction of damage to organic or biological matter as a result of exposure to ionizing radiation. Here, we study the cross-section for damage to crystalline pentacene layers as a result of exposure to an electron beam with tuneable energies between 0 eV and 40 eV. We investigate the damage primarily by means of changes in the diffraction pattern of the pentacene layers, as well as changes in their electronic band structure. We conclude that different mechanisms describe electron interaction and damage at different electron energies. Namely, at energies of only a few eV, (dissociative) electron attachment is the key mechanism, while at higher energies, impact ionization dominates. We observe that beam damage decreases as the energy of the incident electrons is reduced. The reduction in damage cross-section is particularly rapid below 10 eV, such that near 0 eV, beam damage is virtually nil. This is in contrast to lithography resists such as PMMA or tin-oxo cages, which in similar experiments show beam damage upon interaction with incident electrons of all energies down to 0 eV. This difference can be of relevance for lithography. Specifically, it implies that the use of aromatic materials as e-beam resists could reduce the effects of secondary electrons in resist exposure, given that these electrons usually have energies of only a few eV.

In chapter 5, we study the influence of unoccupied electronic states above the vacuum level on the emission of photo-electrons and secondary electrons, using thin crystalline pentacene films as a model system. These states are known to play an important role as intermediate states from which an electron is emitted to the vacuum, yet, they are often overlooked or not independently investigated, mostly due to the lack of proper spectroscopic techniques. Monitoring the growth of pentacene layers on a silicon substrate using UV photons, we observe a decrease in photoemission intensity from the pentacene film with the growth of each additional layer. Given an absence of increase in the ionization energy for thicker films, or change in the crystal structure of the layers, the reduction in intensity is explained by suppression of the photoemission process. The suppression can be directly connected to a reduction in the density of available intermediate states in thicker films. Since electrons first need to transition into these intermediate electronic states above the vacuum level before leaving the material, a reduction in the availability of these states directly results in lower photoemission intensity. The density of unoccupied electronic states above the vacuum level can be directly measured in LEEM via electron reflectivity spectra, in which lower density of electronic states at any given electron energy results in higher electron reflectivity. Furthermore, we demonstrate the influence of the unoccupied electronic states on the emission of secondary electrons. Using electron beam irradiation, we cause controlled changes in the structure of the pentacene films, which result in concomitant changes in their unoccupied electronic density of states, observable in LEEM electron reflectivity spectra. Electron energy spectra measurements reveal that these changes directly affect the energy distribution of secondary electrons. The observations in pentacene films regarding the role of unoccupied electronic states in electron emission processes can be generalized to all materials, and highlight the importance of knowledge of these states for correct interpretation of electron emission experiments. In chapter 6, we further explore the unoccupied electronic states of crystalline pentacene layers above the vacuum level. In particular, we obtain LEEM electron reflectivity spectra not only as a function of energy, but in addition, also as a function of in-plane momenta. These measurements provide a fuller picture of the unoccupied density of states, and are relevant for the discussion above, regarding emission of electrons that are ejected at an angle with respect to the surface normal.

Finally, we describe the design of a cryogenic sample chamber for LEEM in chapter 7. The design is based on the IBM/SPECS aberration-corrected LEEM instrument, with modifications that include mechanisms for cooling the sample and its surroundings, and minimization of the various sources of heat load. Using both a liquid nitrogen dewar connected to the sample stage and the superconducting objective lens, as well as a liquid helium flow cryostat cooling the sample and its vicinity, controllable sample temperatures down to 15K have been achieved. We also present the first scientific measurements obtained from a pentacene film at various temperatures between 300K and 52K. These measurements show a reduction in electron beam irradiation damage cross-section at lower temperatures, as well as changes in LEEM electron reflectivity spectra upon cooling the sample. The cryogenic chamber enables novel LEEM experiments addressing questions in surface science and condensed matter physics.

Samenvatting

Moleculaire materialen staan al tientallen jaren in de belangstelling, zowel in het kader van fundamenteel onderzoek als voor toepassingen. Ze worden bestudeerd in verschillende vormen, zoals bulkkristallen, (dunne) films en ook als individuele moleculen. De verschillen in de fysische, chemische en mechanische eigenschappen van moleculaire materialen en de grote verscheidenheid in eigenschappen van verschillende categorieën moleculen, maken het mogelijk om materiaaleigenschappen af te stemmen op een gewenste functionaliteit of toepassing. Dit proefschrift onderzoekt pentaceenkristallen nabij de tweedimensionale grens, d.w.z. in films van één tot enkele monolagen, een diktebereik dat relatief weinig onderzocht is in de literatuur. Specifiek richt dit proefschrift zich op tijdsafhankelijke studies van zulke pentaceenlagen, te beginnen met de dynamiek van laaggroei, met inbegrip van veranderingen in de elektronische en optische eigenschappen van de film als gevolg van variërende dikte of externe stimuli. Pentaceen is gekozen als representatieve vertegenwoordiger van de belangrijke groep van kleine polycyclische aromatische moleculen.

Voor mijn werk heb ik een experimentele techniek genaamd Lage Energie Elektronen Microscopie (LEEM) gebruikt, omdat deze aan een aantal belangrijke criteria voldoet. LEEM tast hooguit de bovenste paar nanometer van het sample af en is daarom geschikt voor het bestuderen van ultradunne films. Bovendien maakt het live beeldvorming en spectroscopie mogelijk, biedt het een hoge ruimtelijke en energetische resolutie, en is het bereik van elektronenenergieën relevant voor het bestuderen van zowel elektronische eigenschappen als chemische processen. Hoofdstuk 2 van dit proefschrift beschrijft ons LEEM instrument, genaamd 'ESCHER', en de verschillende meettechnieken die het biedt.

Bij de groei van moleculaire lagen heeft het substraat een significante invloed op de kristalstructuur en verschillende eigenschappen van de groeiende laag. In hoofdstuk 3 bestuderen we de groei van kristallijne pentaceenlagen op hexagonaal boronitride (hBN) en grafietvlokken, twee leden van een opkomende klasse van substraten, de zogenaamde 'van der Waals materialen'. Deze twee substraten hebben bijna identieke atomaire roosters die nauw overeenkomen met de aromatische ringstructuur van pentaceen. Grafiet is een geleider, terwijl hBN een isolator is. We zien dat op beide substraten het pentaceen eerst een platliggende bevochtigingslaag vormt als gevolg van een aanpassing aan de substraatstructuur. Vervolgens groeit pentaceen echter verschillend verder: in een (op)staande dunne-filmfase op hBN, maar als gekantelde, liggende kristallijne domeinen op grafiet. We schrijven dit toe aan de verschillen in de elektronische eigenschappen van de substraten, die resulteren in een sterkere elektronische interactie tussen pentaceen en grafiet, vergeleken met hBN. Dit hoofdstuk belicht daarmee de veelzijdige manier waarop substraateigenschappen, zoals oppervlakterooster, elektronische eigenschappen en zuiverheid, de groei van de moleculaire laag beïnvloeden.

In hoofdstuk 4 bestuderen we chemische veranderingen in moleculen als gevolg van interactie met lage energie elektronen. Dit onderwerp is van groot belang voor verschillende toepassingen, zoals elektronenbundellithografie, of voor het (leren) beperken van schade aan organische of biologische materie bij blootstelling aan ioniserende straling. In het bijzonder bestuderen we schade aan kristallijne pentaceenlagen als gevolg van blootstelling aan een elektronenbundel met instelbare energieën tussen 0 eV en 40 eV. We onderzoeken de schade voornamelijk door veranderingen in het diffractiepatroon van de pentaceenlagen te volgen, en ook door veranderingen in hun elektronische bandstructuur te meten. We concluderen dat elektroneninteractie en schade bij verschillende elektronenenergieën door verschillende mechanismen wordt beschreven. Bij energieën van slechts enkele eV (elektronvolts) is (dissociatieve) elektronaanhechting het belangrijkste mechanisme, terwijl bij hogere energieën impact-ionisatie domineert. We zien dat bundelschade afneemt naarmate de energie van de invallende elektronen wordt verlaagd. De vermindering van de schade-dwarsdoorsnede gaat vooral snel onder 10 eV, zodat in de buurt van 0 eV de stralingsschade aan de laag vrijwel nihil is. Dit is in tegenstelling tot lithografische resists zoals PMMA of tin-oxo cages, die in vergelijkbare experimenten bundelschade vertonen bij interactie met invallende elektronen van alle energieën, dus ook rond 0 eV. Dit verschil kan van groot belang zijn voor lithografie. Specifiek impliceert het dat het gebruik van aromatische materialen als resists de (ongewenste) schade-effecten van secundaire elektronen kan verminderen, aangezien juist zulke elektronen gewoonlijk energieën van slechts enkele eV hebben.

In hoofdstuk 5 bestuderen we de invloed van onbezette elektronische toestanden boven het vacuümniveau op de emissie van foto-elektronen en secundaire elektronen. Opnieuw kiezen we voor dunne, kristallijne pentaceenlagen als modelsysteem. Het is bekend dat onbezette elektron-toestanden een belangrijke rol spelen als ‘tussenliggende’ niveaus (boven het vacuümniveau) van waaruit een elektron naar het vacuüm wordt uitgestoten, bijvoorbeeld na excitatie door een lichtdeeltje (het foto-elektrisch effect). Toch worden ze bijna altijd over het hoofd gezien in de analyse, met name door een gebrek aan de juiste spectroscopische technieken. In ons experiment bekijken we hoe de fotoemissie-intensiteit van de pentaceenfilm verandert met de groei van elke extra moleculaire laag. Daarvoor belichten we de lagen met ultraviolet (UV) licht. Interessant genoeg vinden we een afname van de foto-elektron emissie voor dikkere lagen. Aangezien de ionisatie-energie niet toeneemt voor dikkere lagen en ook de kristalstructuur niet verandert, verklaren we deze afname door een verandering binnen het twee-staps foto-emissieproces zelf. Preciezer gezegd: we zien een verband tussen de onderdrukking van foto-emissie en een vermindering van de dichtheid van beschikbare tussentoestanden in dikkere films. Aangezien foto-elektronen eerst moeten overgaan naar een tussenliggende toestand, voordat ze het materiaal verlaten, leidt een vermindering van de beschikbaarheid van deze toestanden direct tot een lagere fotoemissie-intensiteit/intensiteit van de foto-emissie. Belangrijk hierbij is dat de dichtheid van deze onbezette elektronische toestanden boven het vacuümniveau direct kan worden gemeten in LEEM via elektronenreflectiespectra. Hierbij geldt dat een lagere dichtheid van elektronische toestanden bij een gegeven elektronenenergie resulteert in een hogere elektronenreflectiviteit. Verder tonen we de invloed van de onbezette elektronische toestanden op de emissie van secundaire elektronen. Door pentaceen-lagen te bestralen met de elektronenbundel bij hogere energie veroorzaken we gecontroleerde veranderingen in de structuur van de pentaceenfilms, die resulteren in gelijktijdige veranderingen in hun onbezette elektronische toestandsdichtheid. Dit laatste is vervolgens waarneembaar in LEEM elektronenreflectiviteitsspectra bij lagere energieën. Metingen van elektronenenergiespectra laten zien dat deze veranderingen rechtstreeks van invloed zijn op de energieverdeling van secundaire elektronen. De waarnemingen in pentaceenfilms met betrekking tot de rol van onbezette elektronische toestanden in elektronen-emissieprocessen kunnen worden gegeneraliseerd naar alle materialen. Dit benadrukt het belang van kennis van deze toestanden voor een juiste interpretatie van elektronenemissie-experimenten.

In hoofdstuk 6 onderzoeken we de onbezette elektronische toestanden van kristallijne pentaceenlagen boven het vacuümniveau in meer detail. In het bijzonder verkrijgen we LEEM elektronenreflectiviteitsspectra niet alleen als functie van energie, maar ook als functie van de elektron-impuls in het vlak van de laag (dwz – hoek van inval). Deze metingen geven een vollediger beeld van de onbezette toestandsdichtheid en zijn relevant voor de bovenstaande discussie, met betrekking tot de emissie van elektronen die het materiaal onder een hoek verlaten.

Ten slotte beschrijven we het ontwerp van een cryogene samplekamer voor LEEM, in hoofdstuk 7. Het ontwerp is gebaseerd op het IBM/SPECS aberratie-gecorrigeerde LEEM instrument, met aanpassingen die het koelen van het sample en zijn omgeving mogelijk maken, zoals in eerste instantie beschreven door Dr. Sebastian Schramm. Hierbij wordt de warmtebelasting door verschillende bronnen geminimaliseerd. We maken gebruik van twee koelmethodes. Ten eerste hebben we een Dewar vat met vloeibare stikstof verbonden met de samplehouder en de supergeleidende objectief-lens. Ten tweede gebruiken we een vloeibaar-helium flow-cryostaat die het sample en zijn omgeving nog verder afkoelt. Op deze manier hebben we regelbare sample-temperaturen tot 15 K bereikt. We presenteren vervolgens de eerste LEEM-metingen aan een pentaceenfilm bij lage temperaturen tussen 300K en 52K. Deze metingen laten een vermindering zien van schade door elektronenstraling bij lagere temperaturen, evenals veranderingen in de LEEM elektronenreflectiespectra bij het koelen van het sample. De cryogene kamer maakt nieuwe LEEM-experimenten mogelijk voor vragen op het gebied van oppervlaktefysica en fysica van gecondenseerde materie bij lage temperaturen.

Curriculum Vitae

Arash Tebyani

I was born in September 1990 in Tehran, Iran. I obtained my bachelor’s degree in “Electrical Engineering – Electronics” at Amirkabir University of Technology in Tehran. Afterwards, I continued my studies in the “Nanoscience” master’s program of the Zernike Institute for Advanced Materials at University of Groningen. I carried out my research project in the “Nanostructures of Functional Oxides” group under the supervision of Prof. Beatriz Noheda, studying the deposition of ferroelectric thin films, with the goal of investigating the effects of growth parameters and post-deposition treatments on the domain structure and the properties of the films. In June 2018, I joined the group of Prof. Sense Jan van der Molen at Leiden University for my PhD. I studied the growth and electronic properties of few-monolayer molecular films primarily using the technique “Low Energy Electron Microscopy”. In October 2022, I joined the group of Prof. Michel Orrit at Leiden University to study the fluorescence of individual molecules adsorbed on surfaces at cryogenic temperatures.

List of Publications

1. **A. Tebyani**, R.M. Tromp, S.J. van der Molen, *"Critical Role of Electronic States above the Vacuum Level in Photo-Electron and Secondary-Electron Emission in Few-Monolayer Pentacene Films"*, Phys. Rev. B 108, 045425 (2023)

2. **A. Tebyani**, S. Schramm, M. Hesselberth, D. Boltje, J. Jobst, R.M. Tromp, S.J. van der Molen, *"Low Energy Electron Microscopy at Cryogenic Temperatures"*, Ultramicroscopy 253, 113815 (2023)

3. **A. Tebyani**, F.B. Baalbergen, R.M. Tromp, S.J. van der Molen *"Low-Energy Electron Irradiation Damage in Few-Monolayer Pentacene Films"*, J. Phys. Chem. C 125, 26150 (2021)

4. **A. Tebyani**, R.M. Tromp, S.J. van der Molen, *"Comparison of Pentacene Layer Growth on Graphite and hBN Flakes"*, Submitted for Publication

5. R. Smit, **A. Tebyani**, J. Hameury, S.J. van der Molen, M. Orrit, *"Sharp zero-phonon lines of single organic molecules on a hexagonal boron-nitride surface"*, Nat. Commun. 14, 7960 (2023)

Acknowledgments

The work presented in this dissertation would not have been possible without the generous support and contributions of many others in the institute. Here, I would like to take the opportunity to express my gratitude.

First, I would like to thank my supervisor, Prof. Sense Jan van der Molen, for offering me this position and welcoming me in the group. You were always available for discussions, knowledgeable and showed great interest in my work. In addition, I'm grateful for the freedom and flexibility you offered me regarding managing the project, and being open to new experiment ideas. I'm thankful for your guidance and support throughout the project.

Next, I want to thank Prof. Ruud Tromp. Our regular discussions about the experiments, and your immense knowledge about LEEM were invaluable in understanding the results and planning the experiments.

I would also like to thank my second promotor, Prof. Michel Orrit. Although we didn't eventually carry out the combined LEEM-fluorescence charge transport experiments that were initially planned, I enjoyed our discussions during my PhD, one of which resulted in the project on terrylene/hBN fluorescence. I would also like to thank you for offering me a position to work on that project after my PhD.

Next, I want to thank Marcel Hesselberth. I'm grateful for your technical support and help in setting up new experiments with LEEM. I especially enjoyed working together in the final stages of the development and the first measurements in the cryogenic chamber. I'm also thankful to Ruud van Egmond for technical support regarding LEEM hardware parts. I thank Federica Galli for her support regarding AFM measurements, Douwe Scholma for his technical support with cleanroom and annealing setups, Peter van Veldhuizen and Raymond Koehler from the electronics department, Martijn Witlox from the fine mechanical department, and Wilfred van der Geest from the cryogenics department. I'm also grateful for the administrative support from Ellie van Rijsewijk, Michelle Wijfje, Marije Boonstra and Henriette van Leeuwen.

I thank Dr. Johannes Jobst for supervision of the initial part of the project, and help regarding measuring with LEEM as well as the first pentacene experiments. I'm also grateful to my PhD colleagues for their help regarding scientific experiments, as well as general discussions and enjoyable company throughout the years, in particular, I would like to thank Peter Neu, Norman Blümel, Jedrzej Tepper, Guido Stam, Amin Moradi, Junxiang Yao, and Robert Smit. I wish you success in your research.

During my PhD, I had the pleasure to work closely with several students as their supervisor. Emile Ankoné, the results of your work on the electron gun emission project, specifically the implementation of imaging with reduced beam currents, proved very useful during many of my later experiments. Erik Baalbergen, your work on the analysis of electron beam irradiation damage in pentacene films was very fruitful. I'm glad we published that work together. Auke Vlasblom, I'm glad you decided to come to Leiden from Utrecht for your research project to work on charge transport through pentacene layers. In the end, we successfully performed potentiometry measurements, although not on hBN substrates. We also observed some unexpected field-effect phenomena. Tomas Osterholt, we worked further on pentacene transport measurements, and solved some of the remaining obstacles, although the pentacene growth still remained challenging. I was impressed by the quality of your work in parallel on the theory and simulation of mapping potential drop during charge transport. Leander Kalff, we performed experiments on electron transmission through pentacene layers together with Peter. You prepared several high-quality samples, and the results of your analysis on the mean free path through the layers were insightful. I wish you all success in your PhDs and future careers.

I also want to thank Prof. Björn Baumeier and Ruben Gerritsen at Eindhoven University of Technology. I enjoyed our collaboration on the electronic band structure of pentacene layers, and appreciate your efforts in calculating the band structure with different methods.

Finally, I would like to thank my family. I'm immensely grateful for all your support and encouragement throughout my education.